Platinum nanoparticle-polyoxometalate based bimetallic catalyst for proton exchange membrane fuel cell and bipolar electrodeposition based combinatorial material library applied in sensors and energy systems

by

Rajakumari Ramaswamy

A dissertation submitted to the Graduate Faculty of
Auburn University
in partial fulfillment of the
requirements for the Degree of
Doctor of Philosophy

Auburn, Alabama
May 6, 2012

Keywords: Pt-based bimetallic catalysts, Fuel cells, Combinatorial strategies, Bipolar technology.

Approved by

Curtis Shannon, Chair, Professor of Chemistry and Biochemistry
Jeffrey Fergus, Professor of Materials Research and Education Center
Wei Zhan, Assistant Professor of Chemistry and Biochemistry
Christopher Easley, Assistant Professor of Chemistry and Biochemistry

Abstract

The first part of chapter 1 summarizes the reports on the improved oxygen reduction reaction (ORR) kinetics on Pt-bimetallic catalysts used in proton exchange membrane fuel cell (PEMFC). An account on the significance of polyoxometalate (POM), an inorganic ligand system to stabilize the base metal component of a multimetallic ORR catalyst, is given in addressing the issue associated with the instability of bimetallic Pt alloy surface under PEMFC cathode operating condition.

The second part of chapter 1 deals with the significance of combinatorial material library and various methods including bipolar electrochemistry to synthesize the material library.

Chapter 2 deals with a bimetallic ORR catalyst system composed of Pt nanoparticle (PtNP) and Co-substituted Dawson type polyoxometalate (Co-POM). The fabricated electrocatalysts films (POM-stabilized PtNP, cysteamine- or poly (diallyl dimethyl ammonium chloride) (PDDA)-stabilized PtNP/POM layer-by-layer (LBL) assembly) were characterized by transmission electron microscopy (TEM), scanning electron microscopy (SEM) and energy dispersive X-ray spectroscopy (EDX). The ORR kinetics of the electrocatalysts were studied using the rotating disc electrode (RDE) experiment. We confirmed our hypothesis that Co center in Co-POM helps promote O=O bond splitting and transfer the split O atom to the PtNP surface from the ORR kinetics using the PDDA-stabilized PtNP/POM LBL assembly.

In chapter 3, we report the synthesis of Ag-Au alloy gradients on stainless steel substrates using bipolar electrodeposition (BP-ED). The alloy gradient was characterized using SEM/EDX. Confocal Raman microscopy was employed to determine the optimum alloy composition of 70 atomic% Ag/30 atomic% Au that resulted in the maximum surface enhanced Raman scattering (SERS) intensity and the optimum composition is explained on the basis of composition-dependent changes in the local surface plasmon resonance (LSPR) of the electrodeposited Ag-Au alloy.

Chapter 4 deals with the Pd-Au alloy gradient generated by bipolar electrodeposition on a gold bipolar electrode, its characterization using SEM/EDX and its screening for the electrocatalytic activity towards formate oxidation using Raman spectroelectrochemistry. The optimum composition, 70 atomic% Pd/ 30 atomic% Au, is explained based on the band theory model applied to alloys between metals from group VIII and IB.

Chapter 5 summarizes my research work and provides the directions for future studies.

Acknowledgements

I owe my deepest gratitude to my supervisor, Dr. Curtis Shannon for his invaluable guidance, constant support and assistance at all levels. I would also like to express my sincere gratitude to my supervisory committee members, Dr. Jeffrey Fergus, Dr. Wei Zhan and Dr. Christopher Easley for the very useful and important suggestions that made my research successful. I also wish to thank Dr. Minseo Park for serving as the outside reader for my dissertation.

I would like to convey my thanks to Dr. Micheal Miller for assisting me in acquiring the transmission electron micrographs, Dr. Blumenthal for his efforts in collecting the X-ray diffractograms. My special thanks to Mr. Matthew Montgomery for his great efforts to make the custom-designed spectroelectrochemical cell. I would also like to thank the chemistry department staff for their support and assistance during the course of my Ph.D. studies.

My Special thanks to all my graduate friends, especially my research group members, Dr. Anand Sankarraj, Dr. Tsunghsueh Wu, Dr. Junxua Xin, Dr. Hongxia Zhang, Dr. Chaokang Gu, Dr. Sridevi Ramakrishnan, Mrs. Weiping Li, Mrs. Sanghapi Ndzesse Sanghapi, Mrs. Tanyu Wang and Ms. Yajiao Yu for their assistance in all phases.

I am indebted to my parents and friends for their moral support and encouragement throughout my studies.

Table of Contents

List of Tables

List of Schemes

List of Figures

Chapter 1

INTRODUCTION

1.1 The Motivation for my research work:

"The true purpose of education is to train the mind to think."

This statement was made by Albert Einstein to explain the necessity of a college education. Education achieves its full meaning when students pursue research oriented education in which they are trained to apply fundamental scientific facts through experimentation. A student can gain clear vision of how scientific discoveries and inventions transition from research to implementation including the need for the invention of new materials and methods to achieve implementation. In particular, electroanalytical chemistry, as an interdisciplinary field, provides an in depth base for the synergy between fundamental research and technological development which both enhance the global economy and improve human welfare. My research work addresses important social needs such as sensors applied in clinical diagnosis, environmental science, and energy systems.

My first project was directed towards the development of an electrocatalyst for proton exchange membrane fuel cell (PEMFC) application. My second project involved the fabrication of a continuous material library which was then screened to choose the best performing material candidate to be applied in sensors as surface enhanced Raman spectroscopy (SERS) substrate and in fuel cells as anode catalyst.

1.2 Development of oxygen reduction reaction (ORR) electrocatalyst- platinum nanoparticle-polyoxometalate nanocomposite for proton exchange membrane fuel cell (PEMFC) application:

1.2.1 Strategies focused on the development of PEMFC technology:

Global industrial and technological advancements have created unprecedented world energy demands. Transportation is one sector that demands a great amount of energy and currently relies on fossil fuels burnt in internal combustion engines whose energy conversion efficiency is just 20%. Fuel cells can convert energy efficiently at about 64%. PEMFCs operating at low temperatures will be suitable for running vehicles. PEMFCs require the use of the precious metal Pt, which is considered to be good for catalyzing reactions at the anode and cathode. PEMFCs, however, show significant activation loss at higher current densities because of the sluggish kinetics of ORR at the Pt cathode.[1] This leads to the need for high loading of Pt which, due to its high cost, makes the commercialization of PEMFCs difficult.[1] Since the late 1990s, the continuous effort to reduce the cost of PEMFCs has resulted in significant reduction in Pt loading in membrane/electrode assembly (MEA).[1] The current MEA loading is ~ 0.6-0.8 mg_{Pt}/cm^2_{MEA} and the power density has increased to 0.7 W/cm^2_{MEA} at cell voltages as high as 0.68 V (i.e. at 58% energy conversion efficiency based on the thermodynamic H_2/air potential at 80°C and near-ambient pressure).[1] The corresponding Pt-specific power density is 0.85 – 1.1 g_{Pt}/kW which results in a requirement of 72-94 g of Pt for a ~ 85 kW fuel cell stack in a 75 kW_{net} automotive fuel cell system.[1]

For large-scale automotive applications the above amount of Pt has to be reduced five times, both due to the high cost of Pt and to Pt supply limitations.[1] Here the target is

to reduce the Pt-specific power density to <0.2 g_{Pt}/kW at cell voltages of ≥0.65V.[1] In other words, the current loading of 0.8 mg_{Pt}/cm^2 (0.4 mg_{Pt}/cm^2 on the cathode side and 0.4 mg_{Pt}/cm^2 on the anode side) has to be reduced to ca. 0.15 mg_{Pt}/cm^2.[1] Reducing the loading of the Pt catalyst at the anode from 0.4 to 0.05 mg_{Pt}/cm^2 was made possible with the kinetically favored hydrogen oxidation reaction at the anode.[1] But reducing the Pt loading at the cathode becomes challenging, since the oxygen reduction reaction (ORR), is kinetically hindered at the Pt cathode.[1] At this point, the goal is to reduce the cathode loading from 0.4 mg_{Pt}/cm^2 to 0.1 mg_{Pt}/cm^2 without affecting cell performance.[1] This can be achieved by studying the factors that affect cell performance. Fig. 1.1 shofws the factors affecting the cell performance of a PEMFC.[1] They are (i) ORR overpotential, η_{ORR}, at the cathode; (ii) Voltage drop due to Ohmic resistance of the cell components, ΔE_{Ohmic}; and (iii) mass-transport-induced voltage losses, η_{tx}, at high current densities. Better MEA design, which can maximize the Pt utilization,[1] can significantly reduce η_{tx} . ORR overpotential, η_{ORR}, can be reduced by implementing a highly active catalyst material such as a Pt alloy, which has been shown to have 2-3 times higher ORR kinetic current than the pure Pt.[1]

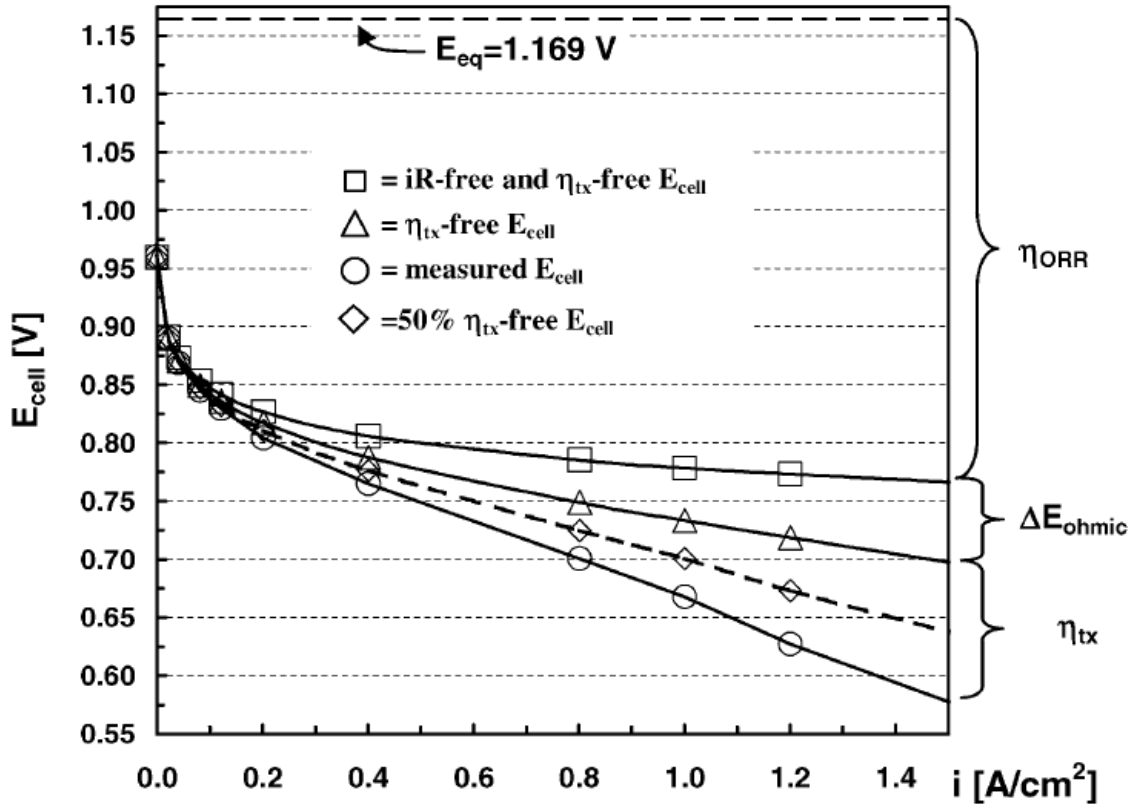

Fig.1.1 PEMFC polarization curve showing the various factors affecting the cell performance.

(Reprinted from Ref. 1 with permission from Elsevier)

1.2.2 Pt-alloy catalysts for PEMFC cathodes:

Implementation of Pt alloy catalyst with PEMFCs has been hindered due to technical issues associated with the leaching of base metal from the Pt-base metal alloy and its blocking in the proton conduction sites in the Nafion membrane, as well as in the ionomer in the catalyst layer leading to high ohmic resistance inside the cell, affecting cell performance.[1] The main criteria that need to be considered in developing a fuel cell catalyst for automotive application has to be cost effectiveness as well as high stability (over ~ 5000 h or more for automotive application with low degradation rates of a few

μV/h).[1] To meet these criteria, the development of a highly active, well dispersed, and corrosion resistant Pt-bimetallic catalyst is necessary.

Several fundamental studies are probing the relation between ORR performance and the structural-electronic properties of the bimetallic Pt alloys with respect to the significance of these properties in catalyzing a redox reaction. In the 1950s and 1960s, Bockris and co-workers did significant research to illustrate the influence of electronic and geometric factors in the electrocatalysis of hydrogen, oxygen, and organic electrode reactions.[2] These reactions can be catalysed quickly using a catalyst whose electronic and geometric properties are tuned by alloying a metal with another metal.

In 1970, Appleby showed a volcano or inverted parabolic type relationship between the ORR current density at 800 mV vs RHE in 85% orthophosphoric acid and the heat of adsorption of the oxygenated reaction intermediate on using Pt group metals and Pt -Ru alloy.[3] The Volcano plot indicates that the binding strength of the oxygenated species on the catalyst surface has to be optimum in order to achieve the maximum ORR performance as shown in Fig. 1.2.

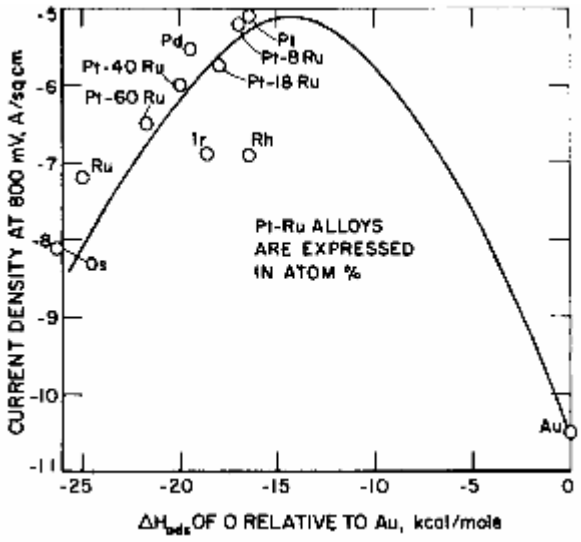

Fig. 1.2 ORR current density at 800 mV in 85% orthophosphoric acid shown against calculated M-O adsorbate bond strength (relative to gold).

(Reprinted from Ref. 3 with permission from Taylor & Francis)

More recently, Jalan et al. pointed out that it is not appropriate to correlate the ORR performance with the ΔH_{ad} for the adsorption of oxygenated species on the catalyst surface due to the possible compensation effect of ΔS_{ad} on ΔH_{ad} in relating ΔH_{ad} to ΔG_{ad}.[4]

Jalan, et al. therefore further investigated the improved ORR performance.[4] Since the percent d-band character (used by Appleby to calculate the relative heat of adsorption of oxygenated species) is a function of the single bond radius of the metal (a geometric factor) according to Pauling's relationship, these authors stated that it was unclear that the electrocatalytic activity is directly influenced by the Pt, Pt alloy interatomic distance, or any other parameter dependent on the interatomic distance. These authors made a correlation between the specific activity of the Pt bimetallic alloys for the ORR in phosphoric acid and the nearest neighbor distance of the Pt alloys calculated from the X-ray diffraction (XRD). The specific activity of the Pt alloys increased linearly with

decreasing nearest neighbor distance relative to Pt with Pt-Cr showing the maximum ORR performance as shown in Fig. 1.3. These authors expect a volcano behavior if more other alloys such as Pt-Co, Pt-Ni based on their lattice parameter are covered. On observing the improved ORR performance on the Pt alloys, the researchers used these alloys as a cathode catalyst in phosphoric acid fuel cell (PAFC).

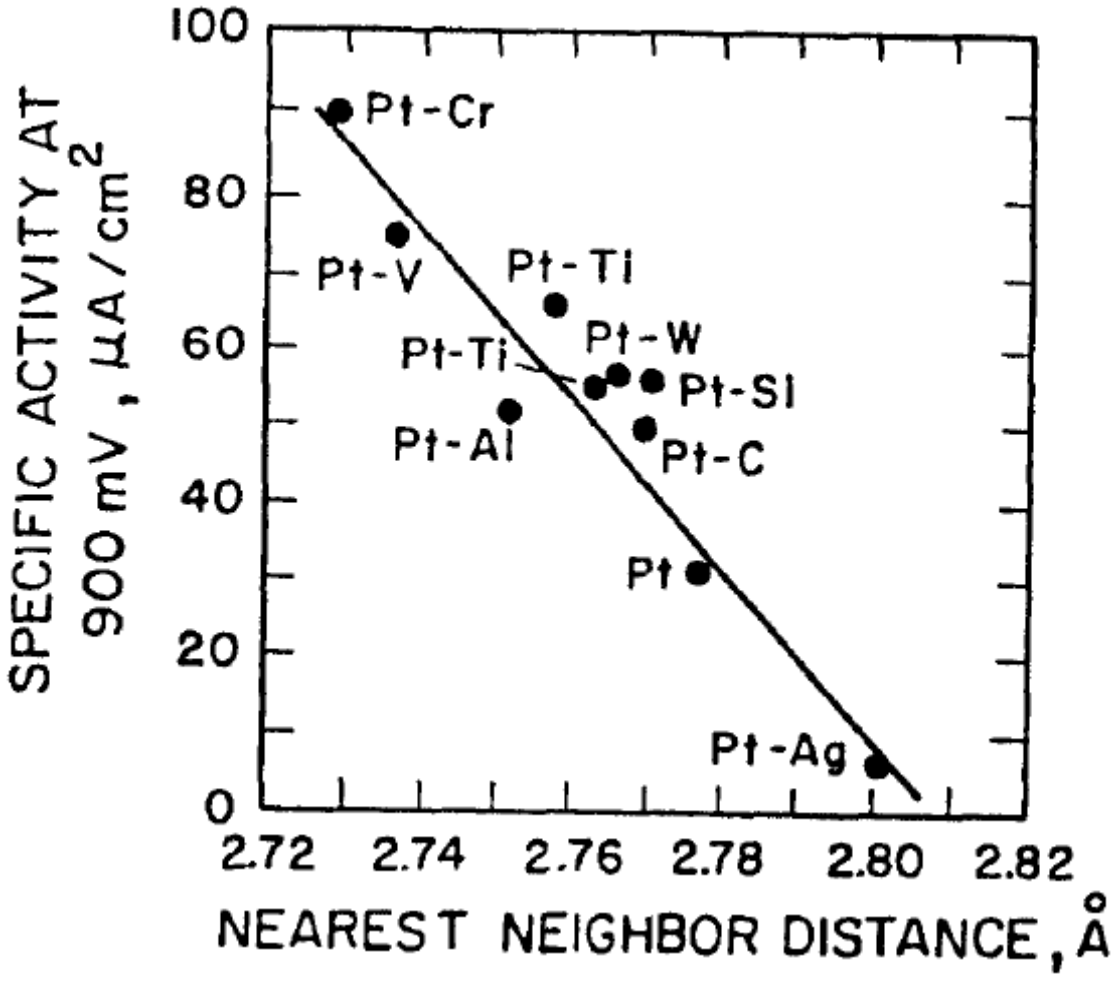

Fig. 1.3 Specific activity for oxygen reduction vs. electrocatalyst nearest-neighbor distance.

(Reprinted from Ref. 4 with permission from the Electrochemical Society)

The successful implementation of Pt alloys in PAFC became the driving force for the application of Pt alloys in PEMFC.

Mukergee, et al. have investigated the ORR catalytic effect of five Pt-based binary alloys supported on carbon with a high surface area (PtCr/C, PtMn/C, PtFe/C, PtCo/C and PtNi/C) in a proton exchange membrane fuel cell.[5] To probe the electronic and the structural effects of Pt-alloys on ORR, *in situ* X-ray absorption spectroscopy (XAS) experiments and X-ray diffraction (XRD) were carried out in addition to the electrochemical experiments. The order of catalytic activity in terms of cell performance is PtCr/C > PtFe/C > PtMn/C PtCo/C > PtNi/C > Pt/C. Correlation of the cathode performance (log i_{900mV}, mA/cm^2) with the d-orbital vacancy per atom and Pt-Pt interatomic distance of the five Pt-alloys studied here resulted in a volcano type curve with Pt-Cr showing the maximum activity as shown in Fig. 1.4. This correlation proves the interplay of electronic and structural effects on the catalytic activity of the Pt and Pt alloy/C. Here the optimum electronic and structural properties help to minimize the adsorption of OH on the electrode surface, thus more active sites are available for dioxygen binding, which leads to high ORR current. The Pt-alloy/C catalyst have exhibited 2 to 3 fold ORR activity when compared with Pt/C.

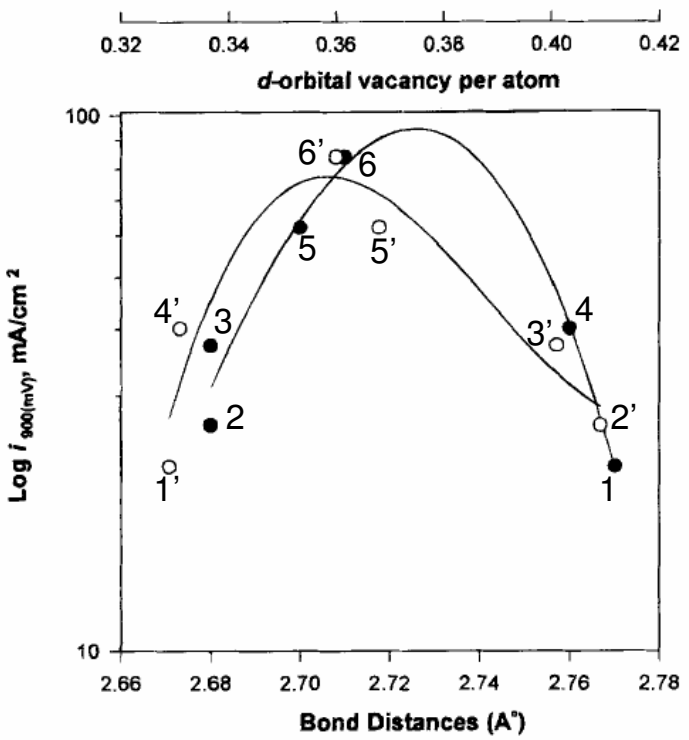

Fig. 1.4 Correlation of oxygen electrode performance (log i_{900mV}, mA/cm^2) of Pt and Pt-alloy electrocatalysts in a PEMFC with Pt-Pt bond distance (closed circles with numbering system 1-6) and the d-orbital vacancy of Pt (open circles with numbering system 1'-6') obtained from *in situ* XAS.

1,1'- Pt/C, 2,2'- PtNi/C, 3,3'- PtCo/C, 4,4' – PtMn/C, 5,5' – PtFe/C, 6,6' – PtCr/C.

(Reprinted from Ref. 5 with permission from the Electrochemical Society)

To minimize the contamination of the MEA during the operation of the PEMFC, Mukergee suggested the multiple leaching of the Pt-alloy catalyst.[1] Later, Gasteiger, et al. followed Mukergee's suggestions and investigated the cell performance with 47% Pt/C, unleached PtCo/C and, multiply-leached PtCo/C used as the cathode material.[1] Catalyst

PtCo/C with multiple leaching showed better ORR performance than the other catalysts. Unleached PtCo/C behaved better than Pt/C, but at higher current densities there was a slight drop in the Tafel slope obtained from the iR-free V-I curves due to the base metal contamination over the catalyst layer as shown in Fig. 1.5. Gasteiger, et al. have stated in their review that the leaching of basemetal from a Pt bimetallic catalyst may have an enrichment of Pt atoms on the first one or two monolayers.[1]

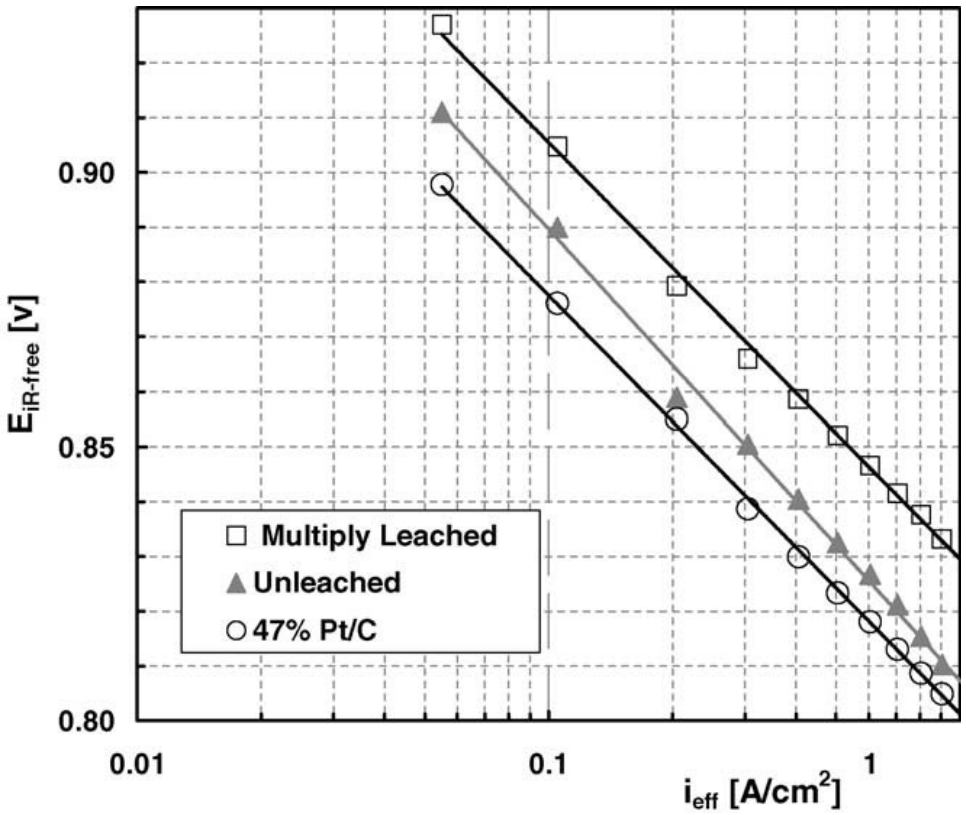

Fig. 1.5 iR-free (where R = resistance due to membrane, electronic components, and contact resistance) V–I curves measured in a PEMFC. The multiply-leached Pt_xCo_{1-x}/C shows the highest catalytic activity over the entire range of current densities as compared to Pt/C under similar operating conditions. All MEAs catalyst loadings of 0.4/0.4 mg_{Pt}/cm^2 nominal loading.

(Reprinted from Ref. 1 with permission from Elsevier)

An interesting debate on the improved ORR performance with the Pt-base metal alloy is whether the improvement is due to the modified electronic and structural properties of Pt-skin present over the Pt-alloy after the base metal leaching or due to the interplay of the surface Pt and the base metal composition. Stamenkovic, et al. tried to resolve this issue.[6] They showed that the magnitude of ORR kinetic current follows the order of Pt skin on Pt_3Co > Pt_3Co > Pt_3Ni > Pt in 0.1 M $HClO_4$ at 0.85 V. They also proposed that Pt skin on Pt_3Co modified the electronic property to resist the OH adsorption beyond 0.8 V. Moreover, the authors reasoned that the higher ORR kinetic current on Pt_3Co and Pt_3Ni than on Pt is due to the formation of "oxide"-covered Ni and Co atoms beyond 0.8 V which inhibited the Pt-OH_{ad} formation over the Pt sites and thus the Pt sites were set free.

Balbuena's calculations[7] based on density functional theory further support the above mentioned justification given by Stamenkovic for the improved ORR performance on Pt-base metal alloys.

Balbuena, et al. determined the binding energies of ORR intermediate species O, OH and the reaction product H_2O on Pt alloy clusters PtX, PtXX, PtPtX (X = Pt, Co, Ni or Cr) using the density functional theory.[7] The binding energy of the atomic oxygen follows the order of hollow sites of Ni_3 and Co_3 > hollow or bridge sites of PtPtX or PtXX > Pt_3. Their binding energy calculation shows that the Ni, Co and Cr in the alloy have a higher affinity towards OH, O and H_2O than the Pt sites. The authors proposed that the higher binding energy of base metals for oxygenated species supports the hypothesis that the oxygen electroreduction current on Pt-based bimetallic surfaces would be increased in the presence of these base metal atoms because of their ability to bind OH radicals and

water and to "free" precious Pt atoms which would become readily available for further O_2 reduction. The differences in binding energies for atomic oxygen, OH and H_2O between arrangements of atoms in specific bimetallic ensembles show the importance of geometric and electronic effects on the adsorption of intermediates of the oxygen electroreduction reaction.

There are some reports in the literature that provide justification for the improved ORR performance on Pt-base metal bimetallic alloy based on the facile O_2 dissociation rather than the scavenging effect of base metals towards oxygenated species. Xu, et al. have studied the adsorption of O and O_2 and the dissociation of O_2 on (111) facet of ordered Pt_3Co alloy and on Pt skin formed over Pt_3Co using the periodic density functional theory calculations. These reports also show that the binding energy of O and O_2 follow the order $Pt_3Co(111)$>Pt(111)>2% compressed Pt(111)>Pt skin on $Pt_3Co(111)$ (as shown in Fig. 1.6).[8] The higher surface binding energy of Pt_3Co for atomic oxygen and molecular oxygen compared to Pt helps achieve the facile dissociation of O_2, and hence we observe the improved ORR performance. These authors further proposed that due to the lowering of d-band center from the Fermi level on the surfaces of 2% compressed Pt, the Pt skin over $Pt_3Co(111)$ reduced the surface poisoning by the oxygenated species which resulted in the improved ORR performance, though O_2 dissociation was made difficult. Identical results were obtained on $Pt_3Fe(111)$ and on its Pt skin surface.[8]

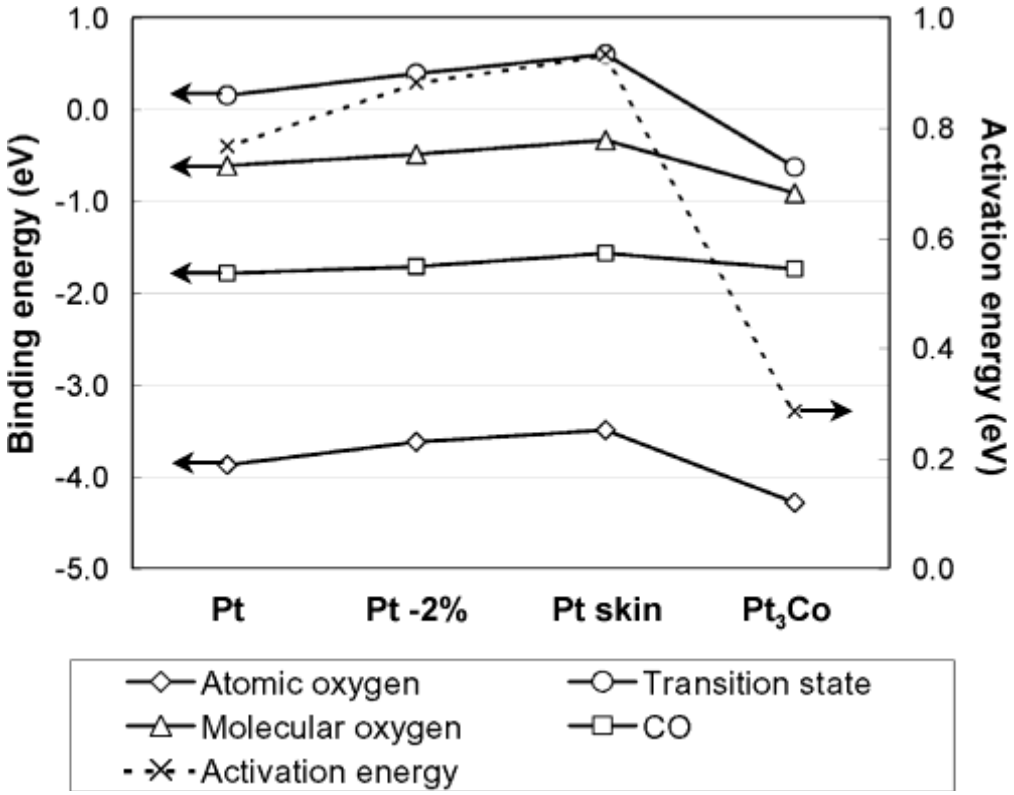

Fig. 1.6 Binding energies of O(a), O_2(a), and CO(a) and the transition states of O_2 dissociation on Pt(111), 2%-compressed Pt(111), Pt skin on Pt_3Co(111), and Pt_3Co(111). The corresponding O_2 activation energies are also included. The most stable state for each species and the transition state of the dissociation path with the smallest activation energy on each surface are shown. Lines are shown only as guides to the eye.

(Reprinted with permission from Ref. 8

The thermodynamic guidelines devised by Bard et al. for the design of ORR bimetallic catalysts also support the idea of facile O_2 dissociation by base metals on a bimetallic catalyst surface.[9,10] If the O_2 reduction pathway prefers the direct $4e^-$ reduction to H_2O, then there occurs an initial dissociative chemisorption of O_2 on the base metal

surface (as given in Equation 1) to form adsorbed oxygen atoms, which is believed to be the rate-determining step in the ORR mechanism.

$$2M + O_2 \rightarrow 2MO \quad (1)$$

These oxygen atoms are then transferred from the base metal (M) to the noble metal (M') as indicated by Equation 2.

$$2MO + 2M' \rightarrow 2M'O + 2M \quad (2)$$

In the next step, the oxygen atoms adsorbed on the noble metal atoms are electro-reduced to water as per Equation 3.

$$2M'O + 4H^+ + 4e^- \rightarrow 2M' + 2H_2O \quad (3)$$

Fig. 1.7 presents the tabulated data with the Gibbs free energy for reaction 1 and the standard potential for reaction 3.

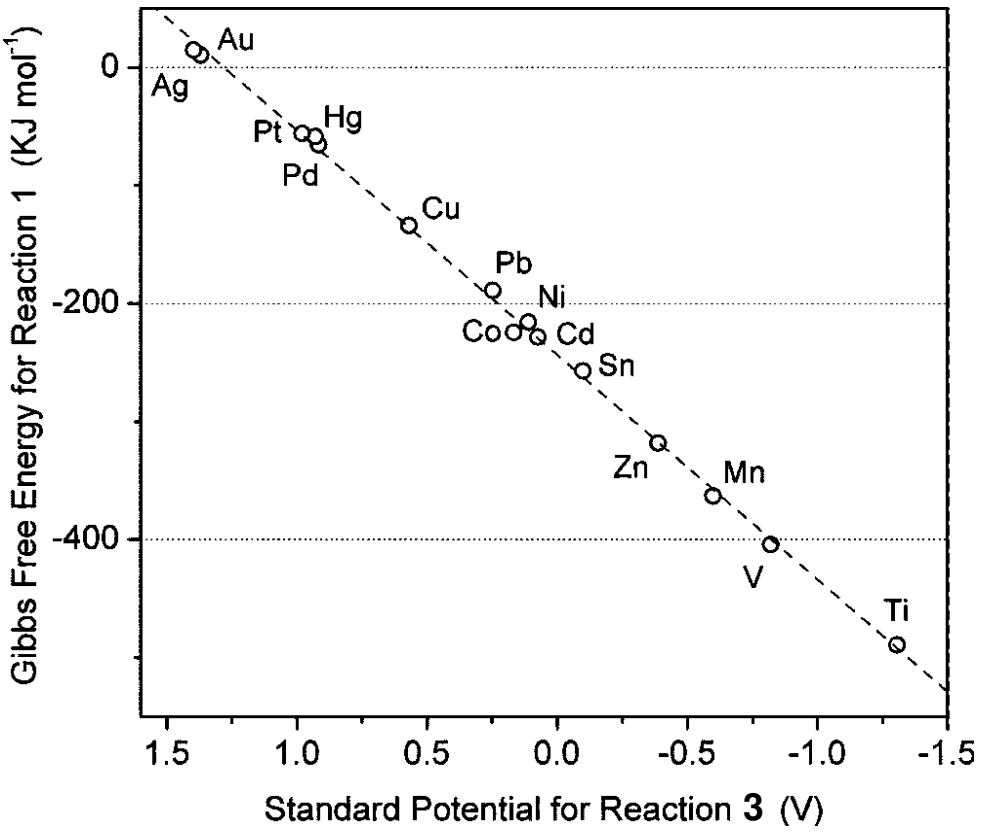

Fig. 1.7 Thermodynamic guidelines for bimetallic catalyst design for ORR (see the text for details). Reaction 1, $2M + O_2 \rightarrow 2MO$. Reaction 3, $2M'O + 4H^+ + 4e^- \rightarrow 2M' + 2H_2O$. (Reprinted from Ref. 10 with permission from the Electrochemical Society)

The metals in the lower right quadrant form a stable M-O bond requiring a negative potential for the MO reduction. The metals in the upper left quadrant form a less stable M'-O bond which can be reduced at positive potential. Based on the information shown in Fig. 1.7 Bard et al. propose to combine a better oxygen bond cleaving metal with another metal that is more efficient to reduce the adsorbed oxygen atom. Fig. 1.8a is a schematic illustration of ORR on a bimetallic catalyst based on the proposed thermodynamic guidelines. Fig. 1.8b illustrates how the cleaved oxygen atom migrates from the A-top site of M to a three-fold site involving M' on a bimetallic surface consisting of M and M'.

Bard et al. made various bimetallic alloys based on their thermodynamic guidelines and screened the various alloy composition for ORR using SECM.[9] For each metal examined (Ag, Au and Pd), addition of 10 to 20% Co resulted in enhanced ORR electrocatalytic activity.[9]

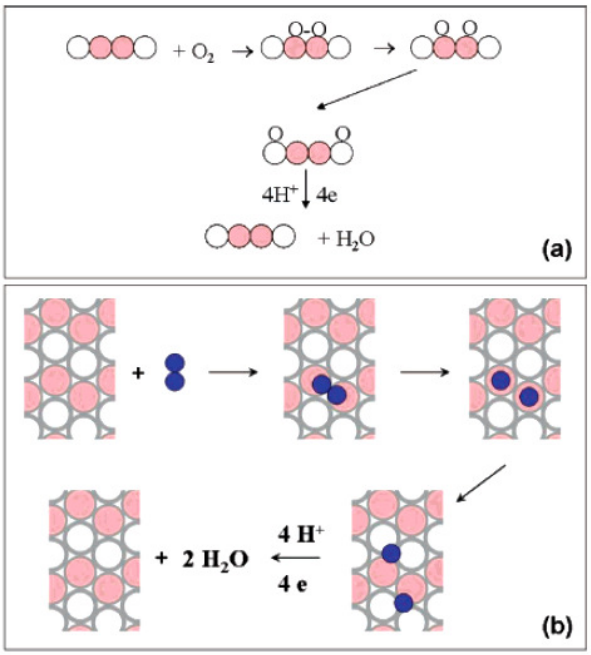

Fig. 1.8(a) Proposed synergetic mechanism for enhanced electrocatalysis using bimetallic surfaces. Closed circles represent good oxygen bond cleaving metal atoms (M) and open circles represent metal atoms that reduce adsorbed oxygen efficiently (M'). Small open circles represent oxygen atoms.

1.8(b) Top view schematic of the proposed mechanism. Large closed circles represent good oxygen bond cleaving metal atoms (M). Open circles represent metal atoms that reduce adsorbed oxygen efficiently (M'). Small closed circles represent oxygen atoms.

(Reprinted with permission from Ref. 9

Based on the thermodynamic guidelines provided by Bard, et al., Shannon, et al.

have developed a new electrocatalytic system where the base metal is placed in a metal coordinating inorganic ligand system which is further attached to the Pt surface by chemisorption.[11] Inorganic ligands such as polyoxometalates (POMs) contain oxidatively resistant metal-oxygen bonds and are stable at high positive potential of the cathode.[12] This helps to overcome the problem of base metal oxidation at high positive potential of the cathode during the fuel cell operation. As shown in Fig. 1.9, our group has studied the ORR activity and showed a shift of 26 mV in the $E_{1/2}$ potential on using Pt (Poly) with Co-substituted Dawson type phosphotungstate in the solution phase (0.1M $HClO_4$).[11] Leveraging the successful result with POM synergy on Pt(poly) for ORR into application for the PEMFC, POMs were combined with Pt nanoparticles using three synthetic approaches and the ORR kinetics were investigated in each method.

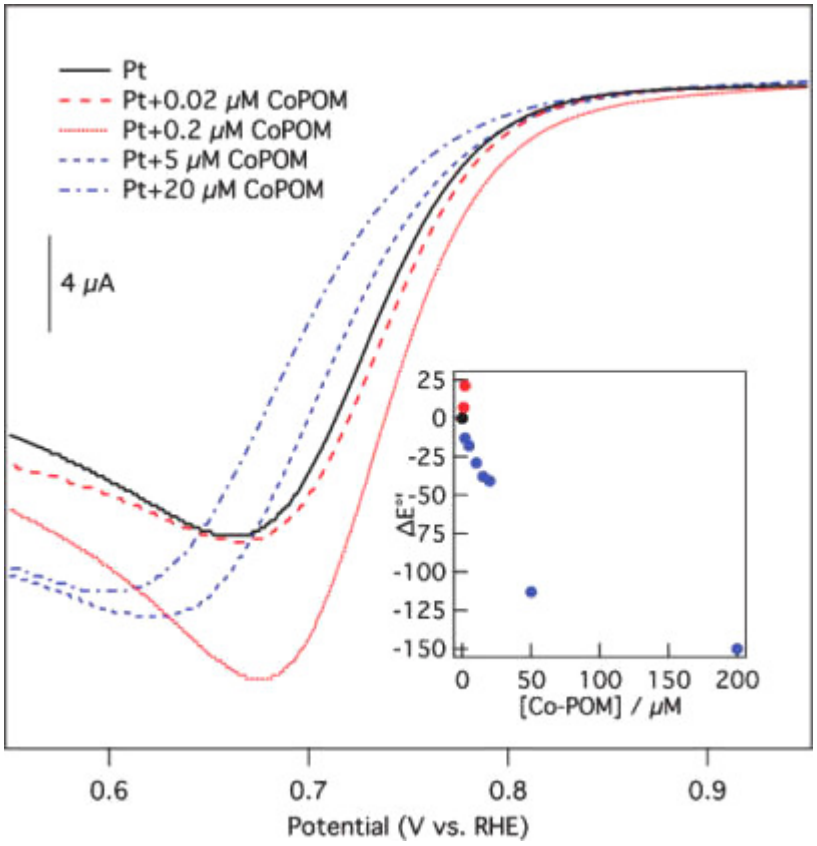

Fig. 1.9 Voltammetric response of a Pt electrode in O_2 saturated 0.1M $HClO_4$ as a function of [Co-Dawson]. Scan rate: 10 mV/s. Inset: plot of $\Delta E°'$ versus [Co-Dawson]. (Reprinted with permission from Ref. 11

Co-Dawson has to be incorporated along with Pt in the form of NP forming the catalyst layer in a PEMFC. In fuel cells, Pt in the form of NP is loaded on to the carbon particles to maximize Pt utilisation. Metal nanoparticles have been used for heterogeneous catalysis for over 50 years.[13] Catalytic reforming for the production of reformulated gasolines is one of the first processes that used metal nanoparticles as catalysts. Recently, metal nanoparticles have been widely applied as catalysts in the gas/solid and liquid/solid systems.[13]

POMs have received attention for ORR electrocatalysis because of their favorable properties when they are used along with the Pt. They have the ability to transfer their lattice oxygen atoms to a reactive species which can undergo oxidation.[14] The reduced POM can be reoxidized by accepting oxygen atoms from an oxidizing agent. This property is useful in catalyzing several organic oxidation reactions as well as the ORR. For example, divanadium substituted phosphomolybdate acts as a mediator by transferring its oxygen atom to anthracene and by regaining the donated oxygen atom from molecular oxygen.[15] Similarly, POMs containing a base metal can efficiently bind molecular oxygen in their base metal active site, split the O-O bond and transfer the split oxygen atom to the Pt surface. As POMs are strong Bronsted acids,[16] they can effectively conduct protons for the ORR reaction where the transfer of proton from the electrolyte to the Pt surface is necessary.[17] POMs are hydrolytically stable in acidic medium which also makes them suitable for fuel cell applications.[17,18] In addition, POMs can act as good mediators for multi-electron transfer reactions.[18]

In Co-Dawson, the Dawson-type phosphotungstate heteropolyanion acts as the inorganic skeleton for holding the Co^{2+}.[19] Dawson-type Phosphotungstate[20] was used for our control experiment. Fig. 1.10 shows the structure of Dawson. Mono substituted α_2-Co-Dawson (α_2 indicates that Co^{2+} occupies one of the cap octahedral positions in Dawson structure) was used in our studies.

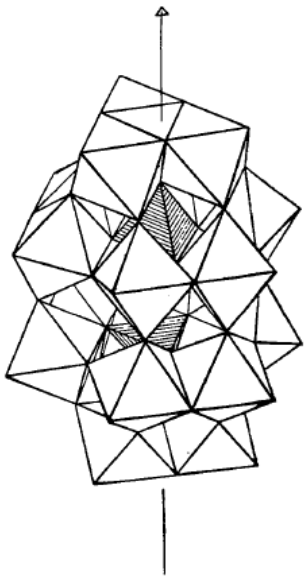

Fig. 1.10 Structure of Dawson type phosphotungstate $[P_2W_{18}O_{62}]^{6-}$

(Reprinted from Ref. 20 with permission from Wiley-Blackwell, Inc.)

Kulesza, et al. investigated the ORR electrocatalytic activity of Keggin-type Phosphotungstate (PW_{12}) and Phosphomolybdate(PMo_{12}) decorated Pt black (Pt black was obtained from Johnson and Matthew) based catalyst ink made with Nafion by supporting the ink directly on a rotating disc GC electrode.[17] In order to avoid the effect of POM adsorbed onto C, no carbon support (such as XC-72) was used to support the PtNP. The modification of Pt black surface by Keggin type PW_{12} and PMo_{12} POMs occurs through the chemisorption of these POMs on the Pt surface. It was reported that PW_{12} modified PtNP has shown enhanced ORR electrocatalytic activity compared with the unmodified PtNP, whereas the PMo_{12} modified PtNP shows reduced electrocatalytic activity for ORR, owing to the surface poisoning of the Pt active sites. These authors have reasoned that the difference in the cocatalysing property of PMo_{12} and PW_{12} on the Pt surface is due to the varying adsorption property of these POMs on the Pt surface. Further

studies are required to confirm this. It has been shown that POMs interact with the Pt surface atom through their terminal oxygen atoms. The literature supports the chemisorption of POM on the noble metal surface.[21-23]

Based on this fact, POM-stabilized metal nanoparticle were prepared by the $NaBH_4$ reduction method.[24] (Experimental details provided in chapter 2). Rice et al. have reported that the carbon can influence the electronic property of the supported PtNP.[25]

POM has the ability to chemisorb on carbon materials,[26-28] and this chemisorption may influence the electronic properties of POM by modifying structural properties.[28] We decided to investigate the ORR kinetics (in Chapter 2) using the Co-Dawson and Dawson-stabilized PtNP without the carbon support, since we are studying the synergetic effect of Co-Dawson or Dawson on PtNP. On testing the ORR performance, we concluded from the high kinetic current of Co-Dawson-stabilized PtNP that Co centers in Co-POM helps with O-O bond splitting and transfers the split O atom to the Pt NP surface. However, the ORR onset potential was found to be more negative than the commercial Pt catalyst. This is possibly due to active site-blocking of POM chemisorbed on the PtNP surface. To overcome this problem, we planned to combine the POM and PtNP using the layer-by-layer (LBL) technique (Fig. 1.11)[29] where the negatively charged POM and the positively charged stabilizer surrounding the PtNP will be in electrostatic interaction.

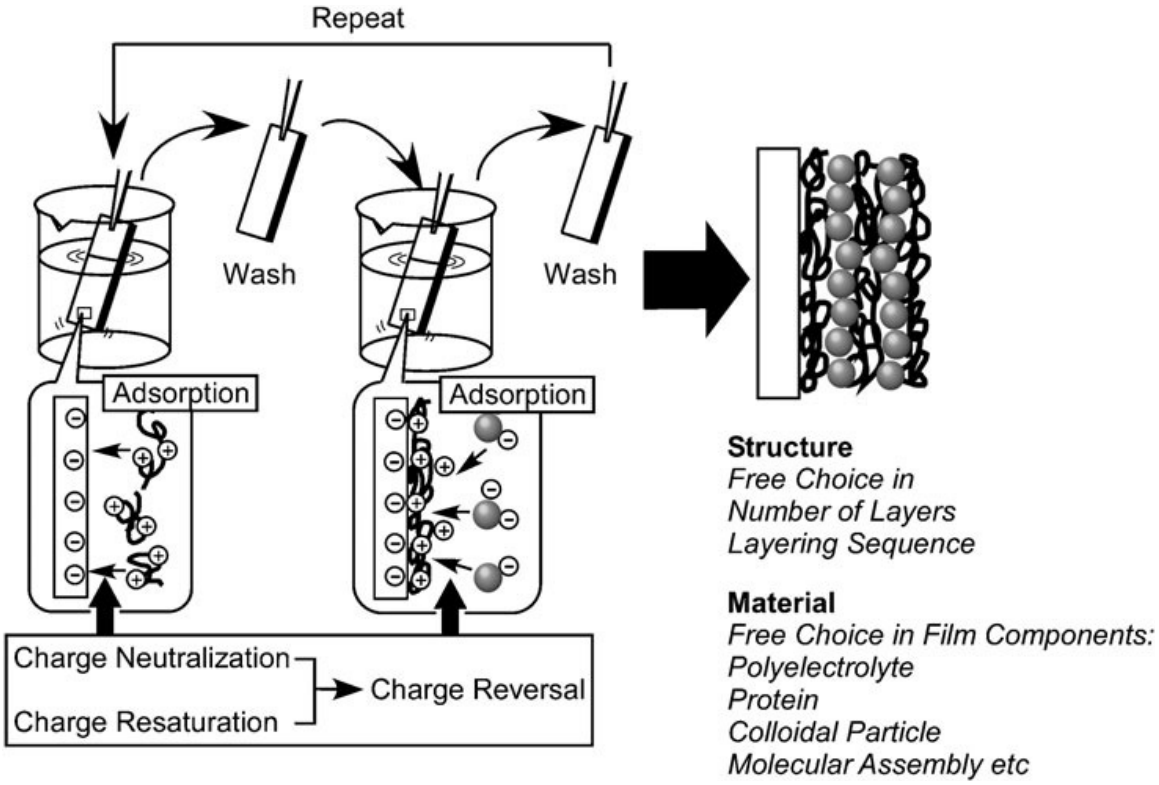

Fig. 1.11 Outline of LBL assembly through electrostatic interaction.

(Reprinted from Ref. 29 with permission from RSC Publishing)

For our second approach, therefore, we prepared protonated cysteamine (a thiol) stabilized Pt NP[30] and assembled with POM. On testing the ORR performance, we realized from the low kinetic current that the thiol chemisorption on Pt surface altered the electronic property similar to the thiol adsorption on Au as reported by Büttner, et al.[31] and Calzolari, et al.[32] and blocked the active site for molecular oxygen to bind. For our third approach, we prepared Pt NP stabilized by PDDA which has the reversible binding ability to allow for the reactive species.[33,34] The layer-by-layer approach for constructing the electrocatalyst also has the additional advantage of thinning the catalyst layer[35] which can reduce the mass-induced voltage losses in the fuel cell by meeting the triple phase

boundary condition, where the Pt nanoparticle can be in contact with the electronic conductor (Vulcan carbon), protonic conductor (Nafion), and the gaseous oxygen. In practice, most of the Pt active sites are not utilized in the catalyst layer.[35] The particles are either trapped inside the pores of Vulcan carbon during the preparation of Pt/C by the wet impregnation and chemical reduction method or they may not be in the triple-phase boundary region as shown in Fig. 1.12.[35-37]

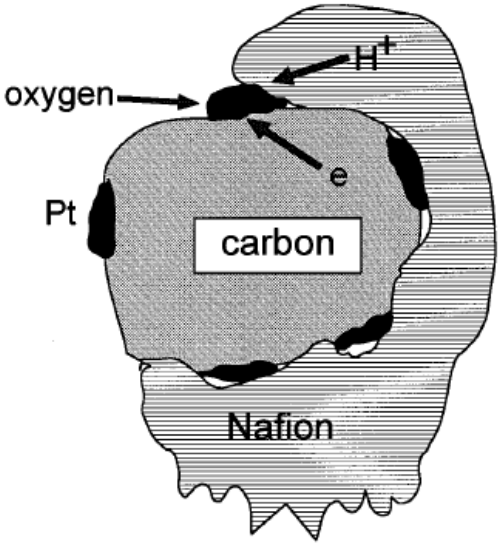

Fig. 1.12 Schematic diagram of the 'state of the art' PEMFC catalyst illustrating the scarcity of the triple phase boundary.

(Reprinted from Ref. 37 with permission from Elsevier)

Increasing the Pt loading on Vulcan carbon in order to reduce the thickness of the catalyst layer increased the particle size of Pt formed on carbon support which could suppress the performance of the fuel cell.[38] Gratiet et al. have reported that the commercially available Pt/C from E-TEK Inc. has a particle size of 2 nm with 10% loading of Pt, 3.2 nm with 30% loading of Pt, and 8.8 nm with 60% loading of Pt.[38]

Recently, Taylor, et al. have fabricated a catalyst layer consisting of PtNP supported on CNT and polyelectrolytes(such as Nafion, polyaniline and polyethyleneimine) using the layer-by-layer(LBL) assembly.[35] The Pt – specific power density obtained was 3198 mW/mg_{Pt}. This is much higher than the one obtained with the conventional membrane electrode assembly (800 mW/mg_{Pt}). This LBL technique is very attractive as it allows the homogeneous assembly of various materials into a thin film.[29,35] Although this method is more time consuming than the conventional method of catalyst preparation, it is simple and cheap, and the maximum Pt utilization helps to reduce the cost of the PEMFC.[35]

1.3 Fabrication of alloy gradient for the best material selection to be applied in sensors and in fuel cells:

1.3.1 Significance of combinatorial material library in the field of material science:

The discovery and engineering of new materials have become essential factors in meeting society's needs for material comfort. Their structure and composition serve as the platform for engineering any new material and thus modern materials like ceramics, polymers, composites, semiconductors, metals and alloys, and biomaterials find application in various fields depending on their properties.[39] If materials are produced and investigated by a traditional mode of sequential preparation, the probability of discovering a new functional material with leading qualities will be greatly reduced. It became possible to discover novel, efficient materials in large quantities with varying physical and chemical properties with the help of the combinatorial material synthesis approach and, as a result, it also became possible to achieve high-throughput synthesis and screening of functional materials such as superconductors, magnetoresistors, photolumonescent solids.[39-41]

A combinatorial material library is a large collection of different materials that vary in their composition or other properties such as optical, electronic, dielectric and catalytic activity.[40] The combinatorial material library can be created either as a spatially-resolved discrete one - or two-dimensional array of materials with varying properties or as a continuous composition spread where an unbroken graded material is generated.[40]

The idea of combinatorial material synthesis was first observed in a biological process in which our human immune system generates 10^{14} antibodies and screens them to find the perfect binding match for the invading virus in order to deactivate it. This basic approach was applied in biochemistry and by the drug industry and later in other fields of chemistry and material science to find the right chemical or material for a particular application.[39]

The combinatorial strategy which helps to screen a large number of samples with precise measurement under equivalent operating conditions not only identifies the material with the optimum property but also demonstrates a systematic relationship between the structure-composition and the properties of the material.[39-41]

The development of microprobe techniques such as microspot X-ray methods, various optical measurement techniques, and a novel evanescent microwave microscope, led to the growth of combinatorial material libraries by characterizing materials at a microscopic level.[41]

Alloys are important functional materials whose mechanical, electrical, magnetic, thermal and catalytic properties are interesting to study as they are applied as construction materials, conductors in electrical components, electromagnetic field oriented instruments (e.g. electric motors), thermocouples, and catalysts in reactors.

Much work has been done in fabricating and screening a combinatorial library of alloys in order to get the best performing composition with the desired property.[41]

1.3.2 Methods to generate the alloy gradient:

Combinatorial alloy libraries are primarily constructed by inkjet printing method[42], wherein the thickness of the ink containing the constituent metal precursor is varied laterally and reduced subsequently with a suitable reducing agent or a designed printing pattern. The process is then repeated with the ink containing constituent metal precursor(s) according to the alloy composition with subsequent reduction, off-axis co-deposition of constituent metals on a single substrate,[41] a combination of masking technique and a rotating ablating target,[40,41] and electrochemical techniques.[43-45]

Generating alloy gradients by the electrochemical technique is a cheap and simple method. People have adopted several strategies to generate the alloy gradient using the electrochemical technique. Hillier and his co-workers have made a binary[43] or ternary[44] alloy gradient spread on an ITO substrate by creating a lateral concentration gradient of a metal precursor using the gel diffusion process, while holding the other metal precursors at a uniform concentration inside the gel and depositing the precursors under a diffusion limited rate (Fig. 1.13).

The formed alloy gradients (Pt_xRu_y, $Pt_xRu_yRh_z$) were screened using SECM or pH sensitive fluorescence for the optimum composition to be used as anode catalyst in fuel cells.

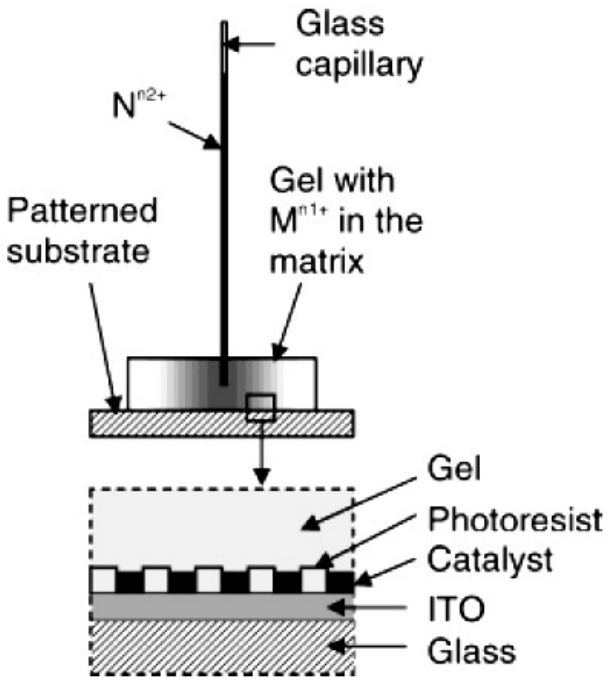

Fig. 1.13 Schematic representation of an alloy gradient generation by the gel diffusion process.

(Reprinted with permission from Ref. 43

Copyright © 2004, American Chemical Society)

Rubinstein's research team came up with a new way of generating the alloy gradient (Pd-Au) where a lateral potential gradient is established over the electrode surface with a uniform concentration of metal precursor all over the electrode surface.[45] Fig. 1.14 shows the experimental set-up used by Rubinstein et al. to establish the lateral potential gradient. A 35 nm gold thin-film sputter coated at one side of a Nanoporous Alumina Membrane (NAM) where it is branched with 0.02 micrometers from a pore diameter of 0.22 micrometers acted as the cathode. A graphite rod served as the counter electrode and an saturated calomel electrode (SCE) served as the reference electrode. Using a power source (9V battery), an in-plane current was passed through the gold thin film between the two

desired points where one point is connected to the potentiostat to maintain the desired potential and the other point is brought to the desired value by regulating the in-plane current passed through the gold film. Thus, a lateral potential gradient is established on the surface of a gold thin film and the deposited Au-Pd alloy grows within the pores of the membrane in the form of wires.

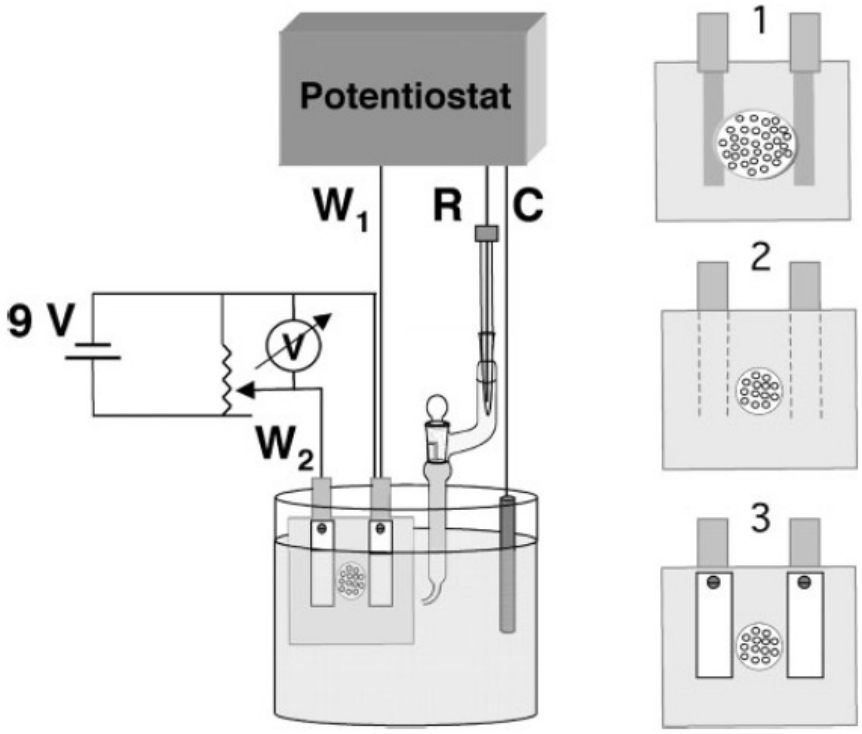

Fig. 1.14 Left: The cell and the electrical circuit used to generate the alloy gradient by the electrodeposition method. *W*1 and *W*2 - the two contacts to the working electrode; *R*-reference electrode and *C* - counter electrode. Right: Steps in the preparation of the working-electrode connections: 1) The Au-coated side of the membrane is placed on two Au contacts. 2) The membrane is covered with a Teflon plate that has a hole in the center (diameter = 4 mm). 3) The plate is fastened using two Teflon bands.

(Reprinted from Ref. 45 with permission from John Wiley and Sons, Inc.)

Fig. 1.15 shows the cyclic voltammograms corresponding to the Au deposition, Pd deposition, and Pd-Au deposition on a gold substrate from an acidic chloride bath.[45] Rubinstein et al. chose the potential range (0.5 V to 0.2 V vs SCE) which covers the less noble metal Pd getting deposited under a kinetically controlled rate along with Au getting deposited under the diffusion limited rate. The composition gradient obtained ranged from 85% Au-15%Pd to 53%Au-47%Pd for the chosen potential gradient 0.5V to 0.2V vs the SCE.

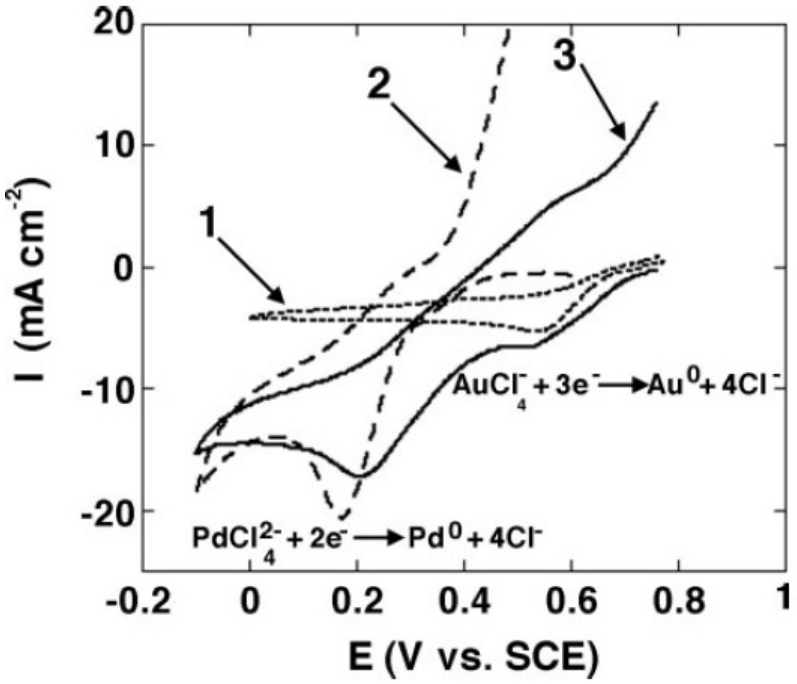

Fig. 1.15 Cyclic voltammograms (first scan) recorded in 1) 10 mM $HAuCl_4$ + 0.5 M HCl; 2) 25 mM H_2PdCl_4 + 0.5 M HCl; and 3) 10 mM $HAuCl_4$ + 25 mM H_2PdCl_4 + 0.5 M HCl solutions. The working electrode: 35 nm Au film evaporated on a NAM. Scan rate: 50 mV/s. All scans started in the negative direction.

(Reprinted from Ref. 45 with permission from John Wiley and Sons, Inc.)

The surface composition gradients prepared by the Gel-Transfer deposition[43,44] and

the templated synthesis of graded alloy material using the in-plane potential gradient[45] were a good start for the combinatorial discovery of alloy gradients. At the same time, these methods do have drawbacks. Though the gel transfer method is desirable because of its simplicity, there's a possibility for the surface and bulk composition to vary due to the hindrance offered by the gel material for the diffusion process. The method of templated synthesis of graded alloy material can be applied only on a thin film substrate and a special design, such as NAM, is needed to create the graded alloy material in order to maintain the lateral potential gradient which would otherwise decrease the resistivity of the electrode to the in-plane current as a result of the increased thickness obtained during the alloy deposition. Removal of NAM will not give a solid substrate which consists of all the graded alloy materials.

Our group has fabricated a material library based on a binary system using the lateral potential gradient established with the help of bipolar electrochemistry.[46] This method needs a simple power source with a flexible bipolar electrochemical cell design. There is no limitation on the thickness of the floating electrode; in addition there is no need for any template in generating the graded material. Solution composition can be optimized to achieve quality deposits.

1.3.3 Principles of bipolar electrochemistry for generating material gradients:

In a three-electrode configuration which involves a working electrode, counter electrode, and a reference electrode, the galvani potential of the working electrode is controlled using a potentiostat against a reference electrode in order to maintain the interfacial potential or the electrode potential which acts as the driving force for the redox reactions.[47,48]

In a bipolar electrode configuration, the solution potential is controlled by establishing an electric field in the solution using a power supply or a battery; also the bipolar electrode will be floating and so its galvani potential will not be disturbed. [47] Though the working principles are different in both the configurations, the driving force for the redox reactions will be the interfacial potential at the electrode surface.[47] As shown in Scheme 1.1, the bipolar electrode is kept at the center of a microfluidic channel containing the electrolyte. A potential difference of E_{tot} is applied between the microfluidic channel using the two-driver electrodes kept at the two extreme ends of the microfluidic channel. An electrode potential of E_{elec} exist at all points before the application of E_{tot}. When E_{tot} is applied, the electrode potential becomes more negative than the electrode equilibrium potential (E_{elec}) upon modulating the solution potential which leads to a gradient cathodic overpotential from the center towards the cathodic pole of the bipolar electrode. The electrode potential becomes more positive than E_{elec} leading to a gradient of anodic overpotential from the center towards the anodic pole of the bipolar electrode. The difference between the electrode potential at the anodic and cathodic ends of the bipolar electrode is denoted as ΔE_{elec}. In the case of sufficient anodic and cathodic overpotentials for the electrochemical reactions to occur, the reduction reaction at the cathodic pole and the oxidation reaction at the anodic pole should balance each other in terms of the total number of electrons transferred per unit time in order to maintain electroneutrality within the bipolar electrode. The current passing through the bipolar electrode is denoted as I_{elec}.

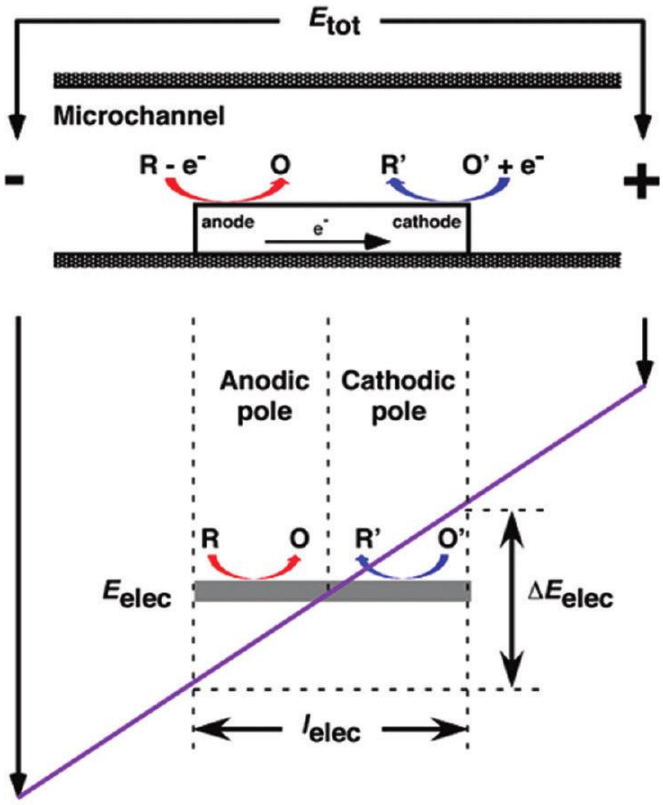

Scheme 1.1 Development of lateral electrode potential gradient on bipolar electrode.

(Reprinted with permission from Ref. 47

Copyright © 2010, American Chemical Society)

1.3.4 Development of bipolar electrochemistry and its application in combinatorial material library fabrication:

Bipolar electrochemistry was first brought into application for the electrochemical synthesis of compounds in packed-bed reactors, when particulate electrodes got more attention in considering yield. In 1977, Goodridge and co-workers demonstrated the behavior of bipolar packed-bed electrodes for the production of hypobromite and epoxidation of styrene.[49]

The bipolar mode of operation in the packed- or fluidized-bed will be suitable to

carry out reactions in a poorly conducting medium, which is associated with organic synthesis. Each particle that is electrically isolated in the packed-bed acts as a bipolar electrode and a uniform potential distribution exists all over the reactor, which was made possible by taking advantage of the high ohmic drop in a poorly-conducting medium between the feeder electrodes which would have been difficult to operate in a monopolar packed-bed reactor. Thus the bipolar electrolysis is important for the reaction yield.[49]

Though there was not much progress in the field of bipolar electrochemistry in the 1980's and the early 1990's, for the past 15 years bipolar electrochemistry has found several interesting applications based on its advantageous features such as the "wireless operation" and the "simple instrumentation". With the invention of microfabrication techniques it has become possible to miniaturize conventional analytical equipment such as the capillary electrophoresis (CE), a separation technique, and other techniques for realizing the benefits of miniaturized devices. Electrochemical detection systems can be much more readily integrated into the miniaturized devices than can optical detection systems. To commercialize a device and to make it portable, the detector system also has to be miniaturized.[50] Arora, et al. have used the Electrochemiluminescence (ECL) process (detected by a charge coupled device (CCD) camera or a photomultimultiplier tube) occuring on an electrically floating Pt electrode (called as bipolar electrode), as a wireless miniaturized integrated detecting system with the miniaturized capillary electrophoresis device on a chip.[50] When a huge electric field was applied along the CE separation column, anodic and cathodic reactions were induced on the Pt bipolar electrode. The anodic ECL reaction was used as the photonic reader for the direct detection of analytes which are involved in the ECL reaction. It was possible to indirectly detect the analytes

which are ECL inactive by taking the ECL active species along with the buffer in the column and reading its negative signal.

Arora's use of the ECL photonic reader on the miniaturized bipolar electrode as part of the detecting system in the miniaturized CE helped to solve the issue of an unfavorable background signal associated with the conventional electrochemical detector (three electrode configuration operated by a potentiostat) used in the separation column.[50]

Later, miniaturized bipolar electrodes were applied in microfluidic devices to detect a wide range of ECL inactive analytes which can undergo reduction at the cathodic pole of the bipolar electrode through the electrical coupling of the ECL process occurring at the anode pole of the electrode (Scheme 1.2).[51] The ECL photonic reader helps with the accurate quantification of the analyte due to its high sensitivity. This device can be operated using a simple power supply or a battery.[51]

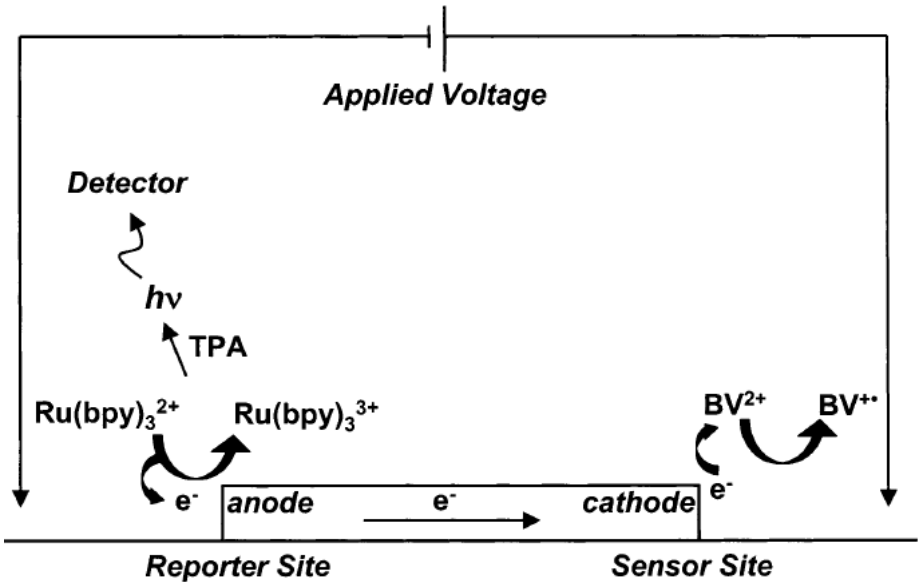

Scheme 1.2 Bipolar ECL photonic reader for cathodically reduced analytes

(Reprinted with permission from Ref. 51

Copyright © 2002, American Chemical Society)

In addition to the chemical and biosensor fields, bipolar electrochemistry has also been applied in the microfabrication of metal structures,[52] site-specific modification of carbon nanotubes (CNT),[53] and surface modification with graded materials.[46,54]

Lateral potential gradient plays an important role in modifying the electrode surface with the graded material using the bipolar electrochemistry. Based on the principle that the property of the material electrodeposited depends on the electrode potential, a material gradient is formed along the length of the bipolar electrode. This phenomenon can be utilized for combinatorial material library fabrication. Using the lateral potential gradient, a molecular gradient has been achieved by Ulrich et al. on a gold bipolar electrode which has a uniform self assembled monolayer (SAM) of HS-C_2H_4-(O-C_2H_4)$_6$-OCH_3 (mPEG) molecules.[54] The SAM molecules are reductively desorbed at the cathodic end of the Au bipolar electrode under the lateral potential gradient created by applying an electric field between the two stainless steel electrodes. The SAM molecular gradient has been further transformed into a surface protein gradient by backfilling the desorbed self assembled monolayer region with HS-C_2H_4-(O-C_2H_4)$_8$-COOH (aPEG) and subsequent linking of the terminal –COOH groups with the Lysozyme protein through succinimide activation. Each step in this procedure for generating the protein gradient was followed by imaging-null-ellipsometry (Fig. 1.16).[54]

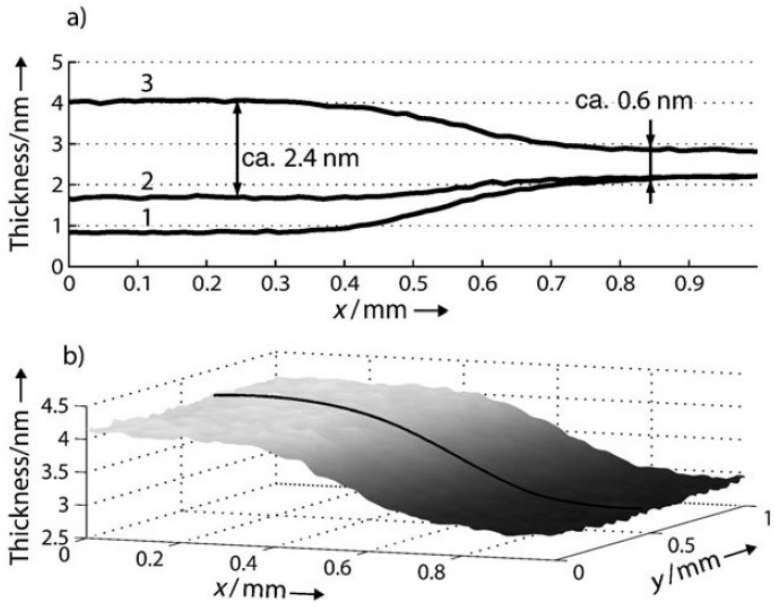

Fig. 1.16 a) Line profiles, obtained from imaging-null-ellipsometry measurements, in which the thicknesses of the gradients observed after the different preparation steps are shown. Line 1 exhibits the result of the desorption of mPEG, line 2 shows that obtained after backfilling with aPEG, and line 3 represents the resulting protein gradient. b) Thickness map of the protein gradient (the line shows the region from which the line profile was taken).

(Reprinted from Ref. 54 with permission from Wiley-VCH Verlag GmbH & Co. KGaA, Weinheim.)

Our group has fabricated the solid state one-dimensional material library on a gold bipolar electrode using the CdS binary system.[46] The binary material was electrodeposited at the cathodic end of the bipolar electrode and screened using resonance Raman microscopy and Auger electron spectroscopy. As expected, based on thermodynamic considerations, the characterizing techniques confirmed the three distinct regions as shown in Fig. 1.17A Starting from the cathodic end towards the center of the bipolar

electrode the three regions were as follows: (i) CdS+Cd (grey), (ii) stoichiometric CdS (orange) and (iii) elemental S (yellow).

Spots 1 to 7 denote the locations where Auger Electron Spectroscopy(AES) measurement (Fig. 1.17B) was taken and spots A to E denote the locations where resonance Raman was captured (Fig. 1.17C). The peak at 300 cm^{-1} in the Raman spectrum indicates the longitudinal optical phonon (LO) band of CdS and the peak at 600 cm^{-1} indicates its overtone. The low intensity of the LO band in spectrum A, C, D confirms that CdS is not present in a 1:1 stoichiometric ratio. The high intensity of LO band in spectrum B indicates that CdS is present in a 1:1 stoichiometric ratio. The broad band at 420 cm^{-1} in spectrum C indicates the excess S in CdS. The Raman results agree with the AES results given in Fig. 1.17B and hence a binary material library is established using the lateral potential gradient along the length of the bipolar electrode.

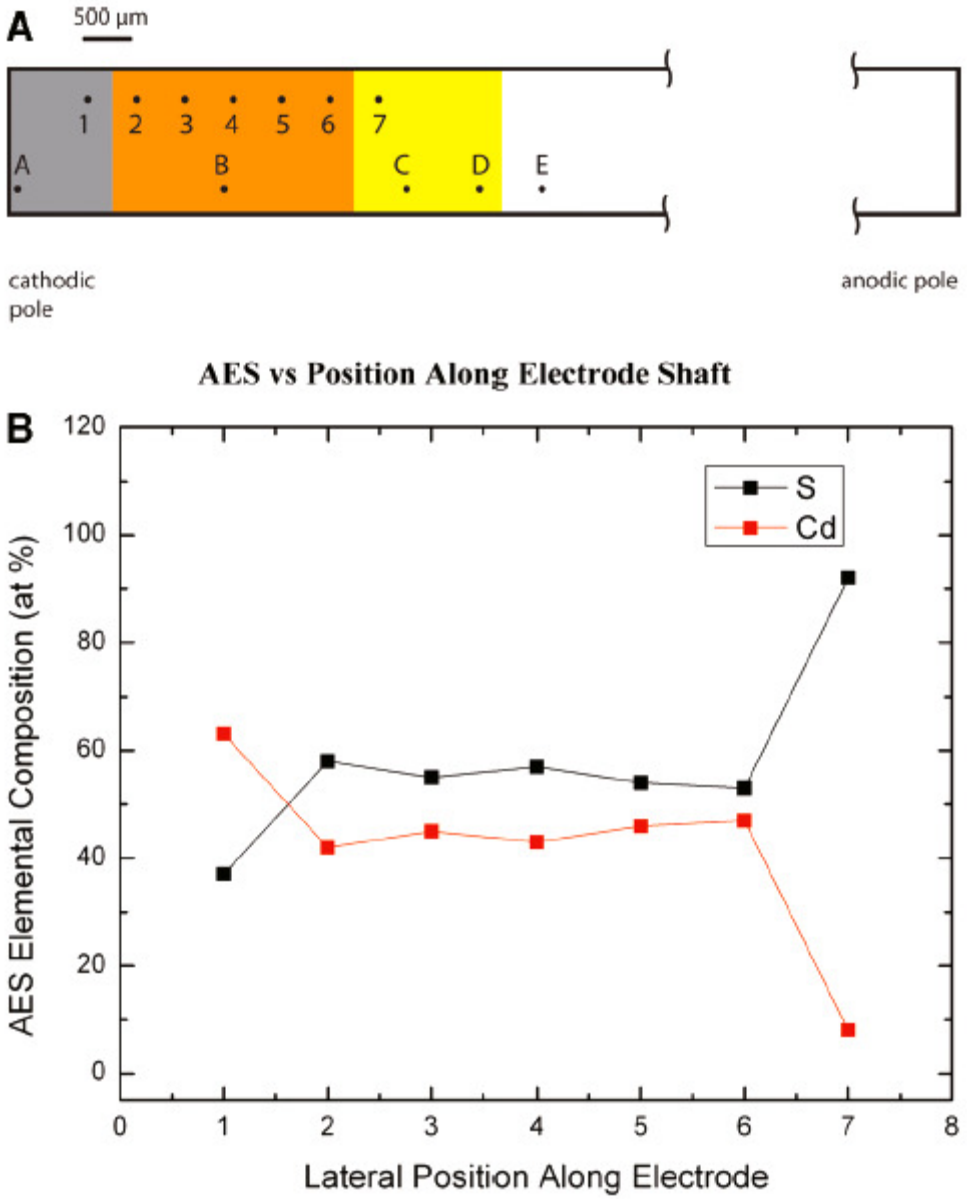

Fig. 1.17 (A) Diagram of the geometry used for AES and Raman analysis. (B) Plot of the AES atomic percentage of Cd and S as a function of lateral position along the bipolar electrode (BPE). The geometry of the analysis locations (for spots 1-7) is shown in Fig. 1.17A.

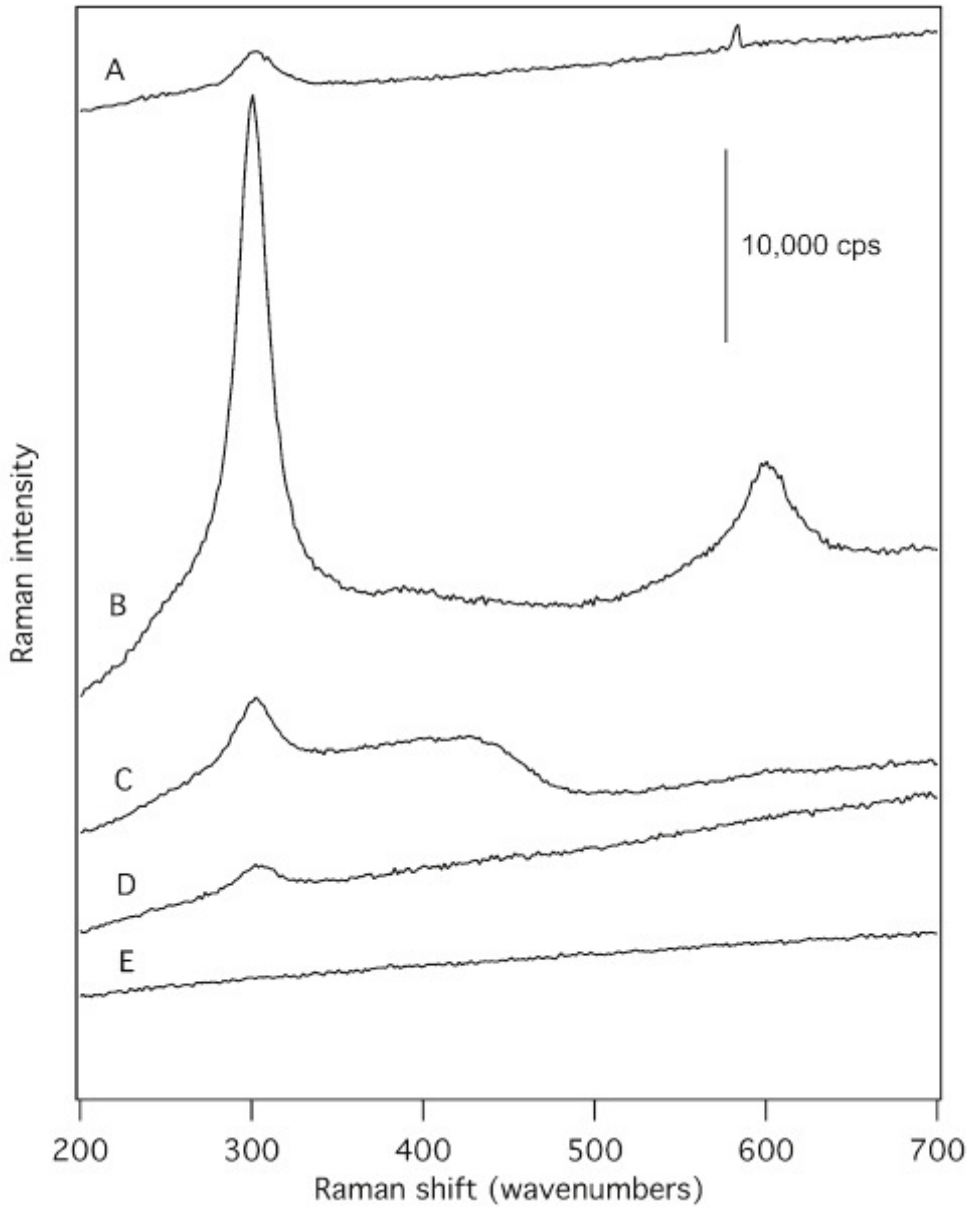

Fig. 1.17C Representative resonance Raman spectra collected at various points along the bipolar electrode using a confocal microscope. The geometry of the analysis locations (for spectra A-E) is shown in Fig. 1.17A.

(Reprinted with permission from Ref. 46

This approach was further applied to create other functional materials, such as the alloy gradient, to find the lead material using high- throughput screening techniques.

According to Faraday's Law, the instantaneous composition of a binary alloy depends on the partial current for the electrodeposition of each metal. In order to achieve a graded alloy composition, it is necessary to co-deposit two metals with different reduction potentials. The more noble metal gets deposited at a more positive potential and reaches the diffusion-limited deposition rate while at the same time the less noble metal starts to get deposited under the kinetically controlled rate. This region, where the less noble metal is deposited under the kinetically controlled rate while the more noble metal is deposited under the diffusion-limited rate, is of interest for obtaining the gradient of alloy composition as per the Faraday's Law. This effect results from the variation in the partial current of the less noble metal, where the partial current of the more noble metal is maintained constant. In the potential region more positive to the aforementioned region no co-deposition occurs, and in the potential region less positive to this defined region there is no variation in the partial currents of the co-depositing metals, resulting in a constant composition of the alloy getting deposited.

Based on the fundamental principles of the bipolar electrochemistry and the Faraday's Law for the alloy deposition described in the above sections, we generated Ag-Au and Pd-Au alloy gradients on a bipolar electrode and screened the optical and catalytic properties using micro Raman spectroscopy. The obtained results are described in Chapter 3 (Ag-Au) and Chapter 4 (Pd-Au).

References:

(1) Gasteiger, H. A.; Kocha, S.S.; Sompalli, B.; Wagner, F.T. *Applied Catalysis B: Environmental* **2005**, *56*, 9–35.

(2) Bockris, J. O'M.; Srinivasan, S. *Fuel Cells: Their Electrochemistry*, McGraw-Hill, New York, 1969.

(3) Appleby, A. J. *Catal. Rev.* **1970**, *4*, 221-243.

(4) Jalan, V.; Taylor, E. J. *J. Electrochem. Soc.*, **1983**, *130*, 2299-2302.

(5) Mukerjee, S.; Srinivasan, S.; Soriaga, M. P.; McBreen, J. *J. Electrochem. Soc.* **1995***, 142*, 1409-1422.

(6) Stamenkovic´, V.; Schmidt, T. J.; Ross, P. N.; Markovic´, N. M. *J. Phys. Chem. B* **2002,** *106,* 11970-11979.

(7) Balbuena, P. B.; Altomare, D.; Vadlamani, N.; Bingi, S.; Agapito, L.A.; Seminario, J. M. *J. Phys. Chem. A* **2004,** *108,* 6378-6384.

(8) Xu, Y.; Ruban, A. V. ; Mavrikakis, M. *J. Am. Chem. Soc.* **2004**, *126*, 4717-4725.

(9) Fernandez, J. L.; Walsh, D. A.; Bard, A. J. *J. Am. Chem. Soc.* **2005**, *127*, 357-365.

(10) Walsh, D. A.; Fernandez, J. L.; Bard, A. J. *J. Electrochem. Soc.* **2006**, *153*, E99-E103.

(11) Sankarraj, A. V.; Ramakrishnan, S.; Shannon, C. *Langmuir* **2008,** *24,* 632-634.

(12) Hill, C.L.; Brown, R.B. *J. Am. Chem. Soc.* **1986***, 108,* 536.

(13) Pachón.L. D.; Rothenberg, G. *Appl. Organometal. Chem.* **2008**, *22*, 288–299.

(14) Mioc, U.B.; Todorovic´, M.R.; Davidovic´, M.; Colomban, Ph.; Holclajtner-Antunovic´, I. Solid State Ionics **2005**, *176*, 3005 – 3017.

(15) Khenkin, A.M.; Weiner, L,; Wang, Y.; Neumann, R. *J. Am. Chem. Soc.* **2001,** *123,* 8531-8542.

(16) Borrás-Almenar, J. J.; Coronado, E.; Müller, A. *Polyoxometalate Molecular Science*, Kluwer Academic Publishers, Netherlands. 2001.

(17) Chojak, M.; Kolary-Zurowska, A.; Wlodarczyk, R.; Miecznikowski, K.; Karnicka, K.; Palys, B.; Marassi, R.; Kulesza, P. J. *Electrochim. Acta* **2007**, *52*, 5574-5581.

(18) Sadakane, M.; Steckhan, E. *Chem. Rev.* **1998,** *98,* 219-237.

(19) Kharat, A. N.; Pendleton, P.; Badalyan, A.; Abedini, M.; Amini, M. M. *J. Mol. Catal. A: Chem.* **2001**, *175*, 277-283.

(20) Dawson, B. *Acta Crystallogr.* **1953**, *6*, 113.

(21) Lica, G. C.; Browne, K. P.; Tong, Y. Y. *Journal of Cluster Science*, **2006**, *17*, 349-359.

(22) Ge, M.; Zhong, B.; Klemperer, W. G.; Gewirth, A. A. *J. Am. Chem. Soc.* **1996,** *118,* 5812-5813.

(23) Timofeeva, E. V.; Tsirlina1, G.. A.; Petrii, O. A. *Russian Journal of Electrochemistry* **2003**, *39*, *716–726.*

(24) Biella, S. ; Porta, F. ; Prati, L. ; Rossi, M. *Catalysis Letters*, **2003**, *90*, 23-29.

(25) Rice, C.; Tong, Y.; Oldfield, E.; Wieckowski, A..*J. Phys. Chem. B* **2000,** *104,* 5803-5807.

(26) Kuhn, A.; Anson, F. C. *Langmuir* **1996,** *12,* 5481-5488.

(27) Klemperer, W. G.; Wall, C. G.. *Chem. Rev.* **1998,** *98,* 297-306.

(28) Pan, D.; Chen, J.; Tao, W.; Nie, L.; Yao. S. *Langmuir* **2006,** *22,* 5872-5876.

(29) Ariga, K.; Hill, J. P.; Ji, Q. *Phys. Chem. Chem. Phys.*, **2007**, *9*, 2319–2340.

(30) Eklund, S. E.; Cliffel, D. E. *Langmuir* **2004,** *20,* 6012-6018.

(31) Büttner, M.; Kröger, H.; Gerhards, I.; Mathys, D.; Oelhafen, P. *Thin Solid Films* **2006**, *495*, 180 – 185.

(32) Calzolari, A.; Felice, R. D. *J. Phys.: Condens. Matter* **2007**, *19***,** 305018-305028.

(33) Jiang, S. P.; Liu, Z.; Tang, H. L.; Pan, M. *Electrochim. Acta* **2006**, *51*, 5721–5730.

(34) Tian, Z. Q.; Jiang, S. P. ; Liu, Z. ; Li, L. *Electrochemistry Communications* **2007**, *9*, 1613–1618.

(35) Taylor, A. D.; Michel, M.; Sekol, R. C.; Kizuka, J. M.; Kotov, N. A.; Thompson, L. T. *Adv. Funct. Mater.* **2008**, *18*, 3003–3009.

(36) Litster, S.; McLean, G.. *J. Power Sources* **2004**, *130*, 61–76.

(37) Qi, Z.; Lefebvre, M. C.; Pickup, P. G.. *J. Electroanal. Chem.* **1998**, *459*, 9–14.

(38) Gratiet, B. L.; Remita, H.; Picq, G.; Delcourt, M. O. *Journal of Catalysis* **1996**, *164***,** 36–43.

(39) Xiang, X. -D. *Annu. Rev. Mater. Sci.***1999**, *29*, 149–171.

(40) Rajan, K. *Annu. Rev. Mater. Res.* **2008**, *38*, 299–322.

(41) Zhao, J-C. *Progress in Materials Science* **2006**, *51*, 557–631.

(42) Reddington, E.; Sapienza, A.; Gurau, B.; Viswanathan, R.; Sarangapani, S.; Smotkin, E. S.; Mallouk, T. E. *Science* **1998**, *280*, 1735-1737.

(43) Jayaraman, S.; Hillier, A. C. *J. Comb. Chem.* **2004,** *6,* 27-31.

(44) Jayaraman, S; Hillier, A. C. *Meas. Sci. Technol.* **2005**, *16***,** 5–13.

(45) Sehayek, T.; Bendikov, T.; Vaskevich, A.; Rubinstein, I. *Adv. Funct. Mater.* **2006**, *16*, 693–698.

(46) Ramakrishnan, S.; Shannon, C. *Langmuir* **2010**, *26*, 4602–4606.

(47) Mavré, F. *Anal. Chem.* **2010,** *82,* 8766–8774.

(48) Bard, A. J.; Faulkner, L. R. *Electrochemical Methods Fundamentals and Applications*, 2nd Ed. John Wiley & Sons, Inc.

(49) Goodridge, F.; King, C. J. H.; Wright, A. R. *Electrochimica Acta.* **1977**, *22*, 347-352.

(50) Arora, A.; Eijkel, J. C. T.; Morf, W. E.; Manz, A. *Anal. Chem.* **2001,** *73*, 3282-3288.

(51) Zhan, W.; Alvarez, J.; Crooks, R. M. *J. Am. Chem. Soc.* **2002**, *124*, 13265-13270.

(52) Bradley, J.-C.; Chen, H. –M.; Crawford, J.; Eckert, J.; Ernazarova, K.; Kurzeja, T.; Lin, M.; McGee, M.; Nadler, W.; Stephens, S. G. *Nature*, **1997**, *389*, 268-271.

(53) Warakulwit, C. ; Nguyen, T. ; Majimel, J. ; Delville, M. –H. ; Lapeyre, V. ; Garrigue, P. ; Ravaine, V. ; Limtrakul, J. ; Kuhn, A. *Nano Lett.* **2008**, *8*, 500-504.

(54) Ulrich, C.; Andersson, O.; Nyholm, L.; Björefors, F. *Angew. Chem. Int. Ed.* **2008**, *47*, 3034 –3036.

Chapter 2

Development of a bimetallic catalyst consisting of PtNP and Co-substituted polyoxometalate for proton exchange membrane fuel cell cathode

2.1 Introduction:

The continuous efforts to reduce the cost of Proton Exchange membrane fuel cell (PEMFC) has significantly reduced the Pt loading in membrane electrode assembly(MEA) since late 1990s. The currently achieved Pt-specific power density is 0.85-1.1 g_{Pt}/kW.[1] In order to commercialize the PEMFC for large scale automotive applications, the Power density is targeted to be < 0.2 g_{Pt}/kW at cell voltage of $\geq$ 0.65 V.[1] The main barrier to reach this target is the sluggish kinetics of cathodic oxygen reduction on the Pt catalyst in PEMFC. Application of Pt-alloy catalysts has the potential to overcome this barrier by improving the ORR kinetics and by reducing the Pt loading.[1]

The improved ORR kinetics on Pt-alloy surface over Pt surface has been explained based on two concepts: (i) the modified electronic and structural properties inhibiting the OH adsorption(from water decomposition) on the Pt-alloy surface[2,3] or (ii) combination of two complementary elements each enhancing the various steps in the ORR process: the base metal of the Pt-base metal alloy enhancing the O=O bond cleavage and the Pt enhancing the reduction of the cleaved 'O' atom to water.[4] The latter ORR mechanism proposed by Bard et al. on a bimetallic Pt-base metal alloy was further extended to a

catalyst system where the noble metal acts as the electrode and the base metal is placed in a metal co-ordinating inorganic system (polyoxometalates) by our research group.[5] Transition metal(TM)-substituted Dawson type phosphotungstates ($P_2W_{17}MO_{62}^{(12-n)-}$; $M=W^{VI}$, Fe^{II}, Co^{II}, Ru^{II}) and Keggin type phosphotungstates ($PW_{12}O_{40}^{3-}$ and $PCoW_{11}O_{39}^{5-}$) were studied as co-catalyst on bulk Au, Pd and Pt electrodes and significant positive shift in ORR $E_{1/2}$ potentials were obtained as per the thermodynamic guidelines suggested by Bard et al.[5]

In addition to the favorable properties such as proton conduction,[6,7] lattice oxygen atom transfer (labile lattice oxygen atom),[8,9] multi e- transfer,[10] hydrolytic stability at low pH (especially Dawson and Keggin type),[7,10] the oxidatively stable inorganic metal-oxygen frame work of POM[11] which acts as a skeleton for holding the base metal makes the polyoxometalate a suitable ORR catalyst for the fuel cell application as it helps to overcome the problem of base metal leaching at high positive potentials of the cathode during the fuel cell operation. Among several combinations of noble metal-TM-substituted POM catalyst systems, the best cathode performance was obtained with Pt-Co-Keggin (with +54 mV positive shift in $E_{1/2}$ compared with the bare Pt), next comes the Pt-Co-Dawson (+21 mV positive shift in the $E_{1/2}$ compared with the bare Pt).[5] Dawson type polyoxometalates have higher hydrolytic stability than the Keggin type POM[12] and hence PtNP were combined with Co-Dawson using the two synthetic approaches: Synthetic approach (i) was based on the metal nanoparticles directly stabilized by the polyoxometalates through the chemisorption.[13-15] (Co-Dawson-stabilized PtNP) To overcome certain drawbacks in this approach (i) (vide infra), synthetic approach (ii) was adopted which is based on the layer-by-layer(LBL) assembly[16] of thiol[17] or polymer[18]

stabilized metal nanoparticles and the polyoxometalates through the electrostatic interaction. (protonated cysteamine-stabilized PtNP or PDDA-stabilized PtNP[18,19] and assembling them with Co-Dawson using the layer-by-layer technique).

Layer-by-layer (LBL) assembly used in the synthetic approach (ii) is a versatile bottom-up nano fabrication technique giving opportunity to incorporate a variety of materials within a multilayer in a simple, inexpensive way.[16] The most common and simple strategy used in the LBL assembly is the electrostatic interaction between the positively and negatively charged species assembled in the subsequent layers as shown in Fig. 2.1.

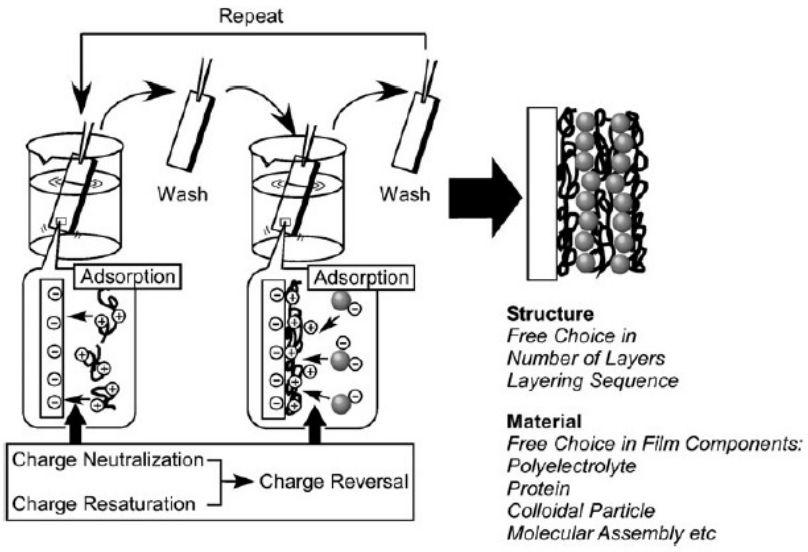

Fig. 2.1 Outline of LBL assembly by the electrostatic interaction.
(reprinted from Ref. 16 with permission from RSC Publishing)

In this method, a charged substrate is alternately dipped in to solutions containing oppositely charged species with intermittent washing to remove the non-specifically

adsorbed species. Relatively high concentrations of the substances in the working solutions are adopted to adsorb the species excessively so that on each dip both charge neutralization and charge reversal by resaturation of the surface will occur as illustrated in Fig. 2.1. Charge reversal is essential for the subsequent layer growth. Alternate dip in to solutions containing oppositely charged species will lead to the continuous growth of the film consisting of positively and negatively charged species in alternate layers. Since, in LBL process, adsorption of discrete species from solution on to the substrate leads to the film formation, there is a flexibility of the substrate geometry as long as the surface is accessible to the working solution. The LBL assembly through the electrostatic interaction can be carried out on any type of material which is initially charged and there is a great flexibility in choosing the number of layers and the layering sequence. Protonated cysteamine-stabilized PtNP, PDDA-stabilized PtNP used in the synthetic approach (ii) are positively charged and Co-Dawson is negatively charged and these oppositely charged species were assembled by the electrostatic force during the layer-by-layer assembly.

The ORR kinetics on the prepared PtNP-Co-Dawson composite catalyst electrodes were determined by the Rotating Disc Electrode(RDE) experiment to prove our hypothesis that Co-center in Co-Dawson co-catalyses ORR on the Pt surface by enhancing the O=O bond cleavage and compared the ORR performance on this nano-composite system with the commercial Pt/C.

2.2 Experimental details:

2.2.1 Synthesis of POM-stabilized PtNP:

19.2 ml of hexachloroplatinic acid (8 wt% in H_2O) & 38.8 mg of POM were dissolved in 19.564 ml millipore H_2O and the solution is stirred for 30 min. 416.7 ml of

96 mM $NaBH_4$ was added dropwise. The above reaction mixture was stirred for 30 min. Finally, a brownish black suspension of PtNP was obtained. The molar ratio of Pt : POM : $NaBH_4$ is 1:2:10. The corresponding concentrations used are 0.2 mM, 0.4 mM & 2 mM respectively.

2.2.2 Synthesis of cysteamine-stabilized PtNP:

28.8 µl aqueous hexachloroplatinic acid (8 wt % in H_2O) and 500 µl of 12 mM cysteamine hydrochloride (2-aminoethanethiol hydrochloride) were added to 28.871 ml of Millipore H_2O with stirring. Stirring was continued for another 30 minutes to allow the co-ordination of cysteamine to Pt precursor. Then 600 µl of 0.1 M aqueous $NaBH_4$ was added dropwise to reduce Pt^{IV} to Pt^0. The appearance of a brownish black suspension indicated the formation of PtNP. The reaction mixture was stirred for another 15 min to get the complete reduction of Pt^{IV}. The molar ratio of Pt:cysteamine:$NaBH_4$ is 1:1:10. The concentrations used are 0.2 mM, 0.2 mM and 2.0 mM respectively.

2.2.3 Synthesis of PDDA-stabilized PtNP:

288 µl aqueous hexachloroplatinic acid (8 wt % in H_2O) was added to 25.632 ml of Millipore H_2O. 84 µl aqueous PDDA (MW 5000 to 20,000, 35 wt% in H_2O) was added to the above mentioned solution and stirred for 20 min for thorough mixing of $[PtCl_6]^{2-}$ and PDDA polymer. 3.996 ml of 0.1 M aq. $NaBH_4$ was added dropwise to reduce Pt^{IV} to Pt^0. A brownish black PtNP suspension was obtained. The reaction mixture was stirred for another 15 min to get the complete reduction of Pt^{IV}. The molar ratio of Pt:PDDA:$NaBH_4$ is 1:3:6.7. The concentrations used are 2 mM, 6 mM and 13.32 mM respectively.

2.2.4 Electrocatalyst or electrode preparation for loading POM-surrounded PtNP:

Glassy carbon (GC) or electrocatalyst loaded GC electrode was used as the working

electrode (WE), Pt mesh as the counter electrode (CE) and Ag/AgCl(sat) as the reference electrode (RE). All potentials given in this chapter are referred against Ag/AgCl(sat). GC was polished with 15 μm, 3 μm, 1 μm diamond suspensions. Next the residual organic impurities, if any, on GC surface was removed by applying a constant of +1250 mV in 1 M NaOH. Next the GC electrode was cycled between -1000 mV & +1500 mV in 0.5 M H_2SO_4. POM-stabilized PtNP was centrifuged to remove the excess POM & then 20 μl of concentrated POM-Stabilized PtNP (concentration of 1.644 mM) dispersed in 0.02% Nafion was drop coated on treated GC (0.28 cm^2 RDE). The drop was left to dry overnight, before carrying out the electrochemical experiments.

2.2.5 Electrode preparation for LBL assembly of cysteamine-PtNP or PDDA-PtNP with POM:

GC electrodes were polished sequentially with 15 μm, 3 μm, 1 μm polycrystalline diamond suspensions (Metadi supreme, Buehler) and finally with 0.05 μm Alumina (Buehler). For electrochemical cleaning, GC was made as WE, Pt mesh as CE and Ag/AgCl(sat) as RE. After mechanical polishing, electrochemical treatments were given by cycling the GC potential between -1000 mV and +1500 mV at a scan rate of 100 mV/sec in 0.5 M H_2SO_4 and then by applying an oxidation potential of +1250 mV for 5 min in 1 M NaOH. This alkali treatment not only oxidizes the organic impurities present on the GC surface, but also oxidizes the GC surface carbon atoms to carboxylate groups ($-COO^-$). The pH was maintained at least 5 or above throughout the LBL process to keep these carboxylic groups deprotonated to facilitate the electrostatic adsorption of the cysteamine- or PDDA-stabilized PtNP (positively charged) on the GC surface, when the treated GC is kept immersed in these PtNP colloidal solutions for 3hrs. (pH was 5 in the

case of cysteamine-PtNP to maintain the protonated state of the cysteamine and 6 in the case of PDDA-PtNP considering the instability of the POMs in the neutral and alkaline pH)

After the first positively charged cysteamine- or PDDA-PtNP layer formation, the electrode was washed with solvent to remove the non-specific interaction of cysteamine- or PDDA-PtNP with the GC electrode. Then the electrode was dried using Ar gas. Next the electrode was dipped for 30 min in 0.2 mM POM solution in $HClO_4$. Then the electrode was washed with the solvent and dried using Ar gas. Cycles of cysteamine- or PDDA-PtNP and POM dipping were continued until the desired number of bilayers was obtained. 30 min dipping time was maintained for each dip in cysteamine- or PDDA-PtNP suspension or in POM solution except the initial dip in cysteamine- or PDDA- PtNP suspension for 3 hr.

2.2.6 ORR kinetics using rotating disc electrode (RDE) experiment:

In the case of POM-stabilized PtNP, drop coated RDE GC electrode will be used as WE, Pt mesh as CE and Ag/AgCl(sat) as RE. 0.1 M $HClO_4$ as supporting electrolyte. Linear sweep voltammetry (LSV) was carried out from 800 mV to 0 mV at a scan rate of 10 mV/Sec in O_2 saturated 0.1 M $HClO_4$ at various electrode rotation speed . For background currents were obtained in Ar purged 0.1 M $HClO_4$.

In the case of cysteamine- or PDDA-PtNP/POM LBL assembly, for optimizing the number of bilayers, the required number of bilayers were grown on identical GC electrodes (0.07 cm^2) and O_2 reduction was carried out in O_2 saturated 0.1 M $HClO_4$ by sweeping the WE (cysteamine- or PDDA-PtNP/Co-Daw LBL assembly on GC) potential from 800 mV to 0 mV at a scan rate of 10 mV/sec. For Kinetic studies, optimized number

of bilayers of cysteamine- or PDDA– PtNP/POM (Dawson or Co-Dawson) were grown on GC RDE (area 0.283cm^2) and similar experiments were conducted as given for POM-stabilized PtNP.

2.2.7 CO strip voltammetry:

WE, CE and RE used are the same used in the ORR experiment. Working electrode potential was held at 90 mV using controlled potential electrolysis (CPE) and CO was dosed in 0.1 M $HClO_4$ electrolyte for 90 min. Then the dissolved CO was removed by purging the electrolyte with Ar for 30 min while continuing the potential holding of WE at 90 mV. Then, CO stripping was carried out at once, by sweeping the working electrode potential from 90 mV to 800 mV at a scan rate of 10 mV/sec

2.2.8 UV–Vis Measurements:

A Shimadzu UV-3600 UV–vis-near infrared (UV–vis-NIR) spectrophotometer was used for collecting UV-Vis spectra.

2.2.9 Transmission electron microscope (TEM):

Samples of PtNP suspension were dried on forwar & carbon coated Cu 300 mesh grids for TEM measurements. TEM measurements were done using a Zeiss EM10 transmission electron microscope (Carl Zeiss SMT, Inc, Germany) operated at an accelerating voltage of 60 kV.

2.2.10 Scanning electron microscope (SEM)/ Energy dispersive X-ray spectroscopy (EDX):

For POM-stabilized PtNP the concentrated PtNP suspension was drop coated on a carbon tape. For PDDA-PtNP/POM LBL assembly, 10 bilayers were grown on a glassy carbon for SEM and EDX. SEM images were collected using a JEOL JSM-7000F field-emission scanning electron microscope and analyzed using the EOS 7000F software

package. EDX data were acquired using an Oxford X-Max energy dispersive X-ray spectrometer and were analyzed using the INCA software package.

2.3 Results and discussions:

2.3.1 Characterization of POM-PtNP:

The preparation of POM-surrounded PtNP were confirmed by UV-Vis measurement and TEM. Fig. 2.2a and 2.3a shows the UV-Vis spectra of Co-Dawson-stabilized PtNP (Co-Daw-PtNP) and Dawson-stabilized PtNP (Daw-PtNP) respectively. The LSPR maximum in the UV region around 215 nm is the characteristic of colloidal PtNP solution. The average particle size calculated from TEM image is 5±1 nm for both Co-Daw-PtNP (Fig. 2.2b) and Daw-PtNP (Fig. 2.3b). The SEM images in Fig. 2.2c and 2.3c shows that the nano structure of the POM surrounded PtNP is maintained in the film cast from these colloidal solutions. The EDX results confirm the presence of POM by elemental analysis as given in Fig. 2.2d and 2.3d.

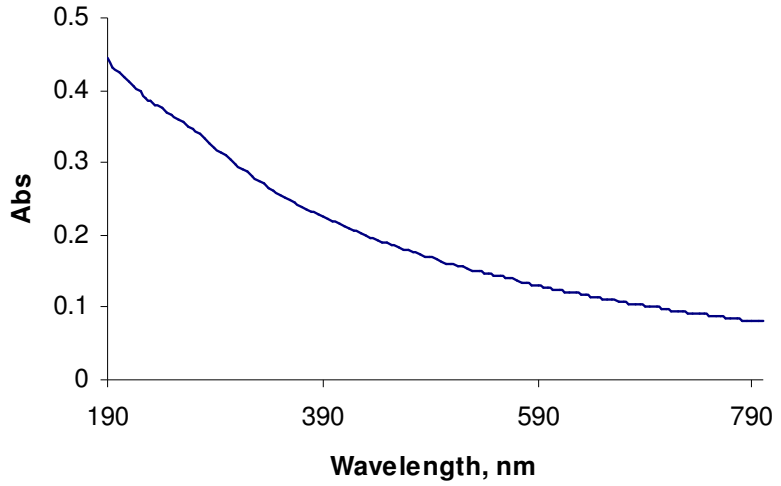

Fig. 2.2a UV-Vis spectrum of Co-Daw-PtNP

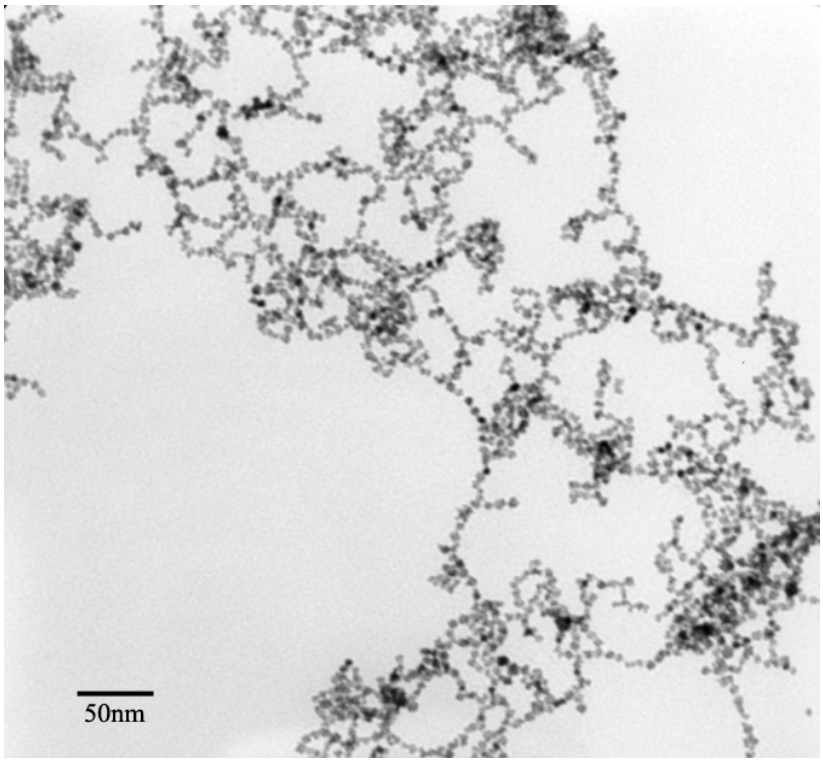

Fig. 2.2b TEM image of Co-Daw-PtNP

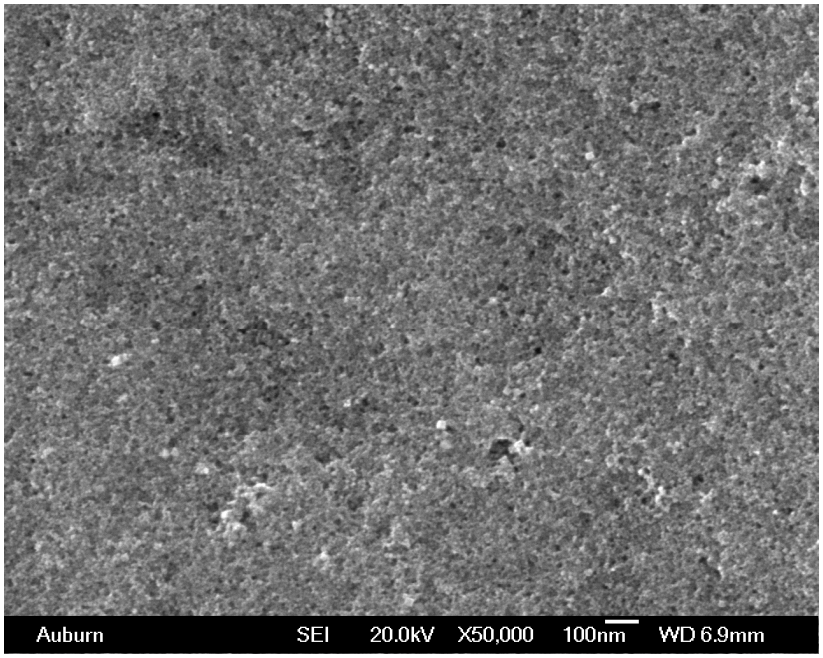

Fig. 2.2c SEM image of Co-Daw-PtNP

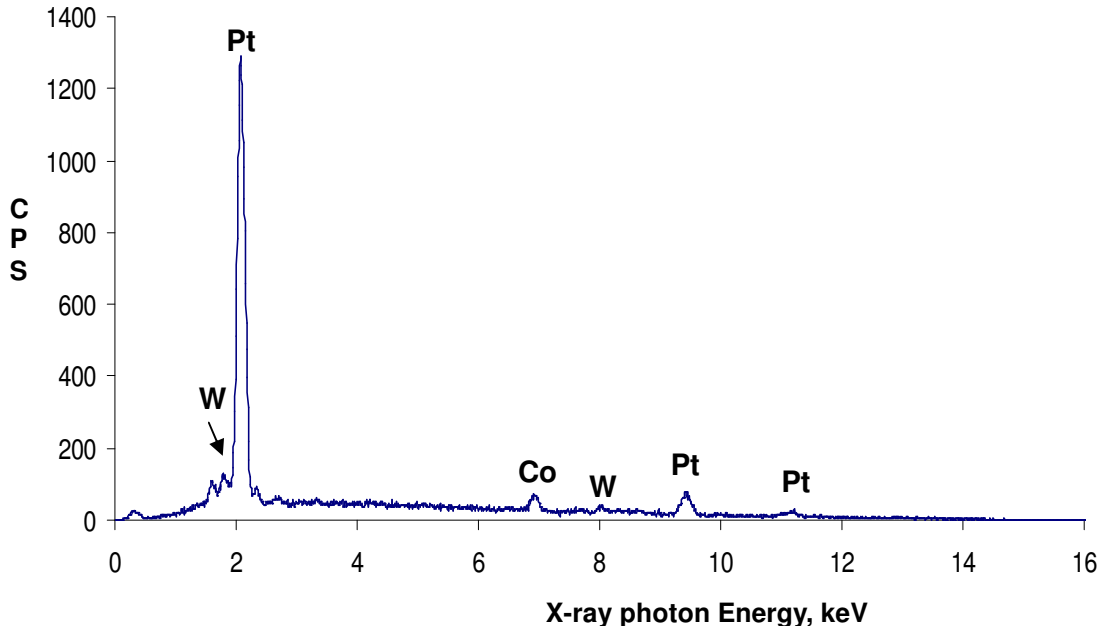

Fig. 2.2d EDX analysis of Co-Daw-PtNP

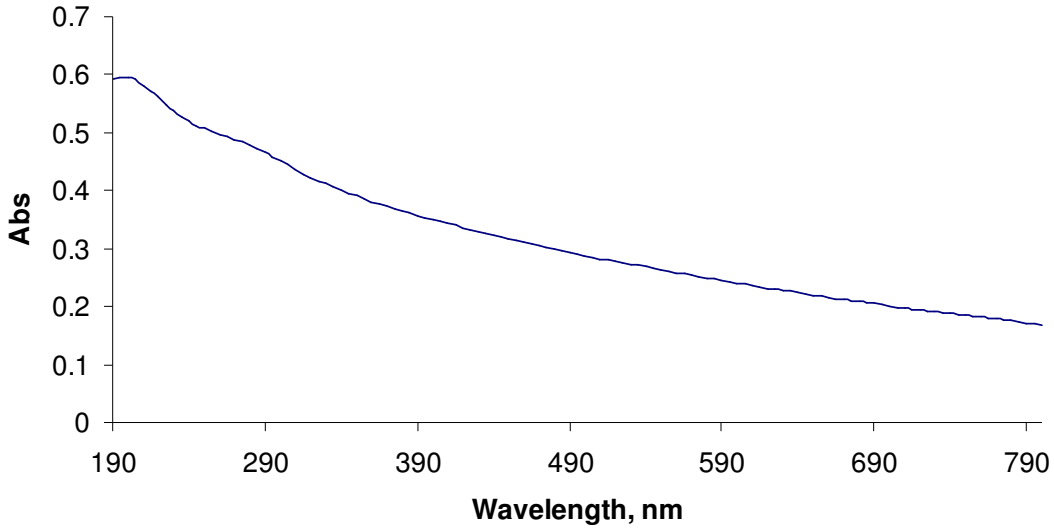

Fig. 2.3a UV-Vis spectrum of Daw-PtNP

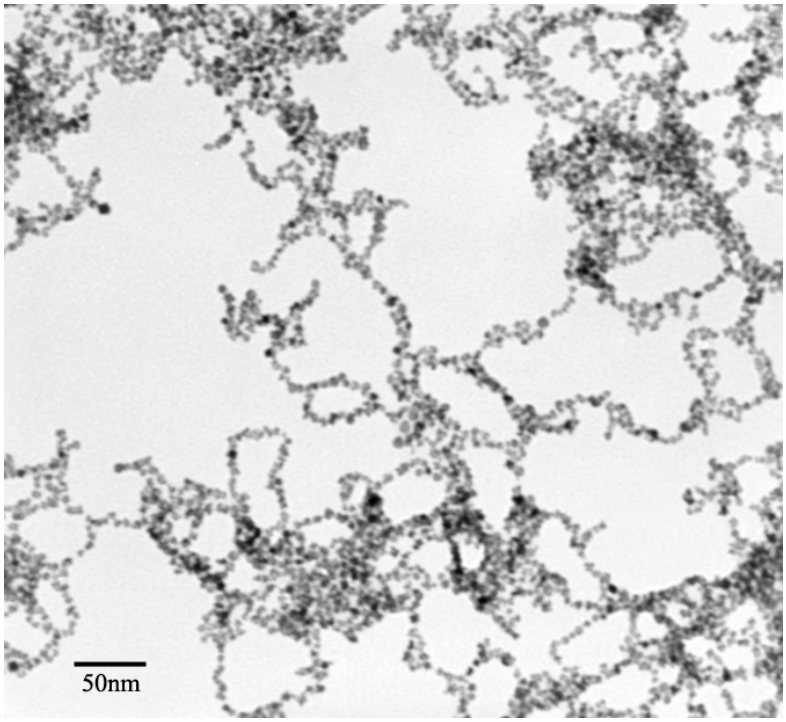

Fig. 2.3b TEM image of Daw-PtNP

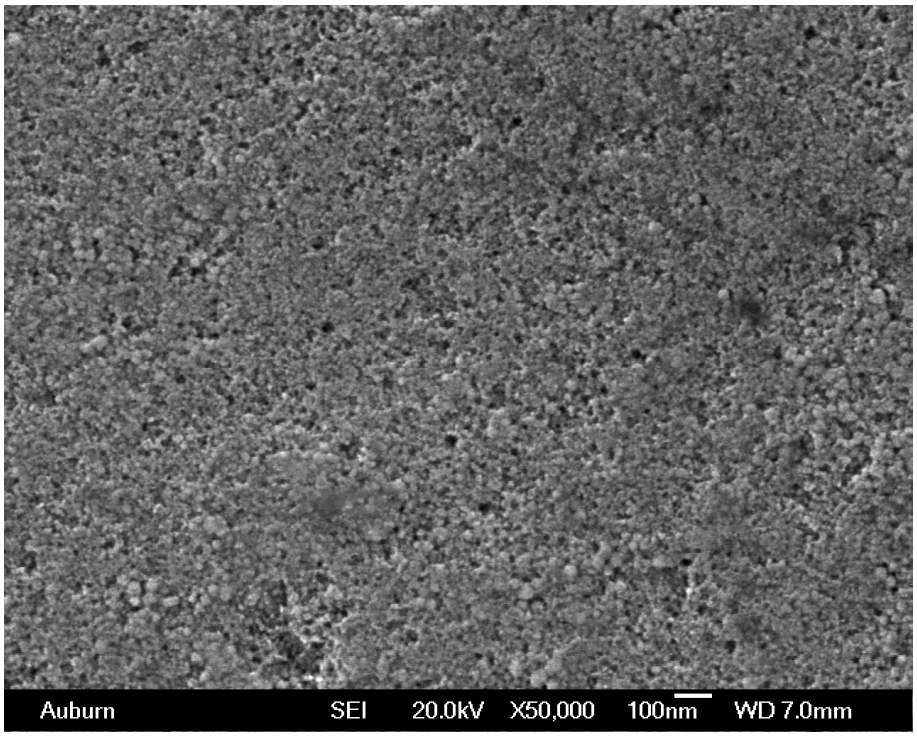

Fig. 2.3c SEM image of Daw-PtNP

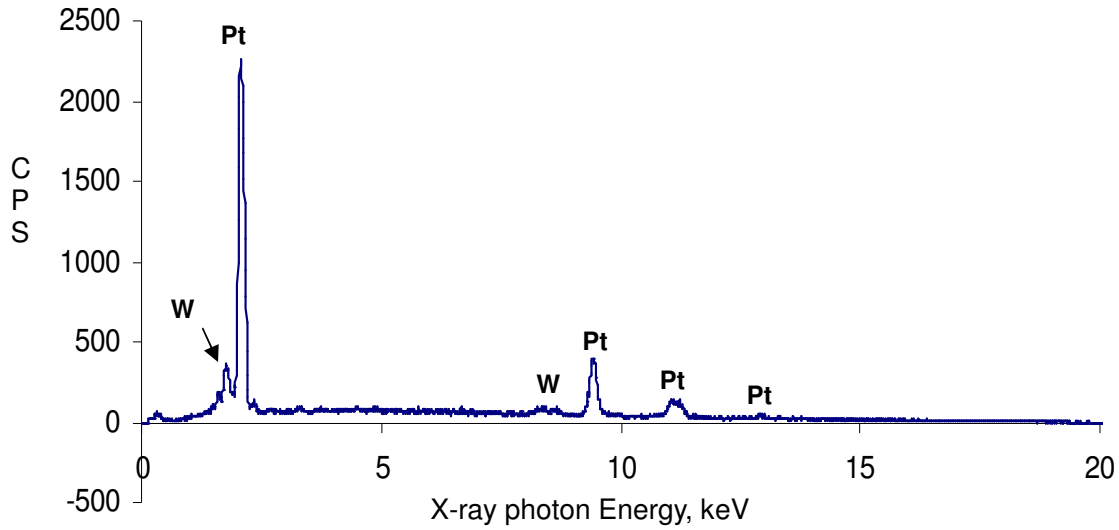

Fig. 2.3d EDX analysis of Daw-PtNP

2.3.2 Characterization of cysteamine-stabilized PtNP:

The formation of cysteamine-stabilized PtNP was confirmed by the UV-Vis spectrum (Fig. 2.4a) and TEM measurements (Fig. 2.4b). Using the TEM measurements the average particle size is calculated to be 2±1 nm with some aggregates of size 15±5 nm.

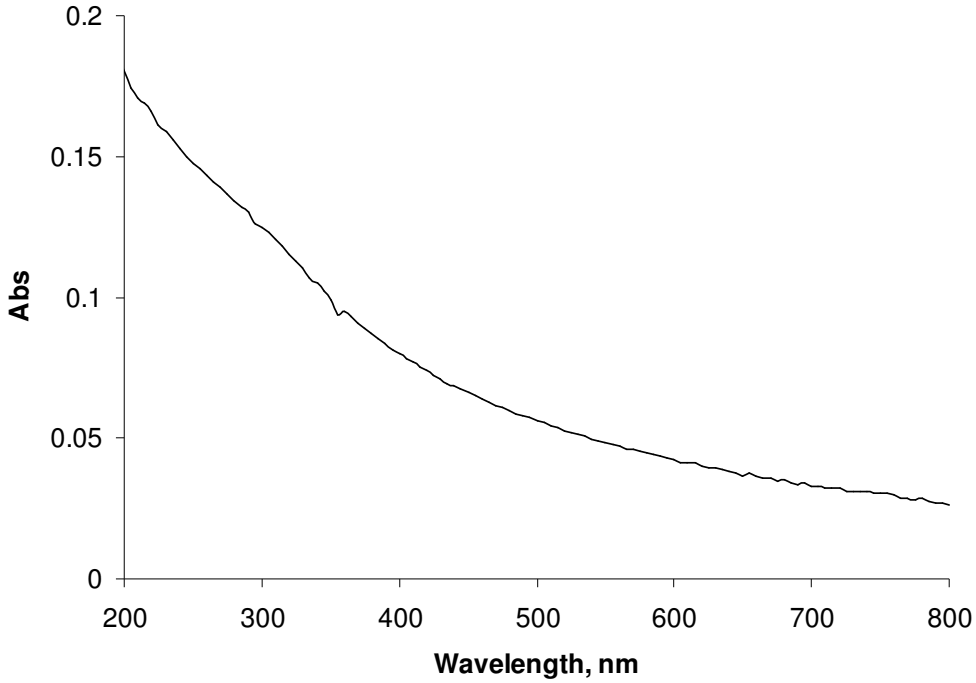

Fig. 2.4a UV-Vis spectrum of cysteamine-PtNP

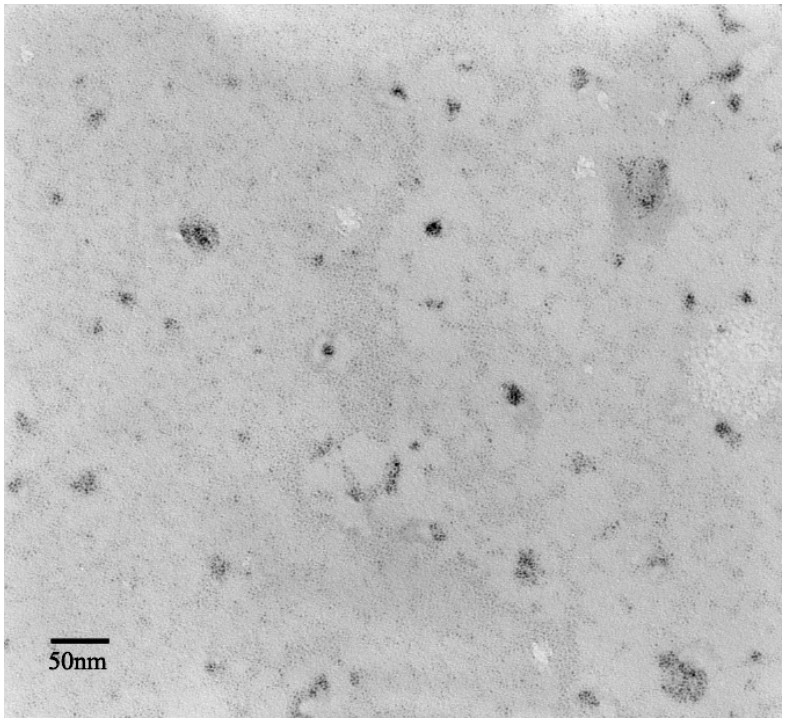

Fig. 2.4b TEM image of cysteamine-PtNP

2.3.3 Characterization of PDDA-PtNP/POM LBL Assembly:

UV-Vis spectrum (Fig. 2.5) and TEM (Fig. 2.6) confirm the formation of PDDA-stabilized PtNP formation. The average particle size is 6±3 nm as measured from TEM image. Fig 2.7 and 2.8 show the SEM images of Co-Dawson and Dawson LBL assembly (10 bilayers) with PDDA-PtNP (PDDA-PtNP/Co-Daw and PDDA-PtNP/Daw) respectively. The particles look agglomerated with 12±7 nm size containing smaller particles. The coverage of particles is greater in Dawson than Co-Dawson LBL assembly with PDDA-PtNP. A noticeable feature is that the substrate is exposed in both cases and the Pt loading is considerably less.

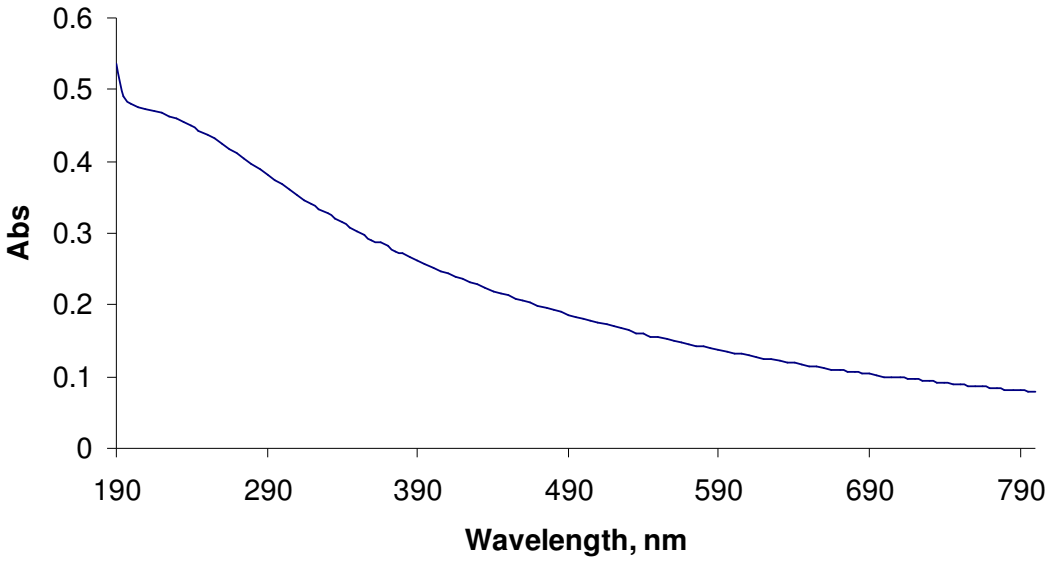

Fig. 2.5 UV-Vis spectra of PDDA-PtNP

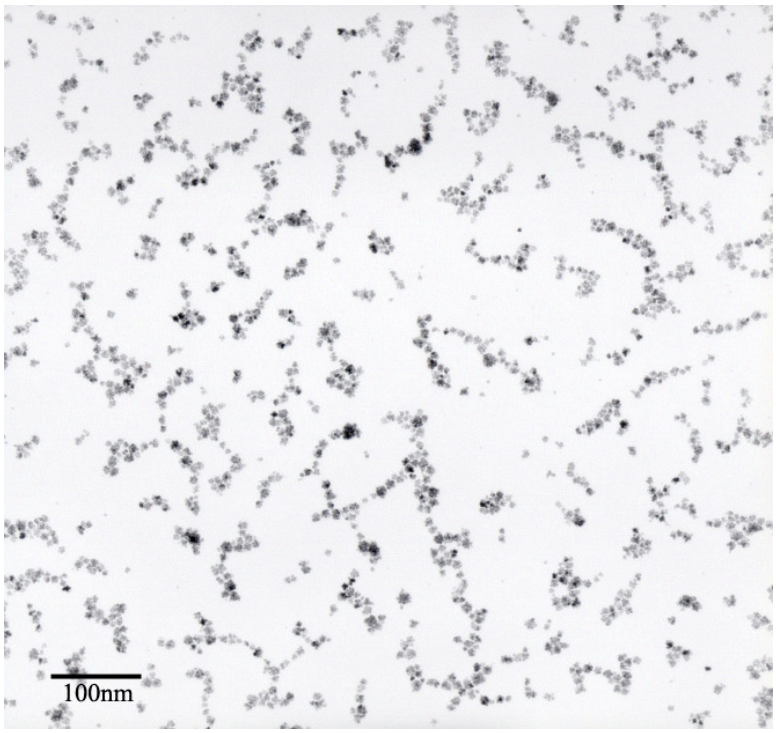

Fig. 2.6 TEM image of PDDA-PtNP

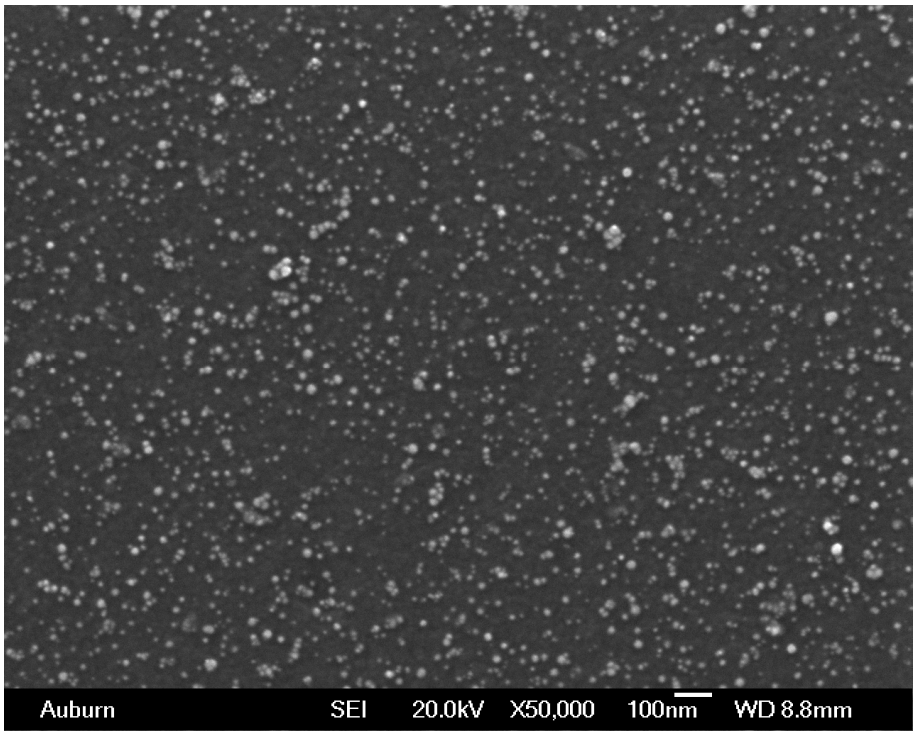

Fig. 2.7 SEM image of PDDA-PtNP/Co-Daw 10 bilayers

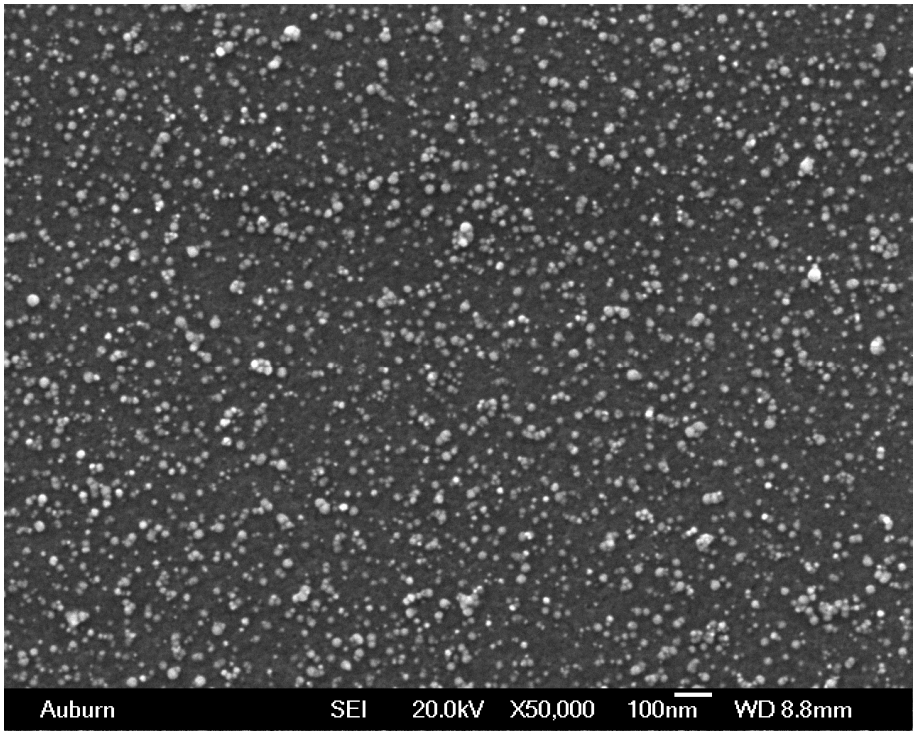

Fig. 2.8 SEM image of PDDA-PtNP/Daw 10 bilayers

2.3.4 ORR on POM-surrounded PtNP:

Fig. 2.9 compares the ORR voltammetric(cathodic) scans at 0 rpm obtained on Dawson-surrounded PtNP (Daw-PtNP) and Co-Dawson-surrounded PtNP (Co-Daw-PtNP) supported on glassy carbon (GC) electrode. Co-Daw-PtNP with a half-wave potential of 575mV, showed a positive shift of 35 mV when compared with Daw-PtNP with a half-wave potential of 540 mV. 35 mV positive shift indicates that the Co-Dawson acts as a better co-catalyst than Dawson for ORR on Pt surface.

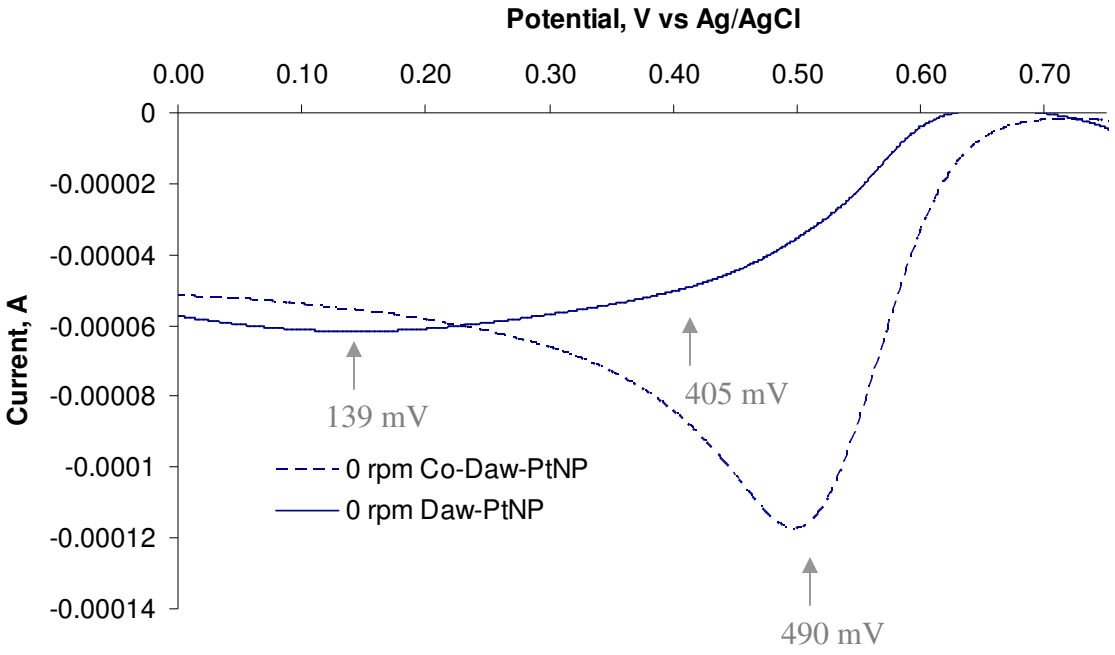

Fig. 2.9 Overlay of the ORR voltammetric scans of Co-Daw-PtNP and Daw-PtNP

A noticeable feature in the ORR voltammetric scan obtained on Daw-PtNP /GC (shown in Fig. 2.9) with two peaks, one at 405 mV and another at 139mV, indicates that on Daw-PtNP /GC, ORR may occur in two steps through hydrogen peroxide pathway. The ORR is expected to follow the direct four electron reduction mechanism with a single reduction peak(490 mV) on Co-Daw-PtNP/GC, which is clear from n = 4 indicated in Table 2.1 representing the kinetic parameters obtained from the K-L plot (Fig. 2.10b) corresponding to the ORR voltammetric scans (Fig. 2.10a) obtained on Co-Daw-PtNP /GC. The ORR kinetic current is extracted from the measured ORR current by a graphical method in the Koutecky-Levich (K-L) plot analysis on a Rotating disc electrode. The measured ORR current can be expressed as a function of kinetic current, i_k and diffusion current, i_d as follows:[20]

$$1/i=(1/i_k+1/i_d) = f(\omega^{-1/2})E \quad (2.1)$$

For a given potential 'E', i^{-1} is a linear function of $\omega^{-1/2}$, where ω is the angular velocity of the rotating disc electrode in radian/sec. As per Levich equation the diffusion limited current i_d is given as

$$i_d = 0.62nFAD_O^{2/3}C_O^b\nu^{-1/6}\omega^{1/2}$$

where n is the number of electron transferred in the ORR mechanism, F is Faraday's constant, A is the electrode area, D_O is the diffusion co-efficient of O_2 in the electrolyte solution, C_O^b is the bulk concentration of dissolved O_2 in the electrolyte solution, ν is the kinematic viscosity of the solution.

So,

$$1/i = 1/i_k + 1/ (0.62nFAD_O^{2/3}C_O^b\nu^{-1/6}\omega^{1/2})$$

On plotting i^{-1} vs $\omega^{-1/2}$, the y-intercept gives i_k^{-1} and from the slope 'n' can be found. 'n' was calculated from K-L plot slope with $D_O= 2.0x10^{-5}$ cm^2/s, $C_O^b = 1.2x10^{-6}$ mol/cm^3, $\nu = 1.0x10^{-2}cm^2/s$,[20] $A=0.283cm^2$, $w = 2\Pi f$, f = electrode rotation speed in rotations per second.

Table 2.2 represents the kinetic parameters obtained from the K-L plots (Fig. 2.11b) derived from the ORR voltammetric scans (Fig. 2.11a) on Daw-PtNP /GC with n = 1.4 to 2.2 indicates that ORR follows a 1 or 2 e^- reduction mechanism to form superoxide or peroxide respectively on Daw-PtNP.

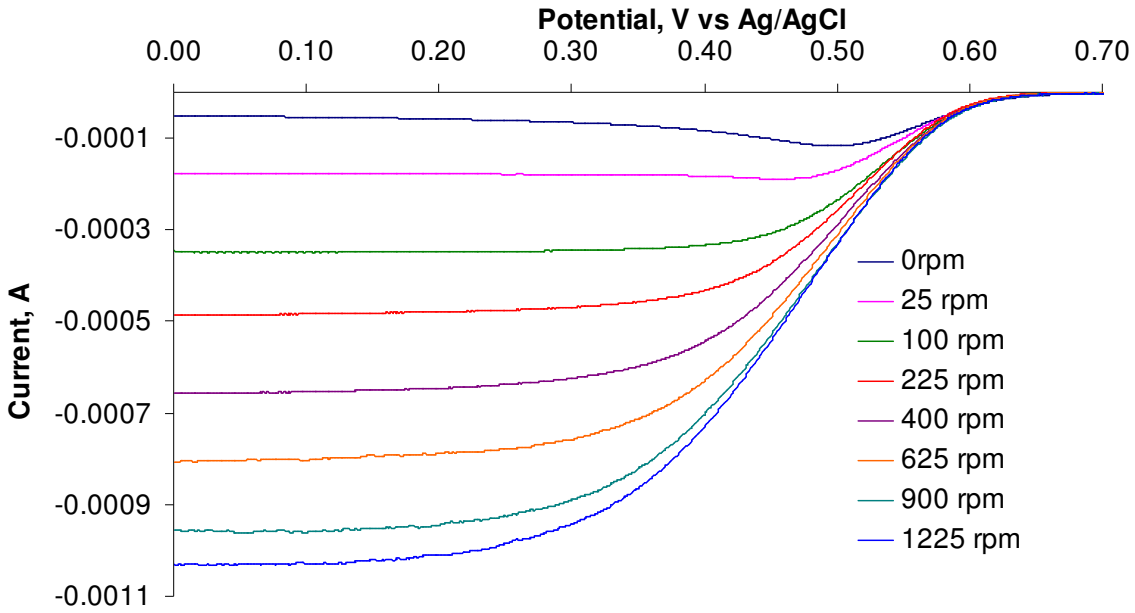

Fig 2.10a ORR voltammetric scans (cathodic) of Co-Daw-PtNP

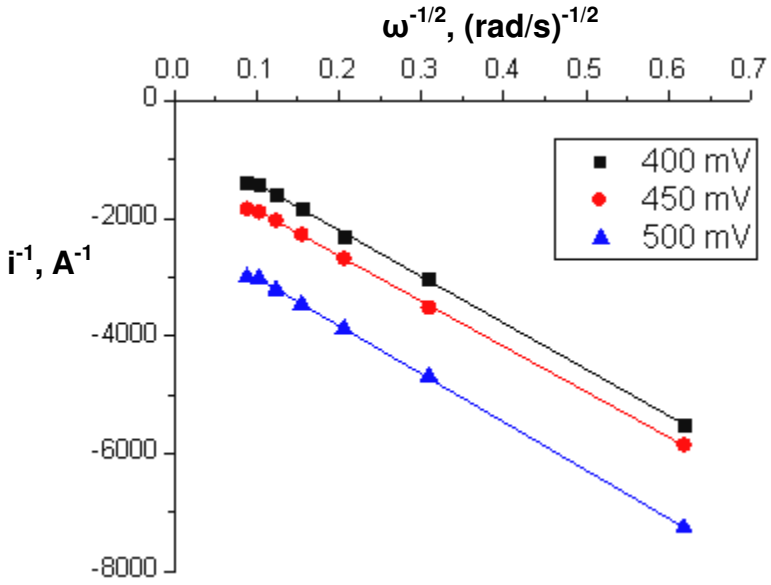

Fig. 2.10b K-L plot analysis of ORR on Co-Daw-PtNP.

Note: The data point at high electrode rotation speed (above 900 rpm) did not fit the linear model represented by K-L equation (Equation 2.1) due to the kinetic limitation for ORR caused by the blocking of Pt active sites due to chemisorption of Co-Dawson.

Table 2.1 Kinetic parameters associated with Fig. 2.10b

Potential, mV	n	i_k, mA	Specific activity, mA/cm^2_{Pt}
500	3.8	0.456	0.326
450	4.0	0.915	0.654
400	3.9	1.60	1.14

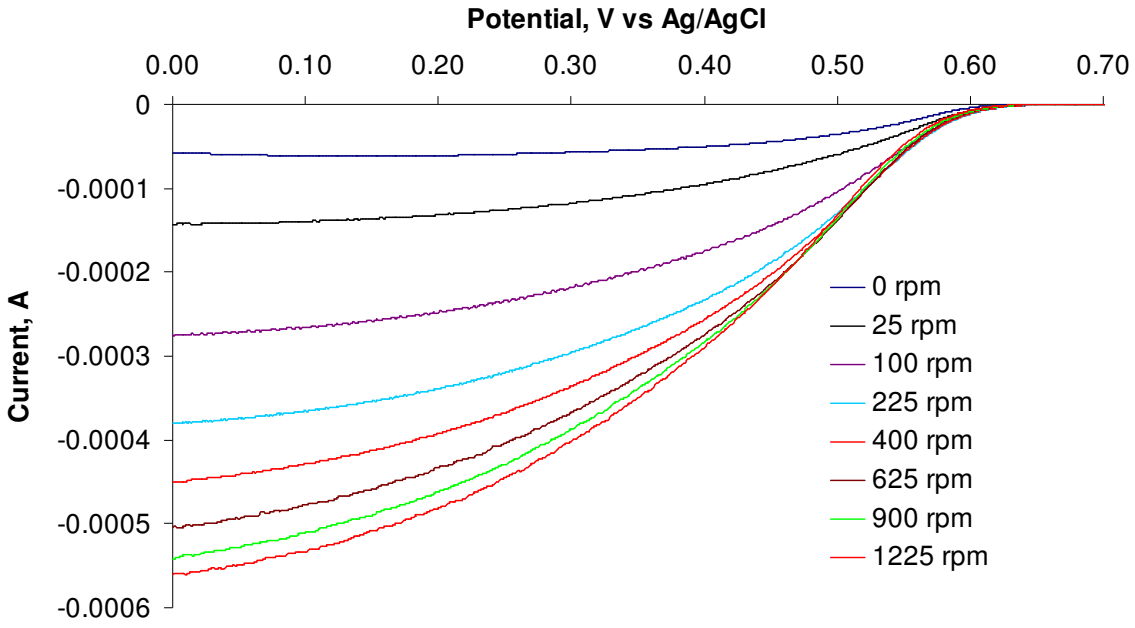

Fig. 2.11a ORR voltammetric scans (cathodic) of Daw-PtNP

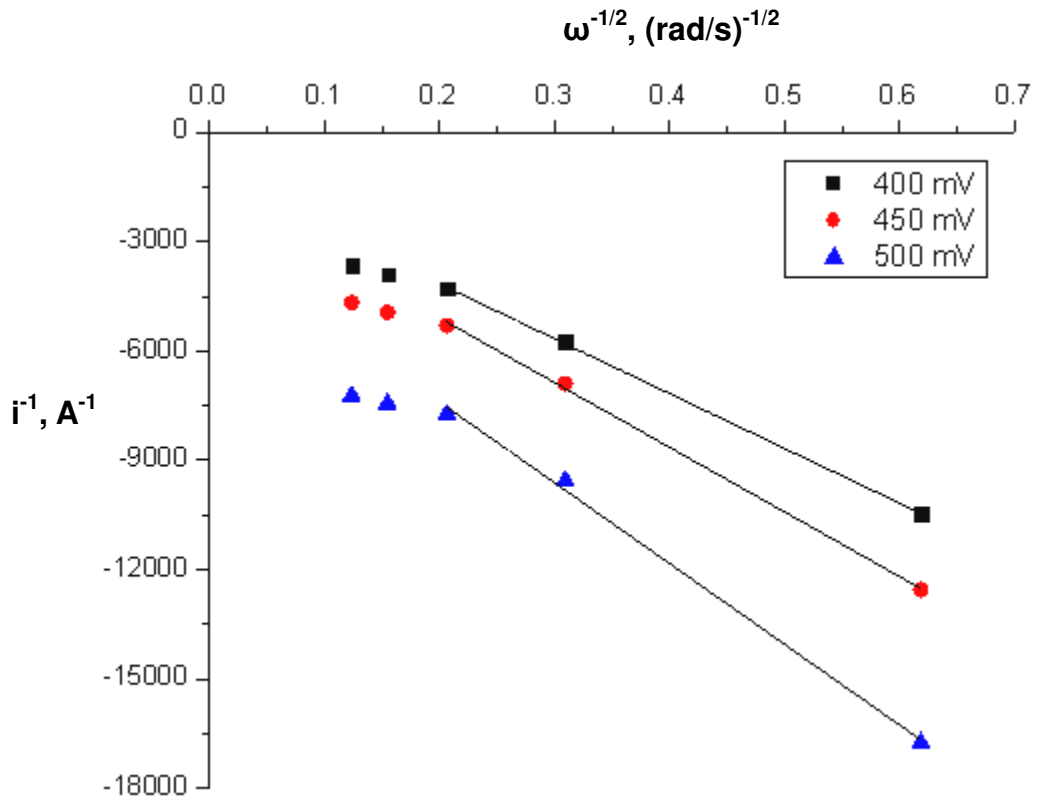

Fig. 2.11b K-L plot analysis of ORR on Daw-PtNP.

Note: The data points at high electrode rotation speed (above 225 rpm) did not fit the linear model represented by K-L equation (Equation 2.1) due to the kinetic limitation for ORR caused by the blocking of Pt active sites due to chemisorption of Dawson.

Table 2.2 Kinetic parameters associated with Fig. 2.11b

Potential, mV	**n**	**i_k, mA**
500	1.4	0.337
450	1.7	0.649
400	2.2	0.874

The kinetic current and the number of electron transferred per oxygen molecule for the ORR were calculated in the potential range where the current is within 10-80% of the diffusion limited current.[21]

Generally accepted ORR mechanism on naked Pt surface is $4e^-$ reduction which involves the O=O bond cleavage under the same experimental condition (0.1M $HClO_4$, acidic electrolyte containing the non-adsorbing anion)[3]

ORR following a 1 or 2 e^- reduction mechanism in Dawson-surrounded PtNP indicates that there is a possibility for the shortage of dual sites (required for the O=O bond cleavage on Pt surface) due to the chemisorption of Dawson.[22] Analogous to the strong adsorption of halide (eg. Cl^-, Br^-) on Pt(100) facet, causing the shortage of dual sites, which is evident from the enhanced H_2O_2 formation detected by the rotating ring disc electrode experiment,[22] we expect Dawson getting adsorbed on Pt active sites should be reducing the availability of dual sites leading to 1 or $2e^-$ reduction mechanism for the ORR.

Finke et al. have given a detailed account on the geometric factors influencing the adsorption of a tridentate, C_3 symmetry oxoanion including Dawson type POM on a metal surface which qualify them as a good stabilizing agent for the transition metal nanoclusters.[13] According to these authors, similar to the SO_4^{2-} adsorption on a metal(111) facet, the tridendate,C_3 symmetry oxoanions like Dawson and Keggin type polyoxometalates (e.g. $P_2W_{15}Nb_3O_{62}^{9-}$, $SiW_9Nb_3O_{40}^{7-}$) and citrate ($C_6H_5O_7^{3-}$) bind to the (111) facet of a transition metal surface. The lattice size matching between the interatomic distance of the facially oriented oxygen atoms and the interatomic distance of

the surface atoms on a metal(111) facet determines the binding strength of an oxoanion on a metal surface. Dawson type tri-Nb substituted phosphotungstate acted as a good stabilizer to form the Ir nanocluster, as the facially oriented oxygen atoms of this POM, $P_2W_{15}Nb_{13}O_{62}^{9-}$ had a good lattice size matching with the Ir surface atoms [size-matching ratio(O-O)/(Ir-Ir) = 2.85A/2.72A= 1.05].

We interpret that Dawson preferentially chemisorbs on Pt(111), as we expect Dawson to have good lattice size matching with the surface Pt atoms as Dawson is structurally similar to the Dawson type tri-Nb substituted phosphotungstate used by these authors and Pt, Ir have closer interatomic distance(Pt - 2.78 Å and Ir – 2.72 Å). An additional literature support reveals that POM like Keggin type silicotungstate, α-$SiW_{12}O_{40}^{4-}$, has been proven to adsorb on Ag(111) facet as a close packed self asembly.[23]

Fig. 2.12a and 2.12b show the CO strip voltammograms obtained on Co-Daw-PtNP and Daw-PtNP respectively. Deconvolution of these voltammograms resulted in two CO strip peaks which are considered to emerge from two energetically different sites on Pt surface, one at a less positive potential associated with (111) facet of PtNP and the other at a more positive potential associated with (100) facet of PtNP surface.[24] Fig. 2.12c is the overlay of deconvoluted CO strip peaks obtained on Co-Daw-PtNP and Daw-PtNP. It is clear from Fig. 2.12c that the CO strip peaks associated with (111) and (100) facets of Co-Daw-PtNP and Daw-PtNP occur in the same potential region. The CO strip ECSA corresponding to (111) facet is less than that corresponding to (100) facet for both Co-Daw-PtNP and Daw-PtNP. The corresponding ECSA is listed in Table 2.3.

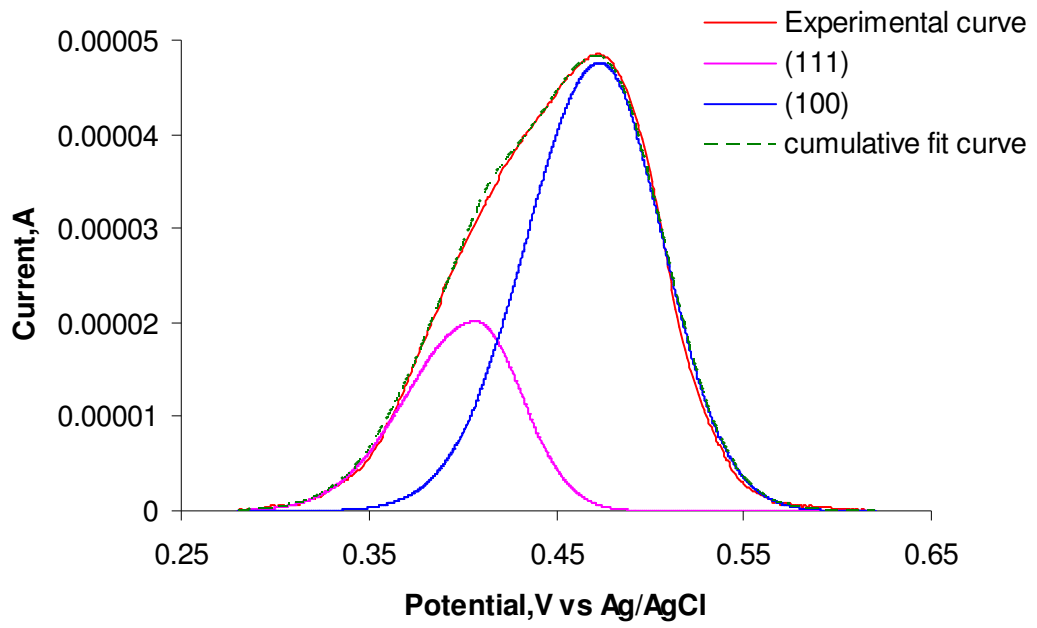

Fig. 2.12a CO strip voltammogram from Co-Daw-PtNP. The deconvolution of CO strip peak was performed using the BiGaussian function (OriginPro 8.6 32Bit).

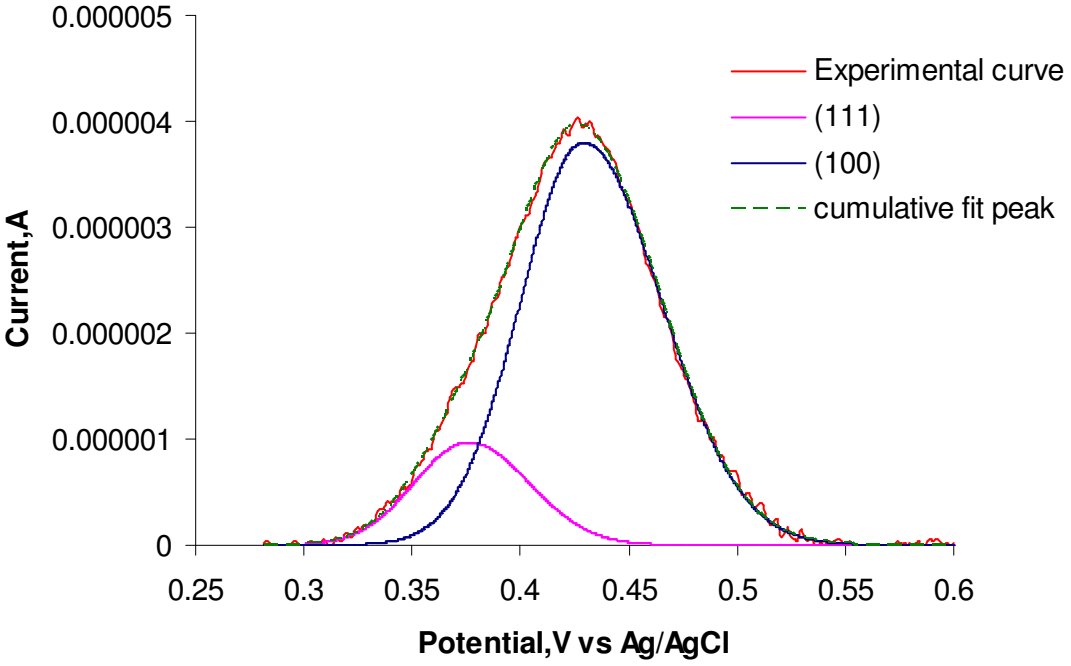

Fig. 2.12b CO strip voltammogram from Daw-PtNP. The deconvolution of CO strip peak was performed using the BiGaussian function (OriginPro 8.6 32Bit).

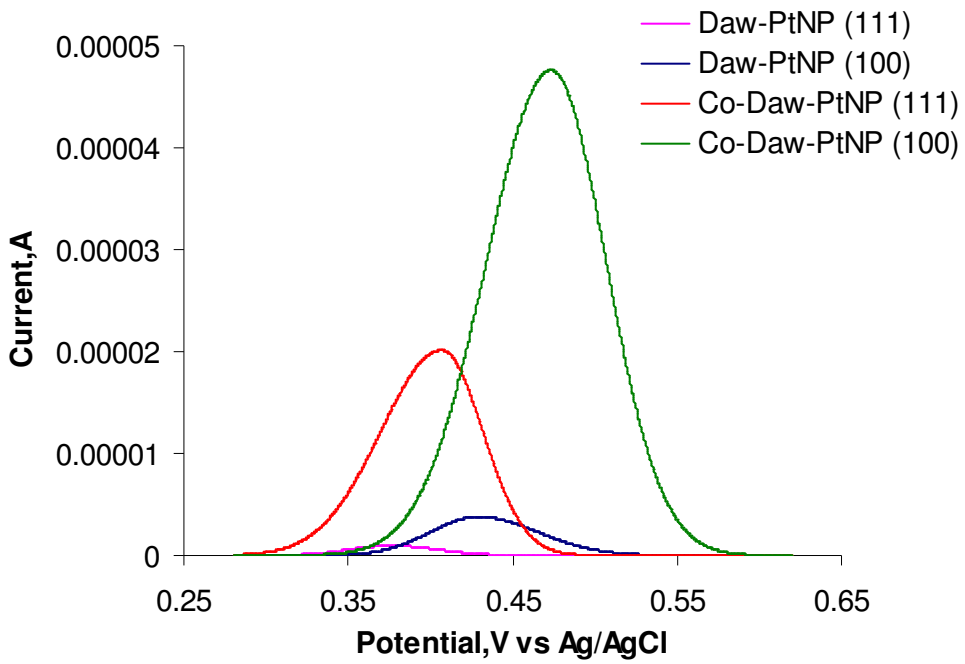

Fig. 2.12c Overlay of deconvoluted CO strip peaks associated with Co-Daw-PtNP and Daw-PtNP shown in Fig. 2.12a and 2.12b respectively.

Table 2.3 ECSA and peak potentials of CO strip peaks associated with Co-Daw-PtNP and Daw-PtNP catalysts

	ECSA, cm^2			Peak potential, mV	
Electrocatalyst	**(111)**	**(100)**	**Total**	**(111)**	**(100)**
Co-Daw-PtNP	0.372	1.03	1.40	407	473
Daw-PtNP	0.0153	0.0738	0.0891	376	429

Studies of CO oxidation on a regular cubo-octahedral Pt nanoparticle by Urgeghe et al. revealed that while CO is oxidized at a slow scan rate from Pt(111) facet, there occurs a surface diffusion of CO from Pt(100) facet to Pt(111) facet and hence the CO oxidation

charge associated with the less positive peak is greater than the one at more positive peak.[24] Finke and co-workers suggested that if a tridendate anion binds strongly on a metal surface site, then CO adsorption will be blocked on those sites.[13] The CO strip voltammogram (shown in Fig. 2.12a and 2.12b) obtained at a slow scan rate of 10 mV/s showed a less CO strip peak area at less positive potential when compared with more positive potential and this is due to the preferential adsorption of POM on (111) facet (which corresponds to less positive potential) preventing the CO to diffuse from (100) to (111) facet.

A 16-fold greater ECSA of CO strip corresponding to Co-Daw-PtNP (1.40 cm^2) than the CO strip obtained on Daw-PtNP (0.0891 cm^2) indicates that the site blocking effect of Co-Dawson is not as severe as observed in Daw-PtNP. It has been already observed in the previous work conducted by our research team that Dawson showed a negative shift in the $E_{1/2}$ of ORR on Pt(Poly) indicating the severe chemisorption than Co-Dawson where the $E_{1/2}$ of ORR was obtained with a positive shift.[5] We propose that the difference in the adsorption property between Dawson and Co-Dawson on Pt surface may arise from (i) the lattice-size matching or (ii) the difference in their anionic surface charge. Since the scope of our work is to study the synergetic effect of Co-center in Co-Dawson and Pt, we did not extend our work to probe the adsorption pattern of POM on the Pt surface.

Tsirlina et al. studied the adsorption property of Keggin type POMs (P- and Si-dodecatungstates) on Pt surface.[25] These authors have concluded that 5-20% of the Pt active sites will be completely blocked by the adsorption of POM which are modeled as large ball shaped bulky molecules. 55- 70% of the Pt active sites are under the projected region of POM. 25% of the Pt active sites are completely free and they lie between the

POM projections. We obtained a 16 fold variation in CO strip ECSA, but only 1.35 fold variation in kinetic current (for a loading of 20 $\mu g_{Pt}/cm^2$) between Co-Daw-PtNP and Daw-PtNP. We assume that a diatomic molecule like CO is unable to occupy the POM (Dawson) projected site due to the steric hindrance exerted by the adsorbed POM molecule. Similar to CO, dioxygen may not bind the Pt sites under the POM projected region but it can undergo reduction through e^- tunneling under the POM projected sites which is indicated from the number of e^- transferred n=1.4 to 2.2 in the K-L analysis. So, CO strip ECSA does not represent all the Pt sites that are involved in oxygen reduction. So calculating specific activity based on CO strip ECSA will not be meaningful.

So we compared the mass specific activity (which would be a good representation to show the effective Pt utilization) of both the systems. The mass specific activity of Co-Daw-PtNP at 500mV vs Ag/AgCl (770mV vs RHE) is 0.0711mA/μg_{Pt} and for Daw-PtNP is 0.0525 mA/μg_{Pt}. Co-Daw-PtNP showed 1.35 times greater mass specific activity than Daw-PtNP

The higher mass specific activity of Co-Daw-PtNP than Daw-PtNP can be attributed to two factors:

One possible factor is the Co-center in Co-Daw enhancing the O=O bond cleavage on Pt surface and the other is the severe active site blocking by the chemisorption of Dawson on Pt surface. To strongly support our hypothesis that Co-center in Co-Daw enhances the O=O bond cleavage, the chemisorption of POM on the Pt active site has to be eliminated or atleast minimized. In order to achieve this, we adopted the LBL technique[16], where the positively charged protonated cysteamine-stabilized PtNP which are monodispersed and the negatively charged POM can be assembled through the

electrostatic interaction on a GC substrate, there by minimizing the POM adsorption on the Pt surface.

2.3.5 Optimization of the number of bilayers of cysteamine-PtNP/POM in the LBL assembly:

LBL technique allows to optimize the number of bilayers in the ORR catalyst film. Fig. 2.13 compares the ORR voltammetric scans obtained on 6, 8, 10, 12 bilayers of cysteamine-PtNP and Co-Dawson (cysteamine-PtNP/Co-Daw LBL assembly) on a stationary GC electrode. When the number of bilayers of cysteamine-PtNP assembled with Co-Dawson reached 10, the most positive ORR $E_{1/2}$ (447 mV) was observed when compared with 6,8 and 12 bilayers implying the optimum number of bilayers with minimum resistance to O_2 mass transport and e^- transport in the film. On increasing the no of bilayers to 12, the ORR $E_{1/2}$ shifted to negative potential by 16 mV. After the optimization of the number of bilayers on a stationary GC electrode, the kinetic parameters were found using the 10 bilayers of cysteamine-PtNP/Co-Daw LBL assembly on a GC RDE.

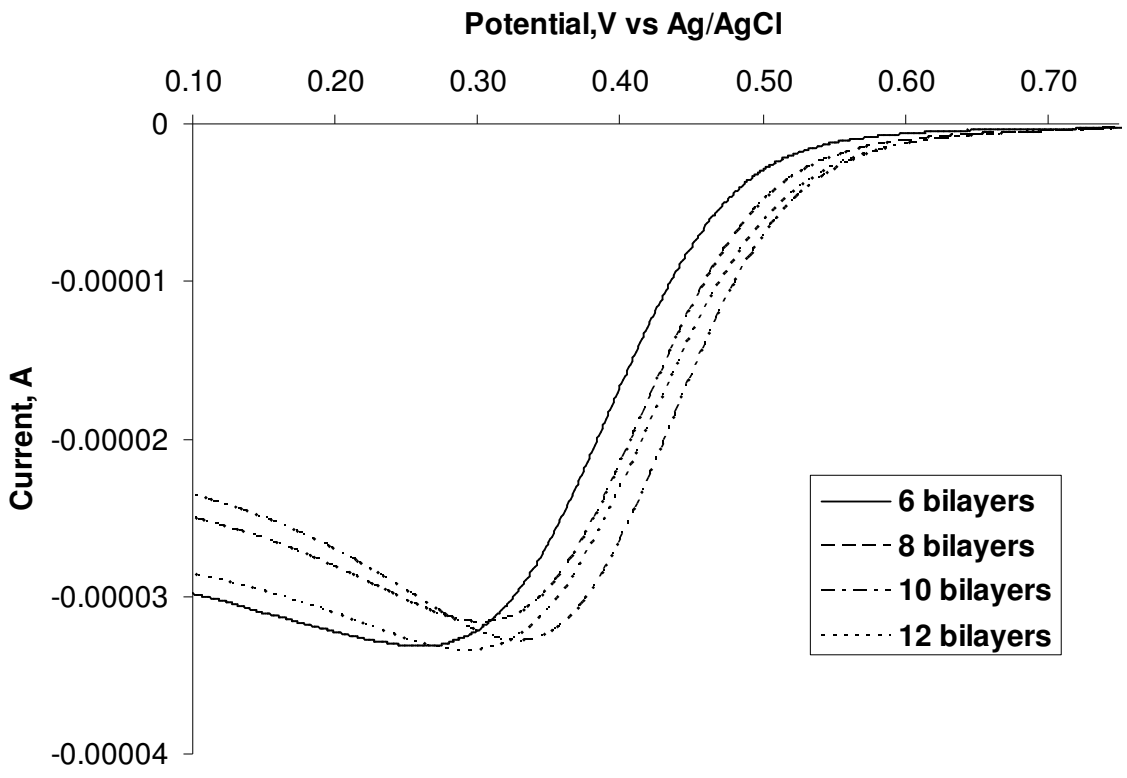

Fig. 2.13 Optimization of number of bilayers in cysteamine-PtNP/Co-Daw LBL assembly

2.3.6 ORR kinetic studies on cysteamine-PtNP/Co-Daw LBL assembly:

Fig. 2.14a shows the ORR voltammetric scans with increasing electrode rotation speed obtained on cysteamine-PtNP/Co-Daw LBL assembly. K-L plot analysis were done in the potential region where the ORR current is between 10 to 80% of the diffusion limited current, i_d at 900 rpm and the data are presented in Fig 2.14b and Table 2.4.

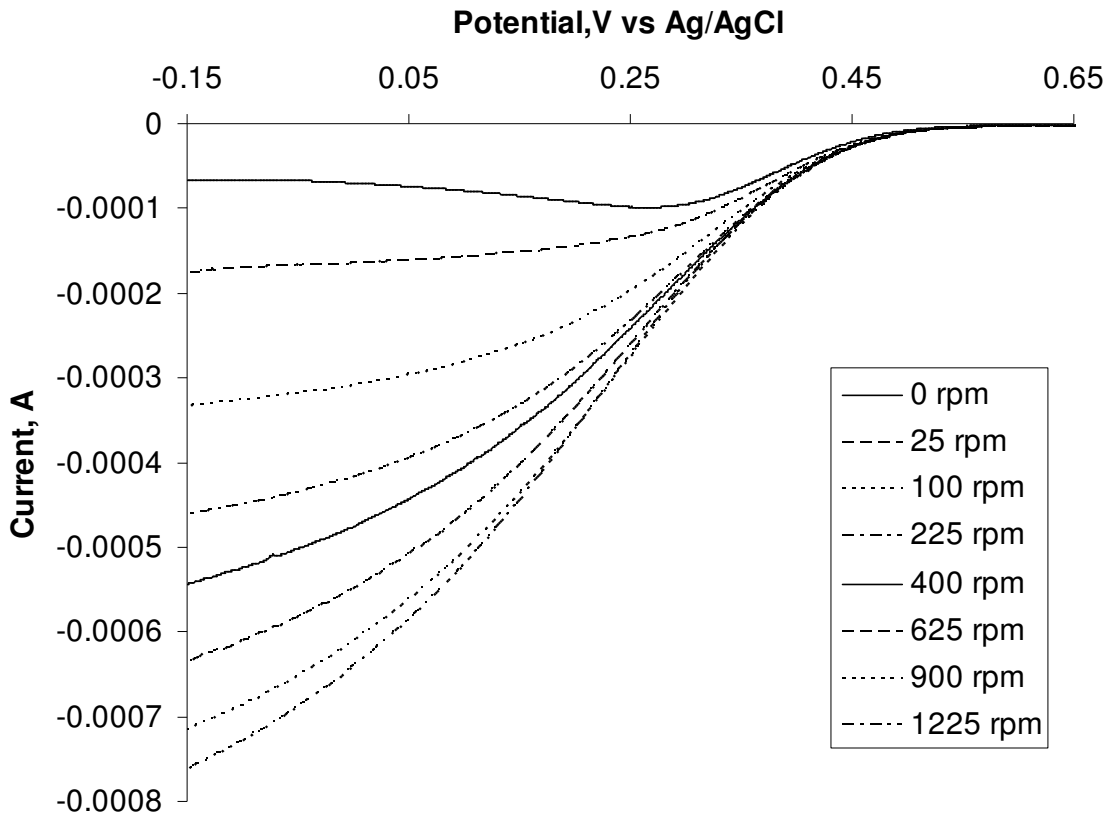

Fig. 2.14a ORR voltammetric scans of cysteamine-PtNP/Co-Daw LBL assembly

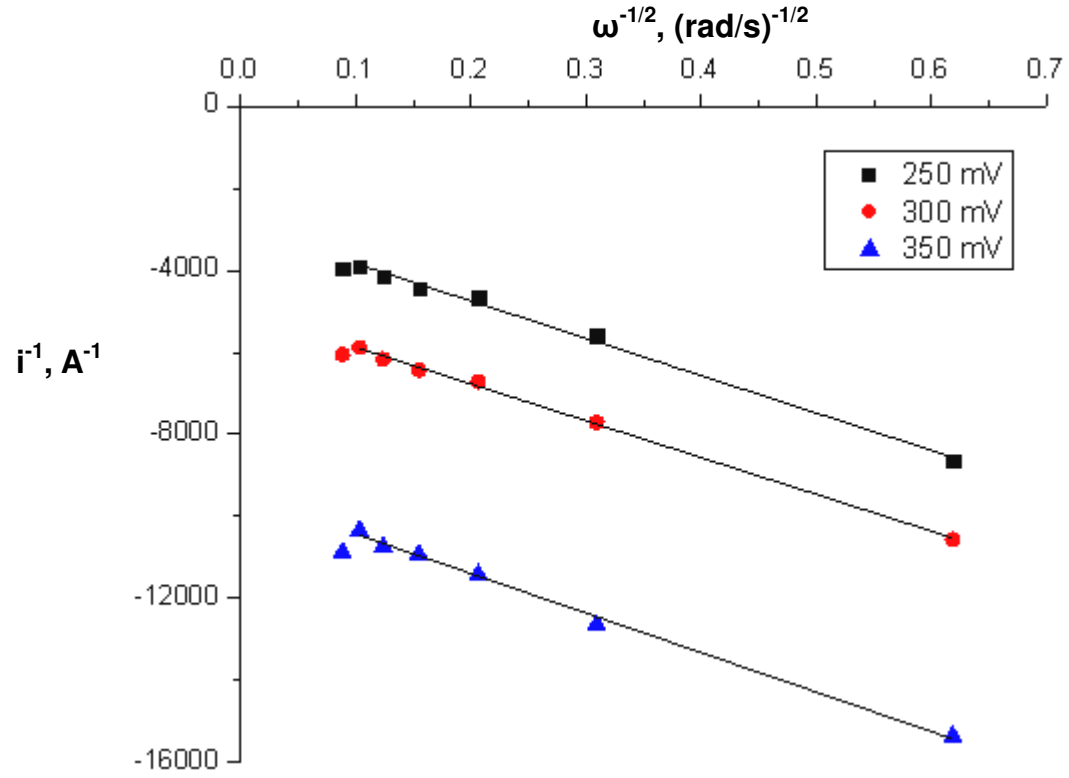

Fig. 2.14b K-L plot analysis of ORR on cysteamine-PtNP/Co-Daw LBL assembly.

Note: The data points at high electrode rotation speed (above 900 rpm) did not fit the linear model represented by K-L equation (Equation 2.1) due to the kinetic limitation for ORR caused by the blocking of Pt active sites by chemisorption of thiol molecules.

Table 2.4 Kinetic parameters associated with Fig. 2.14b:

Potential, mV	**n**	**i_k, mA**	**Specific activity, mA/cm$^2_{Pt}$**
350	3.2	0.106	0.386
300	3.4	0.201	0.734
250	3.4	0.342	1.25

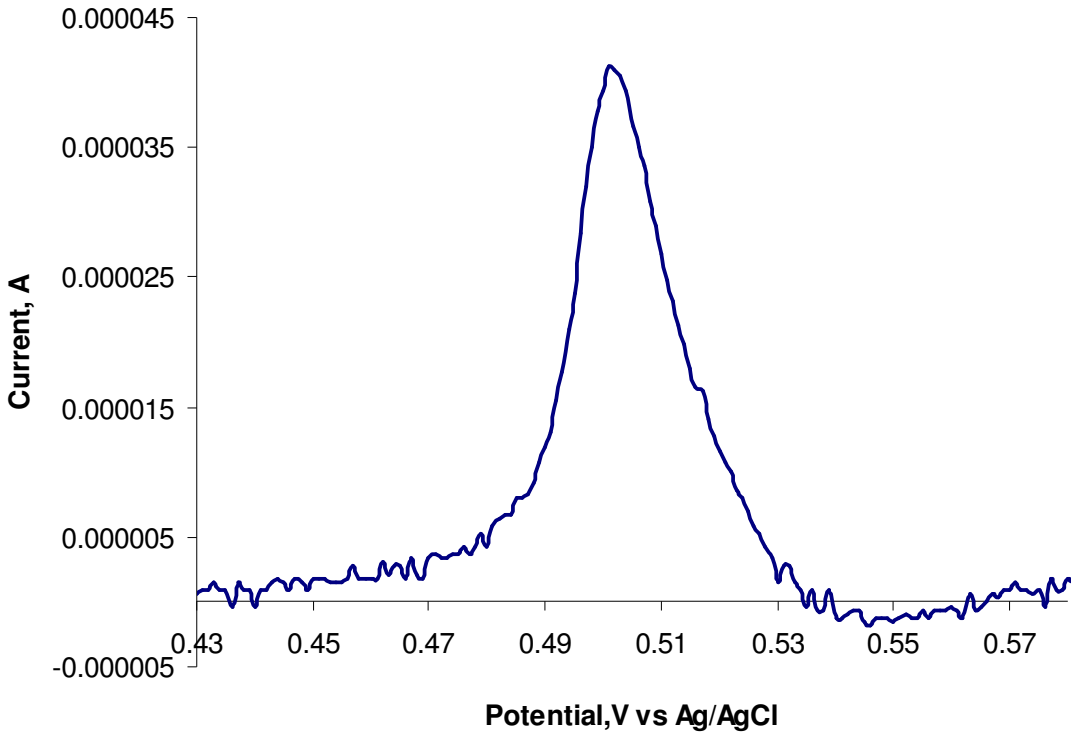

Fig. 2.15 CO strip voltammogram obtained on cysteamine-PtNP/Co-Daw LBL assembly.

(ECSA by CO strip is 0.274 cm^2)

The n < 4 in Table 2.4 indicates that the thiols bound on the Pt surface results in the lack of dual sites required for O=O bond cleavage leading to H_2O_2 formation along with H_2O as the ORR product. The poor ORR kinetics and H_2O_2 formation on cysteamine-PtNP/Co-Daw LBL assembly suggests that it is not a suitable system for fuel cell application, and our hypothesis is not confirmed using this system.

In order to avoid the site-blocking effect of cysteamine on PtNP surface towards ORR, PtNP were prepared using a cationic polymer stabilizer and assembled with the anionic POM on a GC substrate through the electrostatic interaction. The polymer PDDA

interacts with the PtNP by physisorption (the quaternary ammonium groups of PDDA electrostatically interact with the chemisorbed Cl^- on the Pt surface), so the site blocking effect is not significant in PDDA-stabilized PtNP.[18,19] The flexible polymer chain favours the easy access of the reactants to reach the Pt active sites. It has been proved that the catalytic activity towards ORR or MeOH oxidation showed improved results on PDDA-stabilized PtNP among other polyelectrolytes like poly(allylamine hydrochloride), Nafion, poly(acrylic acid), etc., as PDDA does not block the Pt active sites.[18]

2.3.7 Optimization of the number of bilayers of PDDA-PtNP/POM in the LBL assembly:

Fig. 2.16 compares the ORR voltammetric scans obtained on 8, 10, 12 bilayers of PDDA-PtNP and Co-Dawson on a stationary GC electrode. The optimum number of bilayers was found to be 10 with an ORR $E_{1/2}$ of 465 mV. There was a negative shift of 21 mV in ORR $E_{1/2}$ when the number of bilayers is increased to 12. After the optimization of the number of bilayers on a stationary GC electrode, the kinetic parameters were found using the 10 bilayers of PDDA-PtNP/Co-Daw LBL assembly on a GC RDE. 10 bilayers of PDDA-PtNP/Daw assembly on GC electrode was used for the control experiment.

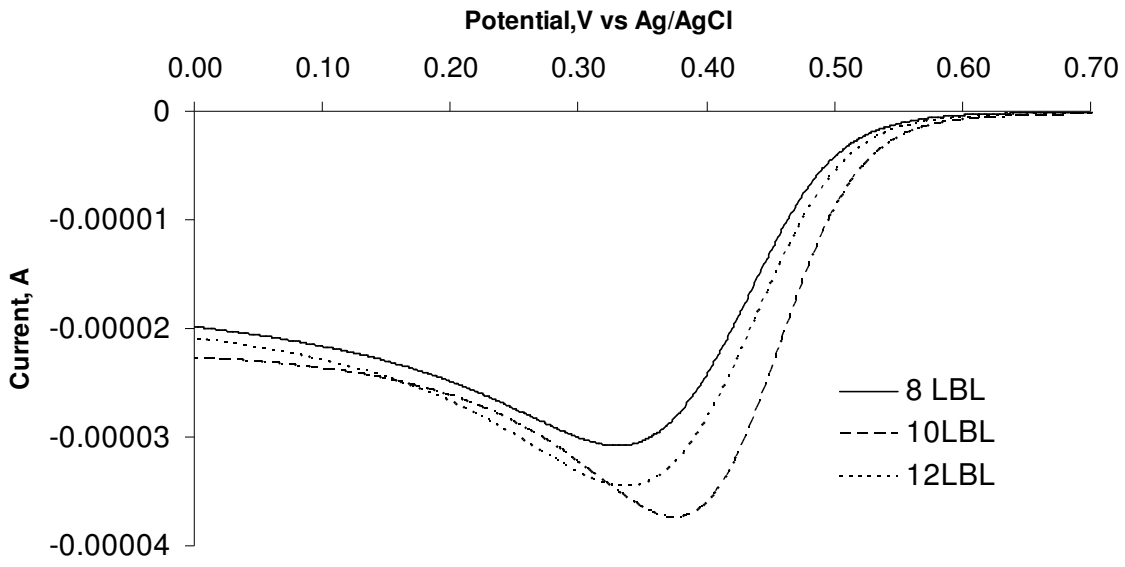

Fig. 2.16 Optimization of the number of bilayers in PDDA-PtNP/Co-Daw LBL assembly

2.3.8 ORR performance on PDDA-PtNP/POM LBL assembly:

ORR voltammetric scan of PDDA-PtNP/Co-Daw and PDDA-PtNP/Daw LBL assemblies are shown in Fig. 2.17a and Fig. 2.18a respectively. The corresponding K-L plots are shown in Fig. 2.17b and Fig. 2.18b respectively. The ORR kinetic parameters associated with PDDA-PtNP/Co-Daw and PDDA-PtNP/Daw are given in Table 2.5 and Table 2.6 respectively.

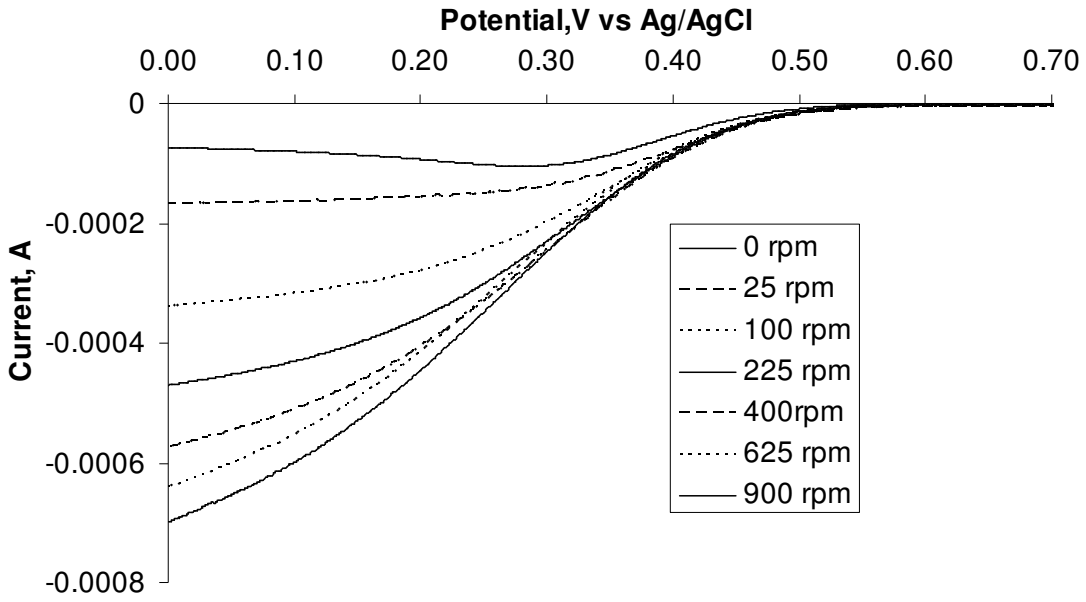

Fig. 2.17a ORR voltammetric scans of PDDA-PtNP/Co-Daw LBL assembly

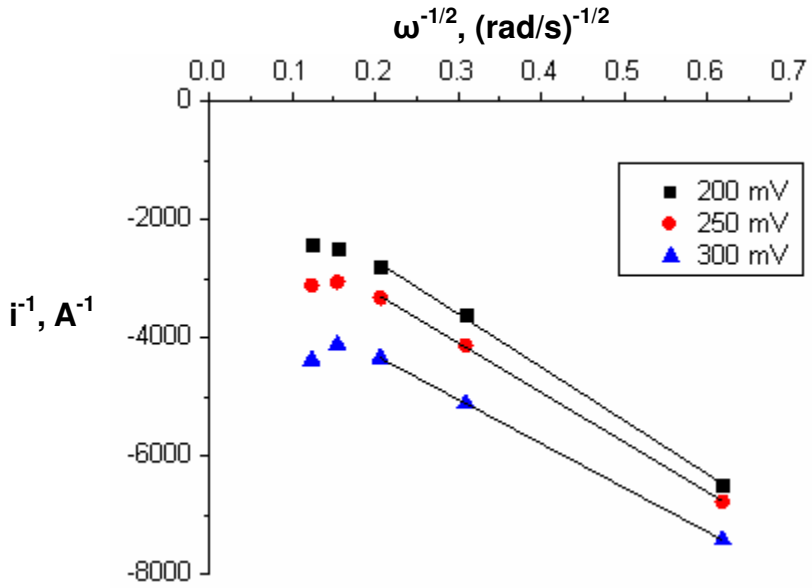

Fig. 2.17b K-L plot analysis of ORR on PDDA-PtNP/Co-Daw LBL assembly.

Note: The data points at high electrode rotation speed (above 225 rpm) did not fit the linear model represented by K-L equation (Equation 2.1) due to the lack of sufficient Pt active sites as PDDA-PtNP/Co-Daw LBL assembly has low Pt loading (3.78 $\mu g_{Pt}/cm^2$).

Table 2.5 Kinetic parameters associated with Fig. 2.17b

Potential, mV	n	i_k, mA	Specific activity, mA/cm^2_{Pt}
300	4.1	0.357	2.92
250	3.7	0.639	5.23
200	3.4	1.13	9.25

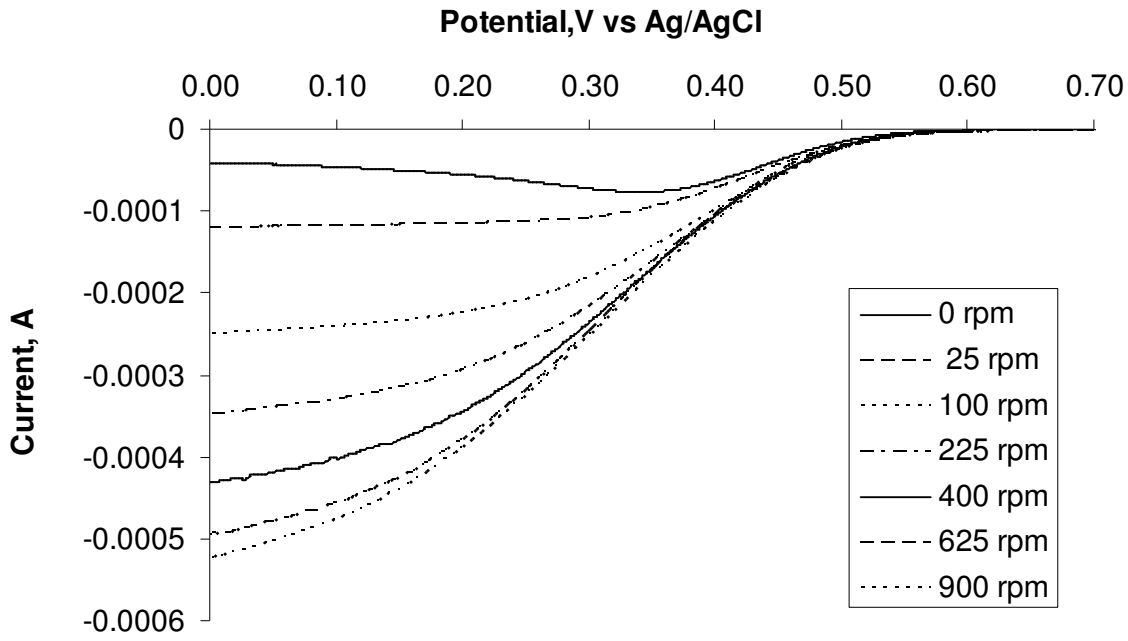

Fig. 2.18a ORR voltammetric scans of PDDA-PtNP/Daw LBL assembly

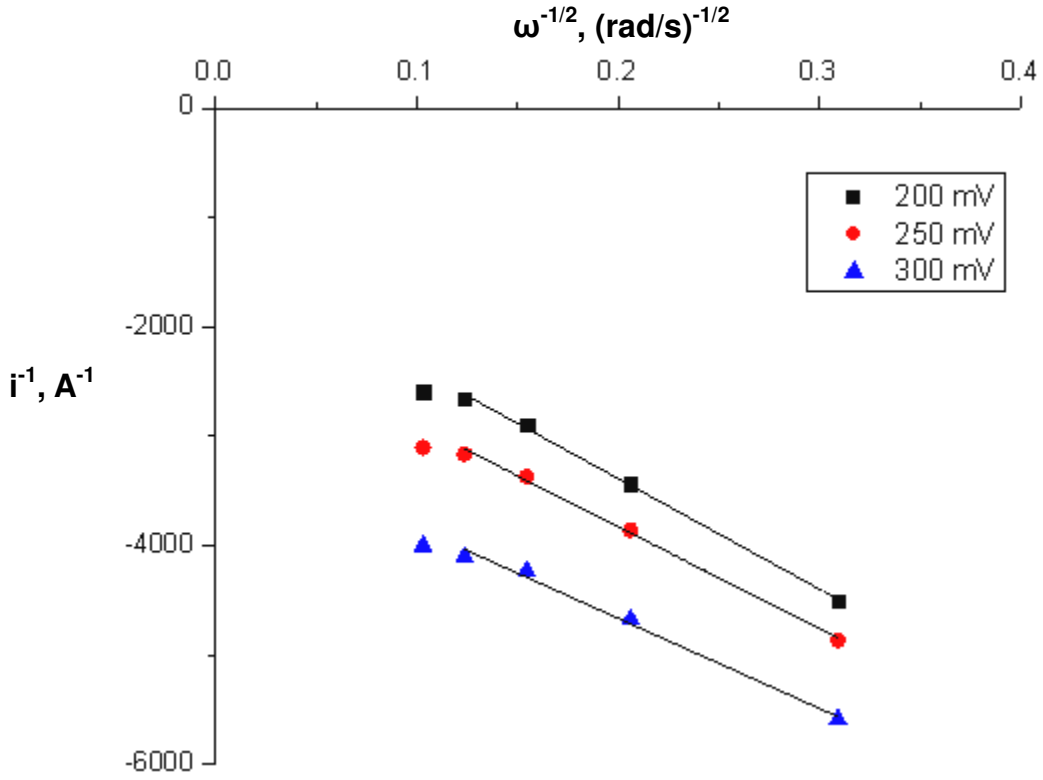

Fig. 2.18b K-L plot analysis of ORR on PDDA-PtNP/Daw LBL assembly.

Note: The data point at high electrode rotation speed (above 625 rpm) did not fit the linear model represented by K-L equation (Equation 2.1) due to the lack of sufficient Pt active sites as PDDA-PtNP/Daw LBL assembly has low Pt loading (5.52 $\mu g_{Pt}/cm^2$).

Table 2.6 Kinetic parameters associated with Fig. 2.18b

Potential, mV	n	i_k, mA	Specific activity, mA/cm^2_{Pt}
300	3.7	0.332	2.28
250	3.3	0.510	3.50
200	3.1	0.732	5.03

In the case of PDDA-PtNP/Co-Daw LBL assembly, the K-L plot analysis showed "n"(number of e^- transferred) from 3.4 to 4 in the potential range 200 to 300 mV vs Ag/AgCl (given in Table 2.5) and for PDDA-PtNP/Daw LBL assembly, n ranged from 3.1 to 3.7 (given in Table 2.6). The obtained 'n' values indicate that ORR follows a mixed 2 and 4 e^- reduction mechanism on both these catalysts. When ORR follows a $2e^-$ reduction pathway to produce H_2O_2, the formed H_2O_2 can easily escape from the catalyst surface without further reduction to water under low Pt loading on a rotating disc electrode.[26] The formed H_2O_2 has less chance to get adsorbed on another (near by) Pt active site for further reduction to H_2O. SEM image (shown in Fig. 2.7 and 2.8) of these LBL assemblies indicate a low surface coverage of PtNP (3.78 $\mu g_{Pt}/cm^2$ for PDDA-PtNP/Co-Daw LBL assembly and 5.52 $\mu g_{Pt}/cm^2$ for PDDA-PtNP/Daw LBL assembly) on the GC surface. So, there is a possibility for the formed H_2O_2 to get escaped (during the rotation of the electrode) without further reduction to H_2O causing 'n' less than 4.

Fig. 2.19 and 2.20 represent the CO strip voltammograms carried on PDDA-PtNP/Co-Daw and PDDA-PtNP/Daw LBL assemblies. The corresponding ECSA and peak potentials are listed in Table 2.7.

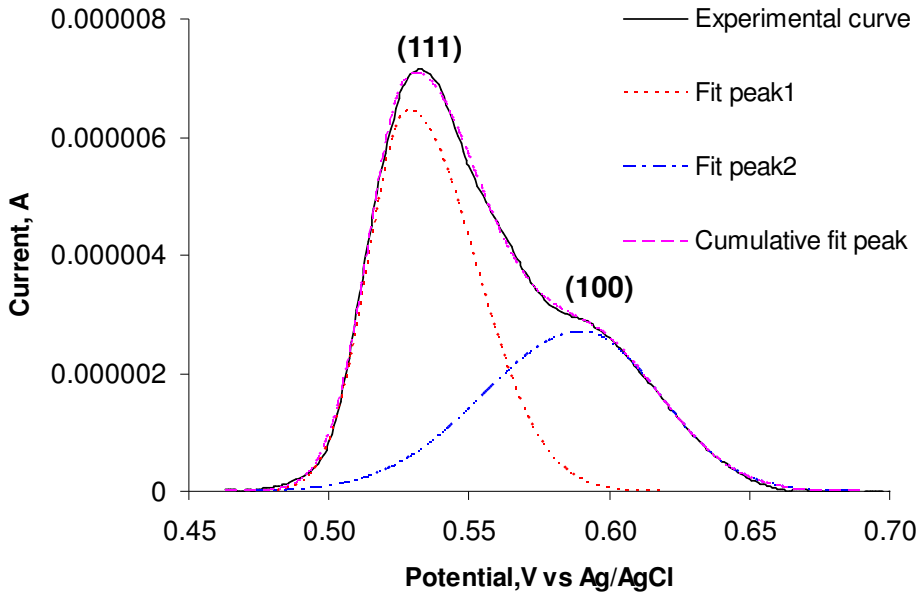

Fig. 2.19 CO strip voltammogram obtained on PDDA-PtNP/Co-Daw LBL assembly. The deconvolution of CO strip curve was performed using the BiGaussian function (OriginPro 8.6 32Bit).

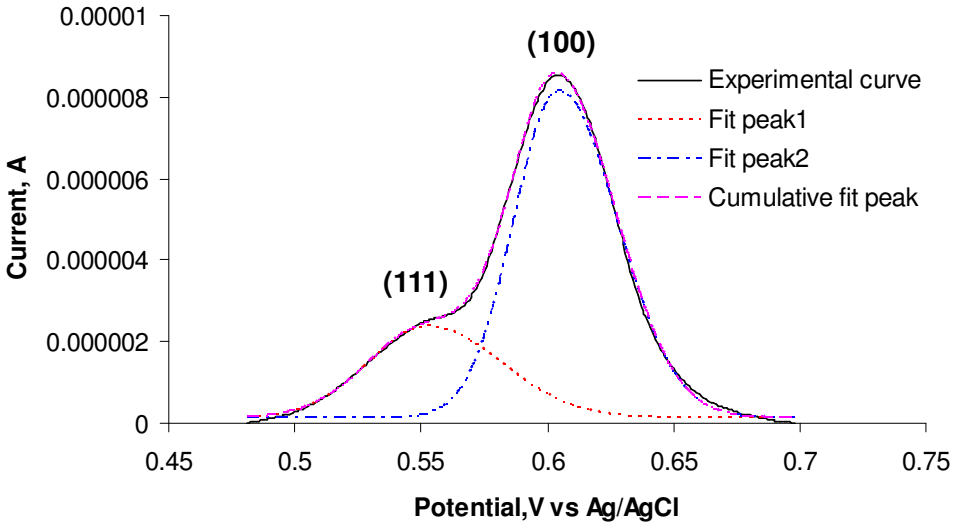

Fig. 2.20 CO strip voltammogram obtained on PDDA-PtNP/Daw LBL assembly. The deconvolution of CO strip curve was performed using the BiGaussian function (OriginPro 8.6 32Bit).

Table 2.7 ECSA and peak potentials of CO strip peaks associated with PDDA-PtNP/POM LBL assemblies

	ECSA, cm^2			Peak potential, mV	
Electrocatalyst	**111**	**100**	**Total**	**111**	**100**
PDDA-PtNP/Co-Daw	0.0723	0.0498	0.1221	528	590
PDDA-PtNP/Daw	0.0416	0.104	0.1456	553	605

As per Urgeghe findings, CO oxidation charge was more from (111) facet which peaks at a less positive Potential than the CO oxidation charge from (100) facet associated with the more positive potential while performing the CO strip voltammogram at a slow scan rate.[24] We observed the same pattern in PDDA-PtNP/Co-Daw LBL assembly (Fig. 2.19). In the case of PDDA-PtNP/Daw LBL assembly (Fig. 2.20), the CO strip ECSA associated with less positive peak from Pt(111) facet was less than the one (more positive peak) from Pt(100). This implies that the CO is prevented to diffuse from Pt(100) to Pt(111) facet due to the chemisorption (site blocking) of Dawson on Pt(111) facet during the LBL assembly. Replicate CO strip experiments on these LBL catalysts gave consistent results. However, comparable ECSA of CO strip obtained on both PDDA-PtNP/Co-Daw and PDDA-PtNP/Daw (Table 2.7) indicates that PDDA has greatly reduced the adsorption of Dawson on PtNP.

At 300 mV vs Ag/AgCl, the mass specific activity of PDDA-PtNP/Co-Daw is 0.337 $mA/\mu g_{Pt}$ and that of PDDA-PtNP/Daw is 0.215 $mA/\mu g_{Pt}$. The mass specific activity of PDDA-PtNP/Co-Daw is 1.57 times greater than that of PDDA-PtNP/Daw. The specific activity of PDDA-PtNP/Co-Daw is 2.92 mA/cm^2_{Pt} and that of PDDA-PtNP/Daw is 2.28 mA/cm^2_{Pt} at 300 mV vs Ag/AgCl. The specific activity of PDDA-PtNP/Co-Daw is 1.28

times greater than that of PDDA-PtNP/Daw and it proves our hypothesis that Co-Dawson is a better co-catalyst than Dawson on the Pt surface due to the presence of Co-center which enhances the O=O bond cleavage. Above 300mV, there is no significant increase in the ORR current for the increased electrode rotational speed, probably due to the low Pt loading, so the K-L analysis gave n >4 for PDDA-PtNP/Co-Daw indicating that the K-L analysis is inaccurate. So it is not advisable to extract the kinetic parameters such as kinetic current above 300 mV.

But at or below 300 mV, neither specific activity nor mass specific activity is available for the commercial Pt/C. So, we are unable to compare the kinetic parameters of PDDA-PtNP/Co-Daw with the commercial Pt/C.

The ORR $E_{1/2}$ (465 mV) with the optimized number of bilayers showed less positive $E_{1/2}$ when compared with the commercial Pt/C (580 to 630 mV) due to the low loading of Pt. On increasing the Pt loading, while optimizing the number of bilayers, $E_{1/2}$ further shifted to the negative potentials possibly due to the resistance offered by the incorporated PDDA to e^- transfer with in the film.

2.4 Conclusions

POM-stabilized PtNP catalyst system did not prove our hypothesis unambiguously due to the severe chemisorption of Dawson on Pt active sites. PtNP-POM catalyst system prepared by LBL technique, though not completely prevented the POM adsorption on PtNP, has greatly reduced the extent of POM adsorption on PtNP. The concomitant incorporation of free PDDA while increasing the number of bilayers in order to increase the Pt loading could resist e^- transfer within the LBL film. It may prevent the ORR performance of the catalyst (PDDA-PtNP/Co-Daw) from reaching the ORR performance

of commercial Pt/C catalyst. However, with PDDA-PtNP/POM catalyst system we were able to prove our hypothesis that Co-center in Co-Dawson helps promote O=O bond cleavage and transfer the split O atom to the Pt surface.

The future studies can be directed to increase the Pt loading with no resistance to e^- transfer. One possible way to achieve this is by preparing PtNP stabilized by a conducting material like carbon nanotube (CNT) and assemble them with POM. The conducting stabilizer can increase the Pt loading without affecting the e^- transport in the LBL film.

References:

(1) Gasteiger, H. A.; Kocha, S.S.; Sompalli, B.; Wagner, F.T. *Applied Catalysis B: Environmental* **2005**, *56*, 9–35.

(2) Mukerjee, S.; Srinivasan, S.; Soriaga, M. P.; McBreen, J. *J. Electrochem. Soc.* **1995***, 142*, 1409-1422.

(3) Stamenkovic´, V.; Schmidt, T. J.; Ross, P. N.; Markovic´, N. M. *J. Phys. Chem. B* **2002,** *106,* 11970-11979.

(4) Fernandez, J. L.; Walsh, D. A.; Bard, A. J. *J. Am. Chem. Soc.* **2005**, *127*, 357-365.

(5) Sankarraj, A. V.; Ramakrishnan, S.; Shannon, C. *Langmuir* **2008,** *24,* 632-634.

(6) Borrás-Almenar, J. J.; Coronado, E.; Müller, A. *Polyoxometalate Molecular Science*, Kluwer Academic Publishers, Netherlands. 2001.

(7) Chojak, M.; Kolary-Zurowska, A.; Wlodarczyk, R.; Miecznikowski, K.; Karnicka, K.; Palys, B.; Marassi, R.; Kulesza, P. J. *Electrochim. Acta* **2007**, *52*, 5574-5581.

(8) Mioc, U.B.; Todorovic´, M.R.; Davidovic´, M.; Colomban, Ph.; Holclajtner-Antunovic´, I. *Solid State Ionics* **2005**, *176*, 3005 – 3017.

(9) Khenkin, A.M.; Weiner, L,; Wang, Y.; Neumann, R. *J. Am. Chem. Soc.* **2001,** *123,* 8531-8542.

(10) Sadakane, M.; Steckhan, E. *Chem. Rev.* **1998,** *98,* 219-237.

(11) Hill, C.L.; Brown, R.B. *J. Am. Chem. Soc.* **1986***, 108,* 536.

(12) Kharat, A. N.; Abedini, M.; Amini, M. M.; Pendleton, P.; Badalyan, A. *Transition Metal Chemistry* **2003**, *28*, 339–344.

(13) Finke, R. G.; Özkar, S. *Coordination Chemistry Reviews* **2004**, *248*, 135–146.

(14) Niu, C.; Wu, Y.; Wang, Z.; Li, Z.; Li, R. *Front. Chem. China* **2009**, *4*, 44–47.

(15) Troupis, A.; Hiskia, A.; Papaconstantinou, E. *Angew. Chem. Int. Ed.* **2002**, *41*, 1911-1914.

(16) Ariga, K.; Hill, J. P.; Ji, Q. *Phys. Chem. Chem. Phys.*, **2007**, *9*, 2319–2340.

(17) Eklund, S. E.; Cliffel, D. E. *Langmuir* **2004,** *20,* 6012-6018.

(18) Tian, Z. Q.; Jiang, S. P. ; Liu, Z. ; Li, L. *Electrochemistry Communications* **2007**, *9*,1613–1618.

(19) Jiang, S. P.; Liu, Z.; Tang, H. L.; Pan, M. *Electrochim. Acta* **2006**, *51*, 5721–5730.

(20) Chen, C.C.; Bose, C.S.C.; Rajeshwar, K. *J. ElectroanaL Chem.* **1993**, *350*, 161-176.

(21) Mayrhofer, K. J. J.; Strmcnik, D.; Blizanac, B.B.; Stamenkovic, V.; Arenz, M.; Markovic, N.M. *Electrochimica Acta* **2008,** *53,* 3181–3188.

(22) Schmidt, T. J.; Paulus, U. A.; Gasteiger, H.A.; Behm, R.J. *J. Electroanal. Chem.* **2001**, *508*, 41–47.

(23) Ge, M.; Zhong, B.; Klemperer, W. G.; Gewirth, A. A. *J. Am. Chem. Soc.* **1996,** *118,* 5812-5813.

(24) Kinge, S.; Urgeghe, C.; Battisti, A. D.; Bönnemann, H. *Appl. Organometal. Chem.* **2008**, *22*, 49–54.

(25) Mishina, E. D.; Tsirlina, G. A.; Timofeeva, E. V.; Sherstyuk, N. E.; Borzenko, M. I.; Tanimura, N.; Nakabayashi, S.; Petrii, O. A. *J. Phys. Chem. B* **2004,** *108,* 17096-17105.

(26) Inaba, M.; Yamada, H.; Tokunaga, J.; Tasaka, A. *Electrochemical and Solid-State Letters* **2004**, *7***,** A474-A476.

Chapter 3

Screening the optical properties of Ag-Au alloy gradients formed by bipolar electrodeposition using surface enhanced Raman spectroscopy

3.1 Introduction:

Several promising new applications of bipolar electrochemistry have emerged over the past 10 years.[1] For example, in a series of recent reports,[2-4] Crooks and co-workers have shown how electrochemical techniques for concentrating, separating, and detecting analytes in microfluidic channels can be implemented using bipolar electrodes (BPEs). Björefors et al.[5,6] have demonstrated the ability to generate and manipulate chemical concentration gradients of organic adsorbates using bipolar electrochemistry. Choi and Buriak have reported the use of current pulse techniques to electrodeposit metal oxides in a bipolar format.[7] Warakulwit et al. showed that asymmetric metal-modified carbon nanotubes could be generated in a capillary electrophoresis channel.[8] Recently, our research group introduced the concept of bipolar electrodeposition (BP-ED) and demonstrated the use of this approach to generate solid-state material libraries along the length of a BPE.[9]

An electronic conductor immersed in an ionically conductive phase can function as a BPE if it experiences a sufficiently large electric field.[10] Typically, the field is generated by applying an appropriate voltage between two driver electrodes immersed in an electrolyte that also contains the BPE. The equilibrium potential of the BPE is determined by its chemical composition and that of the supporting electrolyte; in addition, due to the

linear potential drop that exists in solution, a cathodic overpotential develops at one end of the BPE and an anodic overpotential at the other end. At points between the two poles, the interfacial potential difference will be a function of lateral position along the axis of the BPE parallel to the electric field. If redox active species are present in solution, faradaic reactions can take place at the BPE-solution interface provided that the applied potential exceeds the difference in formal potentials between the anodic and cathodic half-reactions (which occur in parallel to maintain charge balance).[11,12]

Electrodeposition has been a commonly used technique for the growth of binary metal alloys for over 50 years.[13] In the case of electrodeposited Ag-Au alloys, it has been found that although Ag deposition is thermodynamically favored (i.e., $E^0_{Ag} > E^0_{Au}$), Au deposition is kinetically favored; thus, the chemical composition of electrodeposited Ag-Au alloys is dependent on the applied potential.[14,15]

In this study, we used BP-ED to deposit Ag-Au alloy chemical composition gradients on stainless steel substrates, exploiting the fact that the interfacial potential varies along the length of the BPE. The interfacial potential gradient causes the rates of electrodeposition of Ag and Au to vary along the length of the BPE, leading to the electrodeposition of a chemical concentration gradient. After characterizing the alloy gradients using scanning electron microscopy (SEM) and energy dispersive X-ray spectroscopy (EDX), self-assembled monolayers of a Raman-active probe molecule (benzene thiol) were allowed to form on the surface of the alloy gradient and confocal Raman microscopy was employed to determine the alloy composition that resulted in the maximum surface enhanced Raman scattering (SERS) intensity. Variations of SERS intensity could be explained on the basis of the optical properties of the electrodeposited

alloy. These experiments clearly demonstrate the utility of using BP-ED for the synthesis of thin film materials libraries which can be screened using a wide variety of surface analytical tools.

3.2 Experimental Section:

3.2.1 Materials: $HAuCl_4$ (30 wt % solution in dilute HCl, 99.99%, Sigma-Aldrich), $AgNO_3$ (>99% ACS reagent, Aldrich Chemical Co.), KCN (99.5% ACS reagent, Fisher Scientific Company), and KOH (87.1%, Fisher Scientific Company) were used as received. Glassy carbon rods (2 mm diameter, SPI Supplies, Inc.) were used to fabricate the driver electrodes used for bipolar electrochemistry. Millipore-Q purified deionized (DI) water (18.2MΩ/cm^3) was used to make up all solutions and to rinse electrodes.

3.2.2 Substrate Preparation: Stainless steel 304 substrates 18 mm in length and 2mm wide were mechanically polished with 800 grit SiC paper and sonicated in water for 5min. They were cleaned by rinsing sequentially with distilled water, absolute ethanol, room temperature piranha solution (1:3 v/v 30% H_2O_2, 18M H_2SO_4), and distilled water. After being dried in a stream of flowing nitrogen, the clean stainless steel bipolar electrode was placed into the electrochemical cell. Glassy carbon driver electrodes were prepared by rinsing sequentially with distilled water, absolute ethanol, and distilled water, and were dried in a stream of flowing nitrogen.

3.2.3 Electrochemistry: All conventional (unipolar) electrochemistry measurements were performed using a standard three electrode configuration in a home-built glass cell. In all cases, we used a stainless steel working electrode, a Pt counter electrode, and a Ag|AgCl(sat) (Bioanalytical Systems, Inc.) reference electrode. The electrochemical cell was controlled using an Epsilon electrochemistry workstation (Bioanalytical Systems,

Inc.).

All bipolar electrochemistry experiments were performed in a home-built single compartment glass cell (ca. 15mL total volume) using a Hewlett-Packard model 6010 regulated DC power supply to control the potential applied between two glassy carbon driver electrodes separated by 2.0 cm. The electrically floating stainless steel BPE was placed symmetrically between the two driver electrodes, as previously reported.[9] The three electrodes were immersed in an electrodeposition solution containing 50 mM $KAu(CN)_4$, 50 mM $K_2Ag(CN)_3$, 200 mM KCN, and 10 mM KOH (pH 12). Ag-Au alloy films were deposited by applying a voltage of 9.5 V across the driver electrodes for 1 min at room temperature under deaerated conditions. The BPE was then rinsed with DI water, dried in a stream of flowing nitrogen, and placed in a covered container prior to analysis using SEM and EDX.

3.2.4 Formation of Benzene Thiol Self-Assembled Monolayers: A freshly deposited Au-Ag alloy gradient was immediately immersed in a 5 mM ethanolic solution of benzene thiol for 15 h. After monolayer formation, the specimen was rinsed with ethanol and dried in Ar prior to analysis by confocal Raman microscopy.

3.2.5 Scanning electron microscopy (SEM)/ Energy dispersive X-ray spectroscopy (EDX) Measurements: SEM images were collected using a JEOL JSM-7000F field-emission scanning electron microscope and analyzed using the EOS 7000F software package. EDX data were acquired using an Oxford X-Max energy dispersive X-ray spectrometer and were analyzed using the INCA software package.

3.2.6 Raman Microscopy: Raman scattering was excited using the 514 nm output (ca. 20 mW) from an air-cooled argon ion laser (model 163-C42, Spectra-Physics Lasers, Inc.)

and the 785 nm (300 mW) output from a wavelength-stabilized high power laser diode system (model SDL-8530, SDL Inc.). Raman measurements were acquired as a function of position along the length of the bipolar electrode and analyzed using a Renishaw inVia Raman microscope system. Raman signals were accumulated for 40 s.

3.3 Results and Discussion:

3.3.1 Ag-Au alloy gradient by bipolar electrodeposition:

The growth of Ag-Au alloy films onto Au surfaces using constant potential electrodeposition in a three-electrode (unipolar) configuration has been investigated by Bozzini and co-workers.[15] By applying fixed potentials between -0.7 and -1.3 V vs Ag|AgCl(sat), Ag-Au alloy thin films ranging from about 25 to 87 atom % Ag could be grown. These workers observed an approximately linear dependence of the alloy composition on the deposition potential, arising from the potential dependence of the rate of electrodeposition of each element. X-ray diffraction measurements showed a systematic increase in the fcc lattice parameter as the atomic percent of Au in the electrodeposit increased, consistent with the formation of single phase Ag-Au alloy films. Based on these findings, we reasoned that BP-ED carried out from a solution of similar chemical composition to that employed by Bozzini et al. could be used to generate Ag-Au alloy gradients on the surface of BPEs.

We deposited Au-Ag alloy gradients near the cathodic pole of polished stainless steel BPEs by applying a voltage of 9.5 V across the driver electrodes for a period of 60 s. The appropriate driving voltage was estimated from conventional (unipolar) linear sweep voltammetry (LSV) using a stainless steel working electrode immersed in the deposition bath. From these measurements, the cathodic limit of Ag-Au alloy deposition was

estimated to be ca. -1.400 V, while the open circuit potential of the stainless steel electrode was found to be -0.168 V vs Ag|AgCl(sat). Assuming that the equilibrium potential of the BPE would float to a value close to the open circuit potential of the unipolar stainless steel electrode, and placing the BPE symmetrically between the two driver electrodes, we calculated a value of 2.464 V (twice the difference between the cathodic limit and the OCP) as the potential difference required between the two poles of the BPE in order to access the full range of Ag-Au alloy deposition potentials. An applied voltage of 9.5 V between the driver electrodes was required to achieve this potential difference. Also, under these conditions, it is likely that the anodic half-reaction corresponds to the generation of molecular oxygen from dissolved hydroxide ions.

The surface morphology of the Ag-Au alloy films produced using BP-ED was studied using SEM. To avoid issues pertaining to the effect of crystallite size on the physical properties of the alloy, we carefully optimized the electrodeposition conditions to ensure that the morphology of the polycrystalline electrodeposits was as uniform as possible near the cathodic pole of the BPE (about 3 mm total length). All characterization data discussed herein was collected within this zone. The region of interest shown in Fig. 3.1 is approximately 5.3 μm in height and 8.5 μm wide, corresponding to a surface area of ca. 45 μm^2. This image is typical of what we observed across the alloy gradient and reveals a uniform coverage of electrodeposited material composed of a broad distribution of roughly spheroidal surface asperities with an average diameter of 85 ± 48 nm (measured in the surface plane). By imaging film defects using SEM, the thickness of the deposit was estimated to be roughly 2 μm.

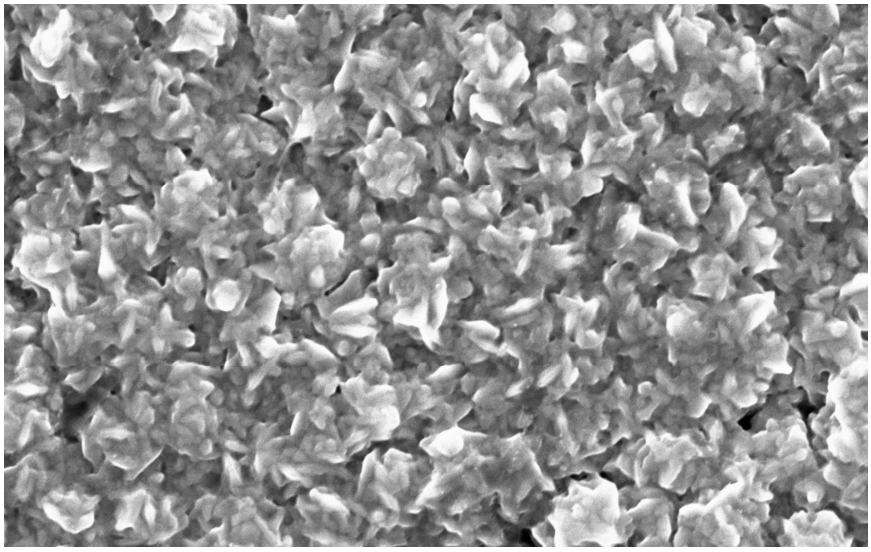

Fig. 3.1 SEM image of the surface of a Ag-Au alloy gradient deposited onto stainless steel using bipolar electrodeposition. A region of interest that is ca. 5.3 μm by 8.5 μm is shown.

Atomic percentages of Ag and Au in the alloy gradients were calculated from EDX spectra acquired as a function of position along the principal axis of the BPE, and a plot of the composition data is shown in Fig. 3.2. The Ag-Au alloy gradients formed under our BP-ED conditions ranged from approximately 55%Ag to 100% Ag, with a nearly linear variation of the surface atomic percentage as a function of lateral position. This finding, taken together with Bozzini's observation of a linear composition dependence on applied potential suggests that the electric potential at the BPE-solution interface varies approximately linearly along the length of the BPE, consistent with previous research.[16] Finally, no EDX peaks originating from the underlying stainless steel substrate were observed in these experiments.

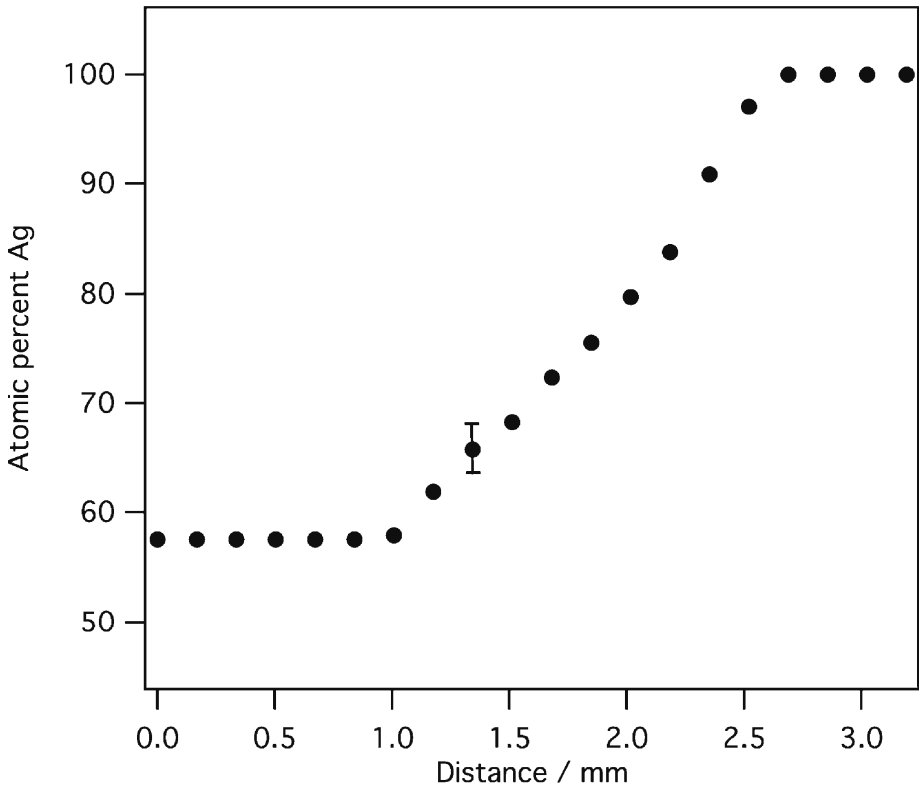

Fig. 3.2 Chemical composition of a Ag-Au alloy gradient deposited onto stainless steel using bipolar electrodeposition as a function lateral position along the BPE determined by EDX. To avoid visual clutter, only a single error bar is shown, which is representative of typical errors observed.

The composition of the alloys formed by BP-ED can be understood on the basis of Faraday's law, which states that the instantaneous composition of a binary alloy depends on the partial current for the electrodeposition of each element. For Ag-Au, we write formally:

$$Ag(CN)_2^- + 2e^- = Ag + 2CN^- \qquad E0' = -0.27\ V \qquad (3.1)$$

$$Au(CN)_2^- + 2e^- = Au + 2CN^- \qquad E0' = -0.47\ V \qquad (3.2)$$

The deposition of the element with the more positive formal potential (Ag) will be

mass transfer limited at potentials positive of the onset of alloy co-deposition. At this potential, $X_{Ag} = 1$ (X_{Ag}, Ag mole fraction) and $X_{Au} = 0$. As the potential becomes more negative, the deposition of the element with the more negative formal potential (Au) will occur under kinetic control, and the two elements will co-deposit. Since the rate of electrodeposition of Au is potential dependent in this region, the composition of the alloy will also be a function of the potential. Finally, when the potential becomes negative enough that both elements are depositing at their diffusion limited rates, the alloy composition will be determined by the relative concentration of the precursor species in solution (here, ca. 1:1). Thus, the alloy composition will be potential dependent on the range of potentials spanned by $\Delta E^{0'}$ (= $E^{0'}_{Ag} - E^{0'}_{Au}$ = 200mV) and will be constant at more positive or negative potentials. This corresponds exactly to the behavior shown in Fig. 3.2. More specifically, the alloy gradient spans a distance of ca. 1.5 mm which corresponds to a ΔE value of 204 mV assuming a linear potential gradient of 136 mV/mm (2.464 V applied potential/18 mm length) under our experimental conditions. This is clearly in excellent agreement with our predictions and is strong indirect evidence that the interfacial potential gradient is linear[16] and that bipolar electrodeposition follows the predictions of Faraday's law.

3.3.2 Screening the optical properties of Ag-Au alloy gradient using SERS:

Having established that it is possible to form Ag-Au alloy gradient thin films using BP-ED, we employed SER spectroscopy to screen the optical properties of these materials. Immediately following the BP-ED step, the samples were rinsed in pure water and dried in a stream of flowing N_2. Then a self-assembled monolayer (SAM) of benzene thiol was allowed to form on the alloy surface by soaking the chemically modified BPE in a 1 mM

benzene thiol solution in ethanol for 24 h. A representative SERS spectrum of a benzene thiol SAM excited using 514.5 nm is shown in Fig. 3.3. The SERS peak frequencies and relative intensities are in excellent agreement with previously published SERS spectra of benzene thiol.[17]

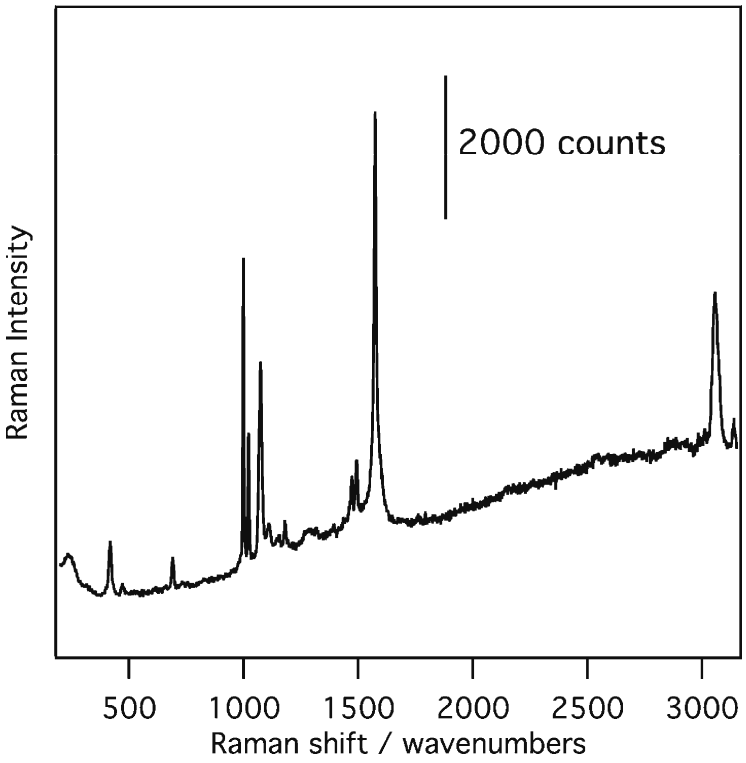

Fig. 3.3 SERS spectrum of a benzene thiol SAM adsorbed on a Ag-Au alloy film excited using 514.5 nm radiation.

A confocal Raman microscope was used to acquire SER spectra at multiple points along the principal axis of the BPE using two excitation wavelengths (514.5 and 785 nm). The integrated intensity of the 1574 cm^{-1} benzene thiol SERS band (assigned as the a_1 symmetric ν(C-C-C) band)[17] is plotted as a function of the alloy composition and excitation wavelength (solid circles, 514.5 nm excitation; open circles, 785 nm excitation) in Fig. 3.4. The SERS intensity observed using both excitation wavelengths was found to

increase as the atomic percentage of Ag in the alloy increased. This observation is consistent with results published previously by Link et al.,[18] who reported an increase in the optical extinction of Ag-Au alloy nanoparticles (NPs) as a function of increasing Ag mole fraction. The increase in SERS intensity we observe as a function of position along the alloy gradient reflects the fact that the electromagnetic enhancement of benzene thiol Raman scattering depends on the optical extinction of the alloy substrate.

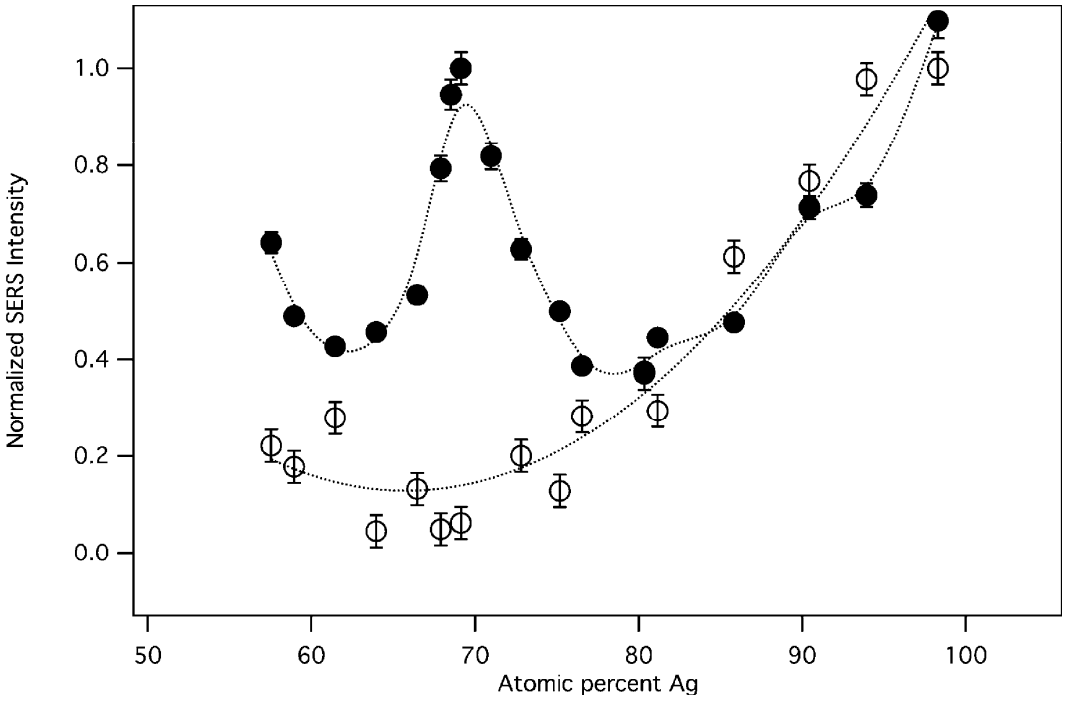

Fig. 3.4 Integrated intensity of the 1574 cm^{-1} benzene thiol SERS band plotted as a function of the alloy composition and excitation wavelength (solid circles, 514.5 nm excitation; open circles, 785 nm excitation). Error bars correspond to plus/minus one standard deviation of a minimum of five replicate measurements.

The data presented in Fig. 3.4 also reveal an optimum alloy composition of about 70% Ag for SERS excited using 514.5 nm radiation, but not for SERS excited using 785

nm light. The existence of an optimum alloy composition for SERS excited using 514.5 nm light is expected based on a consideration of the optical properties of Ag-Au alloy NPs, for which the visible local surface plasmon resonance (LSPR) is well-known to blue shift with increasing Ag atomic percentage. While the details of the origin of this effect remain somewhat controversial, the linear dependence of the visible LSPR on alloy composition in these systems is not in doubt. Indeed, even in the early work of Papavassilou,[19] for example, it was observed that the plasmon band of Au-Ag alloy sols was a linear function of the mole fraction of Ag. Later, Link et al.[18] presented similar results and provided convincing arguments that the optical properties of the alloy were unique and not simply the weighted average of the pure component optical constants as suggested by earlier researchers. They also showed structural data based on high resolution transmission electron microscopy indicating the formation of single phase alloy nanoparticles. More recently, Park and co-workers[20] studied the optical behavior of Ag-Au nanorods and found similar behavior; that is, the LSPR frequency of the nanorod is a linear function of its chemical composition. These workers also observed a red-shift of the LSPR depending on the nanorod aspect ratio. Our observation of a LSPR resonance for 514.5 nm radiation is thus consistent with the relatively large, nonspherical alloy particles present in our electrodeposited alloy gradients. Finally, the data presented in Fig. 3.4 also indicate that no combination of film thickness, crystallite size, and alloy composition that we could achieve using bipolar electrodeposition was optimal for SERS excited using 785 nm radiation.

To rule out the possibility that segregation of significant amounts of Ag to the surface of the alloys was occurring, we performed a study in which the total deposition

time was systematically varied, reasoning that if the surface composition of the films is different from that of the bulk, gradients formed using shorter deposition times (thinner films) should exhibit different optical properties than those deposited using longer times (thicker films). For all the alloy gradients studied (t_{dep}= 15, 30, and 60 s), the dependence of SERS intensity on alloy composition at both wavelengths was identical to the data presented in Fig. 3.4.

Finally, in order to test the generality of our spectroscopic measurements, we repeated our Raman experiment using a nonaromatic probe molecule (decanethiol) and monitoring a significantly higher vibrational frequency (ca. 2900 cm^{-1}). We found the behavior of decanethiol to be indistinguishable from that of benzene thiol.

3.4 Conclusions:

We have shown that bipolar electrochemistry is a useful tool for the rapid fabrication of solid-state chemical composition gradients that are suitable for screening using a wide variety of conventional surface analysis techniques. The screening of optical properties of Ag-Au alloy gradient using SERS exhibited an optimum composition of 70 atomic% Ag/ 30 atomic% Au with 514.5 nm excitation laser. Optimization of Ag-Au alloy compositional gradient for a durable and sensitive SERS substrate is a significant contribution for several analytical applications such as medical diagnostics, drug discovery, forensics and chemical development. Screening the optical properties of Ag-Au alloy composition gradient using SERS is an example to illustrate that the Bipolar electrodeposition is quick enough in helping us to understand the systematic relationship between the material composition and its property.

Reference:

(1) Arora, A.; Eijkel, J. C. T.; Morf, W. E.; Manz, A. *Anal. Chem.* **2001**, *73*, 3282–3288.

(2) Mavre, F.; Anand, R. K.; Laws, D. R.; Chow, K.-F.; Chang, B.-Y.; Crooks, J. A.; Crooks, R. M. *Anal. Chem.* **2010**, *82*, 8766–8774.

(3) Laws, D. R.; Hlushkou, D.; Perdue, R. K.; Tallarek, U.; Crooks, R. M. *Anal. Chem.* **2009**, *81*(21), 8923–8929.

(4) Zhan, W.; Alvarez, J.; Crooks, R. M. *J. Am. Chem. Soc.* **2002**, *124*(44), 13265–13270.

(5) Ulrich, C.; Andersson, O.; Nyholm, L.; Björefors, F. *Angew. Chem.* **2008**, *47*(16), 3034–3036.

(6) Ulrich, C.; Andersson, O.; Nyholm, L.; Björefors, F. *Anal. Chem.* **2009**, *81*, 453.

(7) Choi, H. C.; Buriak, J. M. *Chem. Commun*. **2001**, 1614–1615.

(8) Warakulwit, C.; Nguyen, T.; Majimel, J.; Delville, M. H.; Lapeyre, V.; Garrigue, P.; Ravaine, V.; Limtrakul, J.; Kuhn, A. *Nano Lett.* **2008**, *8*, 500–504.

(9) Ramakrishnan, S.; Shannon, C. *Langmuir* **2010**, *26*(7), 4602–4606.

(10) Duval, J.; Mieke-Kleijn, J.; van Leeuwen, H. P. *J. Electroanal. Chem.* **2001**, *505*, 1–11.

(11) Duval, J. F. L.; van Leeuwen, H. P.; Cecilia, J.; Galceran, J. *J. Phys. Chem. B* **2003**, *107*, 6782–6800.

(12) Duval, J. F. L.; Buffle, J.; van Leeuwen, H. P. *J. Phys. Chem. B* **2006**, *110*, 6081–6094.

(13) Brenner, A. *Electrodeposition of Alloys;* Academic Press: New York, 1963; Vols. *1 and 2*.

(14) Marquez, K.; Ortiz, R.; Schultze, J. W.; Marquez, O. P.; Marquez, J.; Staikov, G. *Electrochim. Acta* **2003**, *48*, 711–720.

(15) Benedetto Bozzini, B.; De Gaudenzi, G. P.; Mele, C. *J. Electroanal. Chem.* **2004**, *563*, 133–143.

(16) Chang, B.-Y.; Mavre, F.; Chow, K.-F.; Crooks, J. A.; Crooks, R. M. *Anal. Chem.* **2010**, *82*, 5317–5322.

(17) Abdelsalam, M. E.; Bartlett, P. N.; Baumberg, J. J.; Cintra, S; Kelf, T. A.; Andrea, E. Russell, A. E. *Electrochem. Commun.* **2005**, *7*, 740–744.

(18) Link, S.; Wang, Z. L.; El-Sayed, M. A. *J. Phys. Chem. B* **1999**, *103*, 3529–3533.

(19) Papavassiliou, G. C. *J. Phys. F: Me. Phys.* **1976**, *6*(4), L103–L105.

(20) Bok, H.-M.; Shuford, K. L.; Kim, S.; Kim, S. K.; Park, S. *Langmuir* **2009**, *25*(9), 5266–5270.

Chapter 4

Bipolar electrodeposition of Pd-Au alloy gradient and screening of its electrocatalytic property using Raman spectroelectrochemistry

4.1 Introduction:

In our first study, our approach was to electrodeposit alloy with varying composition on a single substrate and screen them for a specific application using a surface probe technique. We electrodeposited Ag-Au alloy with gradient composition and screened it for the SERS application.[1] Following this, we extended our approach of screening the alloy compositional gradient for electrocatalysis. We obtained the Pd-Au alloy gradient by BP-ED and screened their electrocatalytic activity towards formate oxidation using Raman spectroelectrochemistry.

Our choice of Pd-Au alloy bipolar electrodeposition applied for the electrocatalytic purpose began with the following facts

(1) Pd and Au form homogeneous alloy at all alloy compositions.[2]

(2) The gradual compositional variation of Pd-Au alloy electrodeposition depending on the applied potential has been already established in the acidic chloride bath.[3]

(3) Pd and Pd based alloys have been proven to be good catalysts for small organic molecule electrooxidation.[4-9]

Nishimura, et al. have studied the synergy between Pd and group 1B metals (Au, Ag,

Cu) for the electrooxidation of formate and formaldehyde.[4] They observed a moderate synergy with a maximum catalytic activity at 50 to 70 atomic % Pd towards the oxidation of formate on Pd-Au alloy in alkaline medium.

IR spectroscopic studies on the surface species derived from formate in alkaline solution on Pd-Au alloy electrodes proved that there was no CO_{ad} on the Pd-Au alloy surface.[5]

Baldauf, et al. have studied formic acid oxidation on Pd monolayer on Au and Pt single crystal surfaces as well as on Pd single crystal surfaces.[6] Pd(100) exhibited the highest catalytic activity of all three low-index faces, and Pd film on Pt(hkl), even when two or three layers thick, generally exhibited a much higher activity than Pd films on Au(hkl) or bulk Pd(hkl). In all cases, a high resistivity of the Pd surface against poisoning by the CO was observed which makes Pd an interesting alternative to the often quickly deactivated Pt as catalyst for organic fuel cell reactions.

Zhu, et al. have constructed the direct formic acid fuel cell (DFAFC) with Pd as anode, which has shown the cell performance near to H_2-air proton exchange membrane fuel cell (PEMFC) and better than direct methanol fuel cell (DMFC) using Pt-Ru as anode catalyst.[7]

Larsen, et al. have tested unsupported Pd black, carbon-supported Pd catalyst and Pd-Au (50:1 atomic ratio alloy) supported on Vulcan XC-72 carbon.[8] Their study shows that carbon-supported Pd catalyst showed good activity and efficient Pd metal utilization. Addition of gold to carbon-supported Pd improves catalytic performance, suggesting that the activity of Pd-based catalyst can be further improved.

The overall equation representing the formate electrooxidation reaction under

alkaline condition is[9]

$$HCOO^- + 3OH^- \longrightarrow CO_3^{2-} + 2H_2O + 2e^-$$

The formate (reactant) and the carbonate (product) both are Raman active[10,11] and it was convenient to use Raman spectroelectrochemistry to follow the reaction kinetics of formate electrooxidation on Pd-Au alloy surface by monitoring the Raman signal intensity of formate and carbonate in the diffusion layer of the alloy surface as a function of time.

The screening of Pd-Au alloy gradient for the formate oxidation in the alkaline medium which is free from the surface poisoning of CO_{ad} species can significantly contribute to the development of alkaline fuel cell (AFC) technology. There is a scope for the AFC technology to get rejuvenated due to the arrival of alkaline anion exchange membrane with cationic head groups such as tetra alkyl ammonium ($-NR_3^+$) replacing the use of aqueous KOH as the electrolyte.[12] The use of alkaline anion exchange membrane can solve the issue of carbonate precipitation occurring in the porous medium (separator) holding the liquid electrolyte, (KOH_{aq}) between anode and cathode in the alkaline fuel cell.[12,13]

The Alkaline fuel cell was the first fuel cell to be developed commercially and is the best performing of all fuel cells.[12] The ORR is more facile in alkaline medium than acidic medium resulting in high cell voltage for a given current density when Pt is used as cathode and anode catalyst in a H_2-fed AFC. There is a flexibility to use non-noble metals as cathode catalyst as they are proved to be good catalyst for ORR under alkaline condition.[13] Alkaline environment favours a good life for the fuel cell components[13]. Use of liquid fuel (formic acid or methanol) avoids certain drawbacks associated with H_2-PEMFC such as low gas-phase energy density of H_2, high cost of miniaturized hydrogen

containers and the possible dangers in transporting the hydrogen containers.[13] Hence it is expected that the incorporation of CO poison free high kinetc Pd-Au anode catalyst with the aforementioned favourable conditions can stimulate the growth of alkaline fuel cell technology.

4.2 Experimental section:

4.2.1 Electrodeposition of Pd-Au alloy gradient on a Au Bipolar electrode:

Acidic chloride bath containing 10 mM $HAuCl_4$, 163 mM H_2PdCl_4 in 0.5 M HCl is used to deposit Pd-Au alloy in a gradient manner on a gold bipolar electrode which is placed between the two graphite driver electrodes. Voltage applied between the driver elctrodes is 9.4 V for about 1 min. The length of the bipolar electrode used is 18 mm.

4.2.2 Characterization of the Pd-Au alloy electrodeposit:

(i) Scanning Electron Microscopy (SEM) and Energy Dispersive X-ray spectroscopy (EDX): SEM images of the electrodeposited Pd-Au alloy on a gold bipolar electrode were obtained from a JOEL JSM- 7000F field- emission scanning electron microscope and analysed using the EOS 7000F software package. EDX data were acquired using the Oxford X-Max energy dispersive X-ray spectrometer and were analysed using the INCA software package.

(ii) X-ray diffraction (XRD) measurements: XRD data was obtained on the Pd-Au alloy gradient from Bruker D8 DISCOVER with GADDS (General area detector diffraction system) instrument.

4.2.3 Raman spectroelectrochemistry:

After a short cleaning of the Pd-Au alloy gradient thin film by cycling the potential

between -972 mV and 478 mV vs Ag/AgCl(sat) in 1 M NaOH, it was connected as the working electrode in a conventional 3-electrode electrochemical circuit. A Pt mesh was used as the counter electrode and Ag/AgCl(sat) was used as the reference electrode. All potentials given in this chapter are referred against Ag/AgCl(sat). The cell was designed to allow the simultaneous collection of electrochemical and Raman spectroscopic data. The catalytic conversion of formate to carbonate under basic conditions was monitored at a fixed applied potential using a Raman microscope to interrogate the small volume of solution directly above the electrocatalyst surface. To achieve this, we pre-focused the Raman laser on the electrode surface and then used the microscope stage to reposition the electrode ca. 25 μm behind the focal volume defined by the microscope optics before carrying out the spectroelectrochemical measurements.

4.3 Results and Discussion:

4.3.1 Characterization of the Pd-Au alloy gradient on the bipolar electrode:

(i) Chemical composition of the Pd-Au alloy gradient determined by EDX:

Fig. 4.1a shows the chemical composition of the deposited Pd-Au alloy gradient determined by EDX as a function of the distance along the bipolar electrode length. The origin in this composition vs distance plot represents the cathodic end of the alloy deposit and the alloy deposition covers a distance of 5mm towards the center of the bipolar electrode. Since Pd is less noble than Au, Pd atomic % increases from 14 to 82% with the increasing negative potential towards the cathodic end of the bipolar electrode. Fig. 4.1b shows the representative SEM image of the Pd-Au alloy deposit.

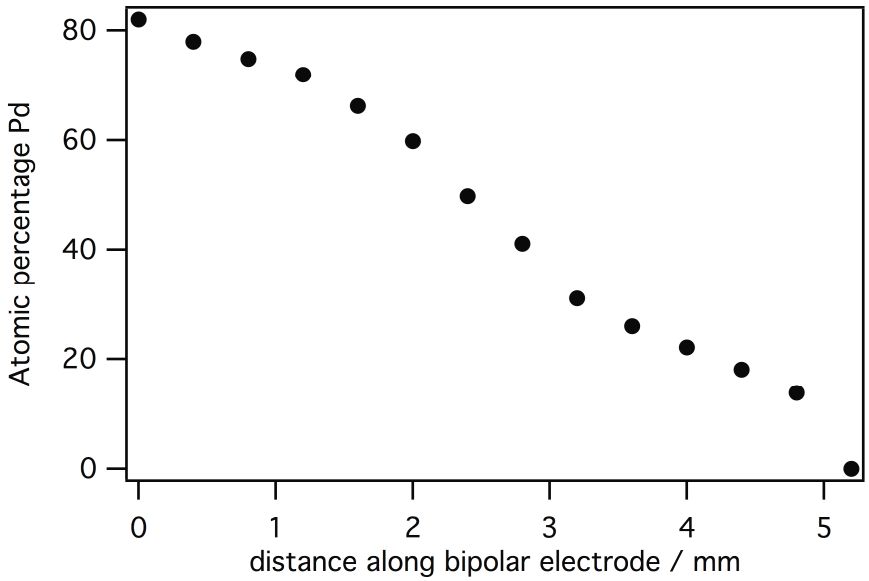

Fig. 4.1a Chemical composition of the Pd-Au alloy gradient deposited onto gold bipolar electrode given as a function of lateral position along the length of the bipolar electrode determined by EDX.

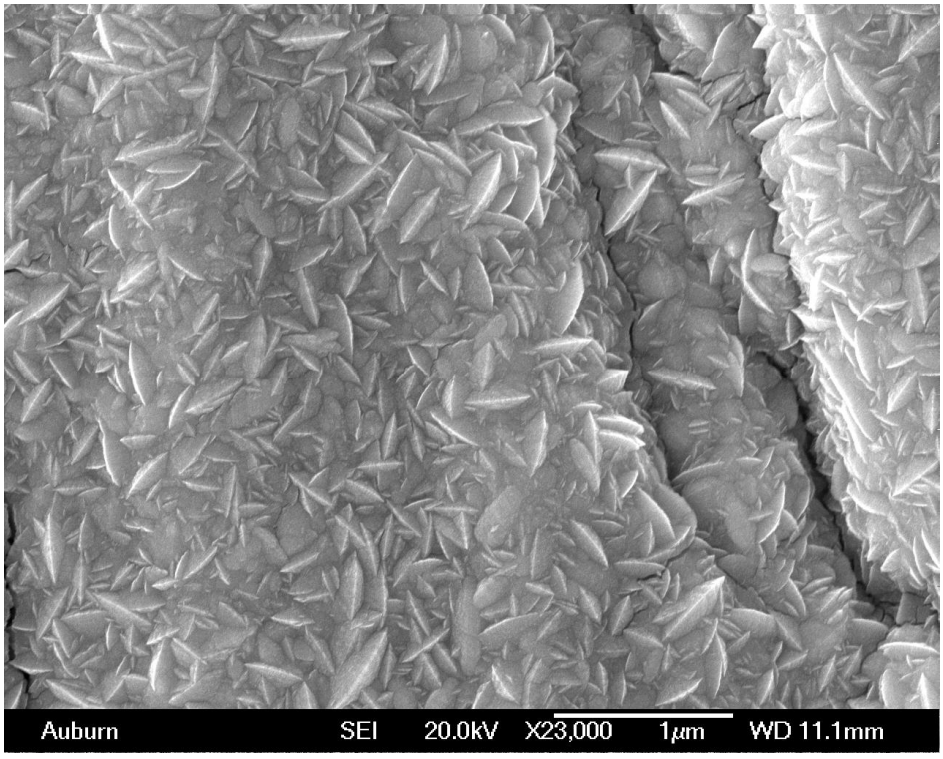

Fig. 4.1b A representative SEM image of the Pd-Au alloy deposit

(ii) XRD measurements on the Pd-Au alloy gradient:

XRD measurements were taken on the Pd-Au alloy gradient with 0.52 mm interval for a length of 4.16 mm. Fig. 4.1c shows a representative X-ray diffractogram collected at a spot corresponding to Pd atomic% of 82 with X-ray diffraction peaks from the alloy (a) at 39.80˚ (111), 46.41˚ (200), 67.64˚ (220), 86.06˚ (222) along with the substrate gold peaks (s) at 38.12˚ (111), 44.27˚ (200), 64.57˚ (220), 77.42˚ (311), 81.76˚ (222). Fig. 4.1d shows the overlay of the alloy X-ray diffraction peaks (deconvoluted using the function 'PearsonVII' in OriginPro 8.6 32Bit.) for (111) reflection, corresponding to different spots on the alloy gradient with 0.52 mm interval. The gradual decrease in the alloy X-ray diffraction peak intensity (while moving over the gradient from Pd-rich alloy towards the Au-rich alloy) is supportive to the established lateral potential gradient along the length of the bipolar electrode. The peak center shifts from 2θ position corresponding to pure Pd (40.2˚) close to 2θ position corresponding to pure Au (38.12˚) as indicated in Fig. 4.1d. (The vertical lines indicate the 2θ position for Au and Pd).

The gradual shift of the alloy X-ray diffraction peak in 2θ position with respect to the alloy composition supports that the electrodeposited Pd-Au alloy compositional gradient forms a homogeneous solid solution and our results agree with the previous XRD results reported by Sehayek et al.[3] The obtained 2θ positions associated with (111), (200) and (220) reflections on the Pd-Au alloy gradient are presented in Table 4.1.

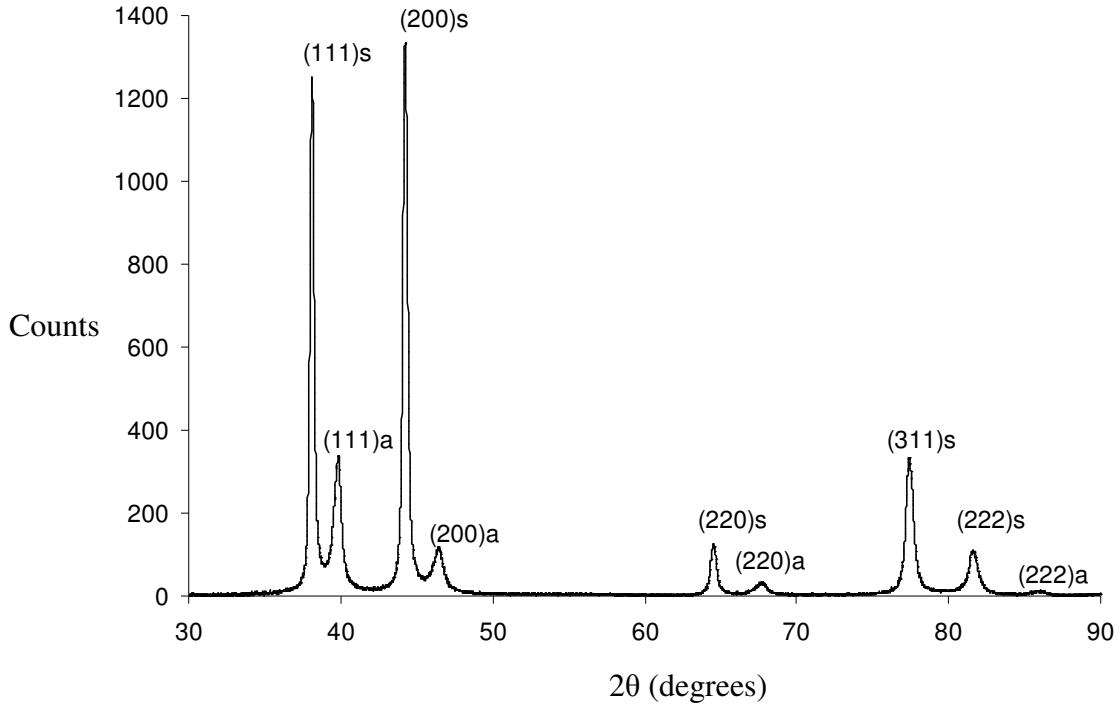

Fig. 4.1c A representative X-ray diffractogram collected at a spot corresponding to Pd atomic% of 82 in the Pd-Au alloy gradient. ‘s’ indicates the diffraction peak from the gold substrate and ‘a’ indicates the diffraction peak from the Pd-Au alloy.

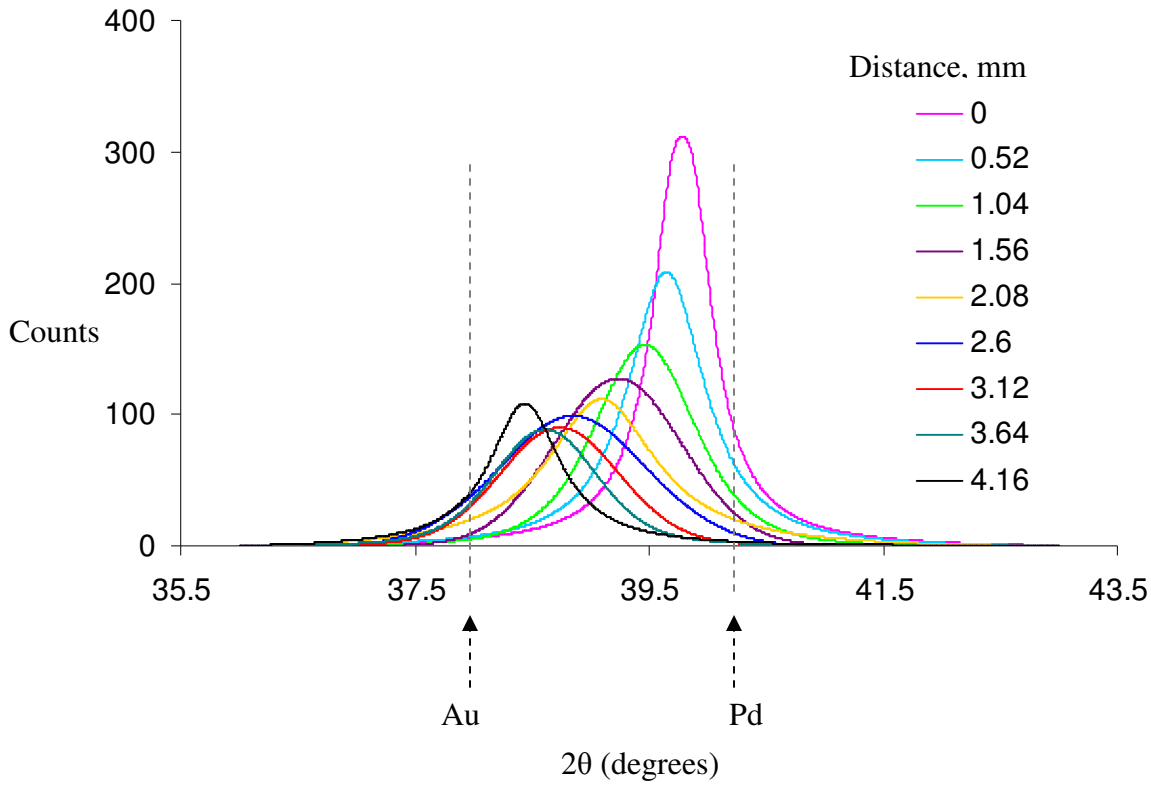

Fig. 4.1d Overlay of the Pd-Au alloy X-ray diffraction peaks (corresponding to (111) reflection) collected at various spots on the Pd-Au alloy gradient (deconvoluted using the function 'PearsonVII' in OriginPro 8.6 32Bit).

Table 4.1 XRD results (2θ) obtained on the Pd-Au alloy gradient

Distance	2θ [˚]		
mm	(111)	(200)	(220)
0	39.8	46.41	67.64
0.52	39.66	46.36	67.47
1.04	39.48	46.34	67.2
1.56	39.25	45.76	66.72
2.08	39.1	45.75	66.42
2.6	38.87	45.22	65.79
3.12	38.75	45.13	65.67
3.64	38.63	44.87	65.54
4.16	38.46	-	64.96

Note: 0 mm represents the cathodic pole of the alloy gradient electrodeposit.

We found the alloy composition using Vegard's law[14] based on the lattice constant found from each reflection (111), (200) and (220) and then the alloy compositions were averaged. For each reflection, d-space value was found from 2θ position of the alloy X-ray diffraction peak using Bragg's law '$2d\sin\theta = n\lambda$' (λ = 1.54 Å for Cu K_α X-ray source).[15] Since the crystal structure of Pd-Au alloy belongs to a cubic system (face centered cubic) the lattice constant is given by $d \times \sqrt{(h^2 + k^2 + l^2)}$.[15] According to Vegard's law, the lattice constant of the Pd-Au alloy ($a_{Pd\text{-}Au}$) is approximately equal to the composition-weighted average of the lattice constants of pure Pd (a_{Pd}) and Au (a_{Au}).[14]

$$a_{Pd\text{-}Au} = (a_{Pd} \times m_{Pd}) + (a_{Au} \times m_{Au}) \quad (4.1)$$

where m_{Pd} is the mole fraction of Pd

and m_{Au} is the mole fraction of Au

Substituting $m_{Au} = 1 - m_{Pd}$ and rearranging Equation 4.1 results in

$m_{Pd} = (a_{Pd\text{-}Au} - a_{Au}) / (a_{Pd} - a_{Au})$

Using the known values of lattice constant of Pd (3.89 Å), lattice constant of Au (4.08 Å) and lattice constant of Pd-Au alloy obtained from the d-space values derived from the XRD results (2θ), the alloy composition was calculated. The Pd-Au alloy composition calculated from XRD measurements (along with the alloy composition from EDX) versus distance over the alloy gradient on the bipolar electrode is given in Fig. 4.1e. The Pd atomic% calculated from XRD measurements is comparable with the one determined by EDX.

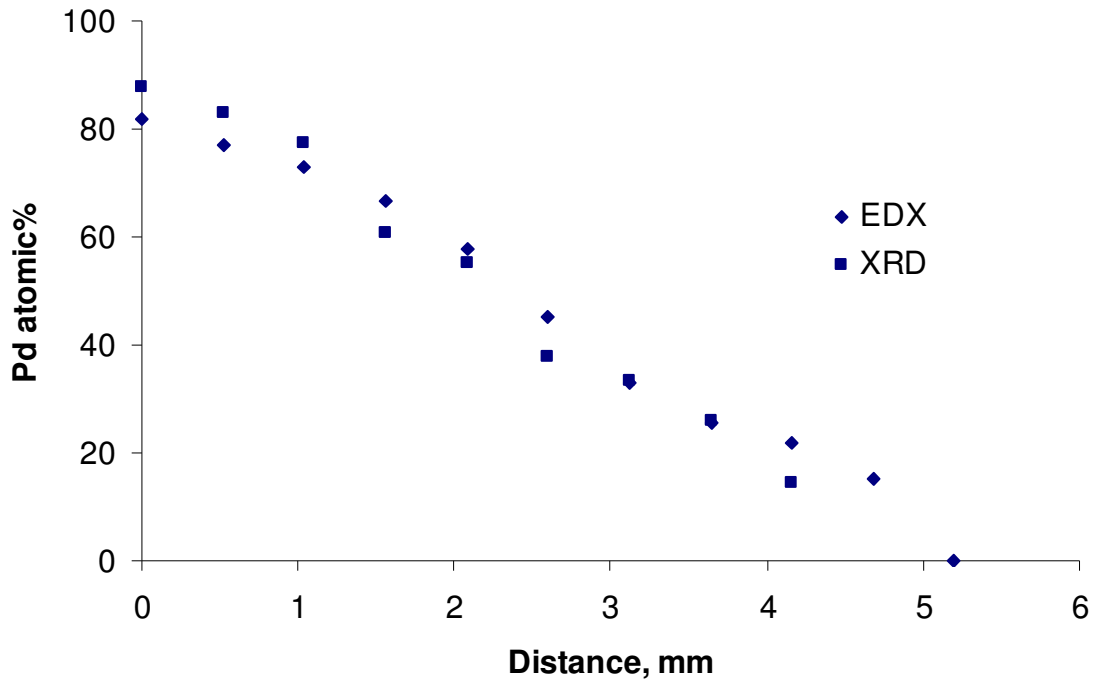

Fig. 4.1e Pd-Au alloy composition (determined by EDX and XRD) versus distance over the alloy gradient on the bipolar electrode.

4.3.2 Screening of Pd-Au alloy gradient for formate electro-oxidation:

With the literature stating that the electrochemical potential cycling(cleaning) of Pd-Au alloy in alkaline medium (1 M NaOH) does not change the surface composition,[4] we carried out the cleaning followed by the electrooxidation of formate in 1 M NaOH at a constant potential of -800 mV (The formate oxidation cyclic voltammogram on a pure pd surface in 1 M NaOH is given in Fig. 4.2 for the reader to refer) and the Raman spectra were collected until the reactant and product signal intensities remained constant indicating the steady state of the formate oxidation reaction.

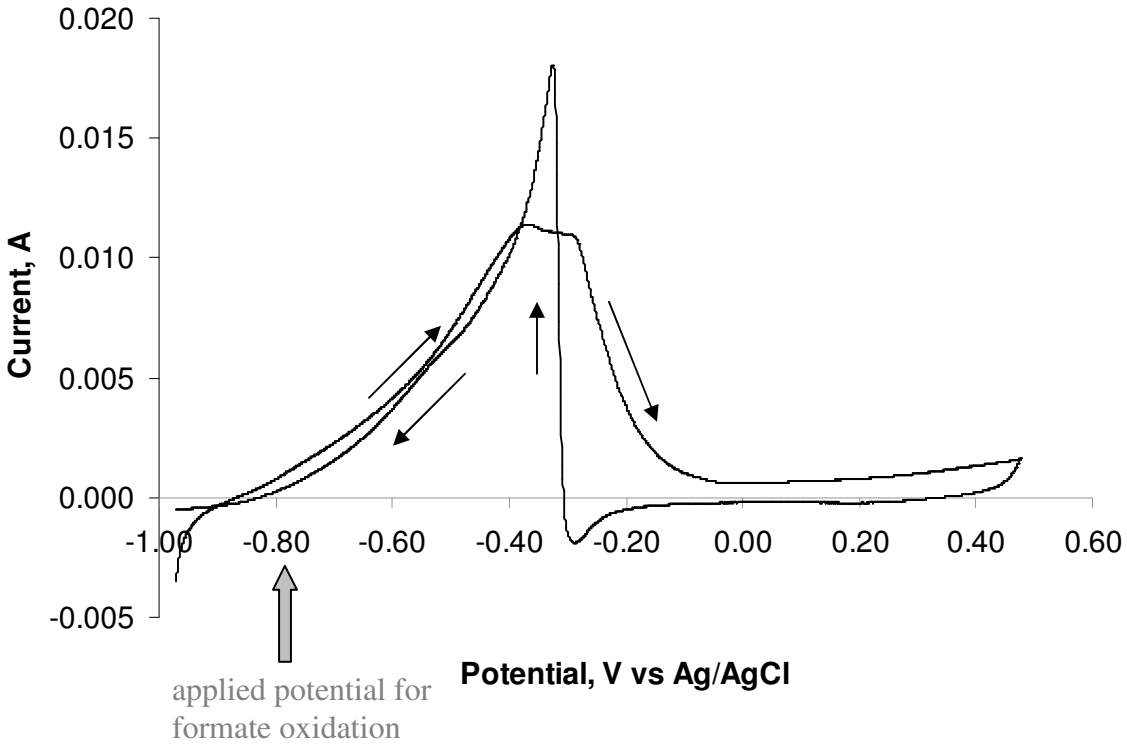

Fig. 4.2 Formate oxidation on Pd surface in a deoxygenated solution containing 0.3 M sodium formate in 1.0 M sodium hydroxide. Scan rate 10 mV/s.

Before applying -800 mV, the bipolar electrode was held at -912 mV, to suppress the

product formation, during which the formate C-O stretch band[10] intensity at 1349 cm^{-1} is around 200 cps on all Pd-Au compositions on the bipolar electrode. On applying -800 mV, the formate signal intensity at 1349 cm^{-1} gradually decreased with time while the intensity of carbonate stretch[11] near 1065 cm^{-1} increased. Formate and carbonate Raman bands were distinct and easy to quantify. A representative data set showing the time dependence of the formate (0.30 M) to carbonate oxidation after a potential step from -912 mV to -800 mV is shown in Fig. 4.3. . The data set represented here is collected at a composition of 66.2 atomic% Pd/ 33.8 atomict% Au and with a time interval of 52 second.

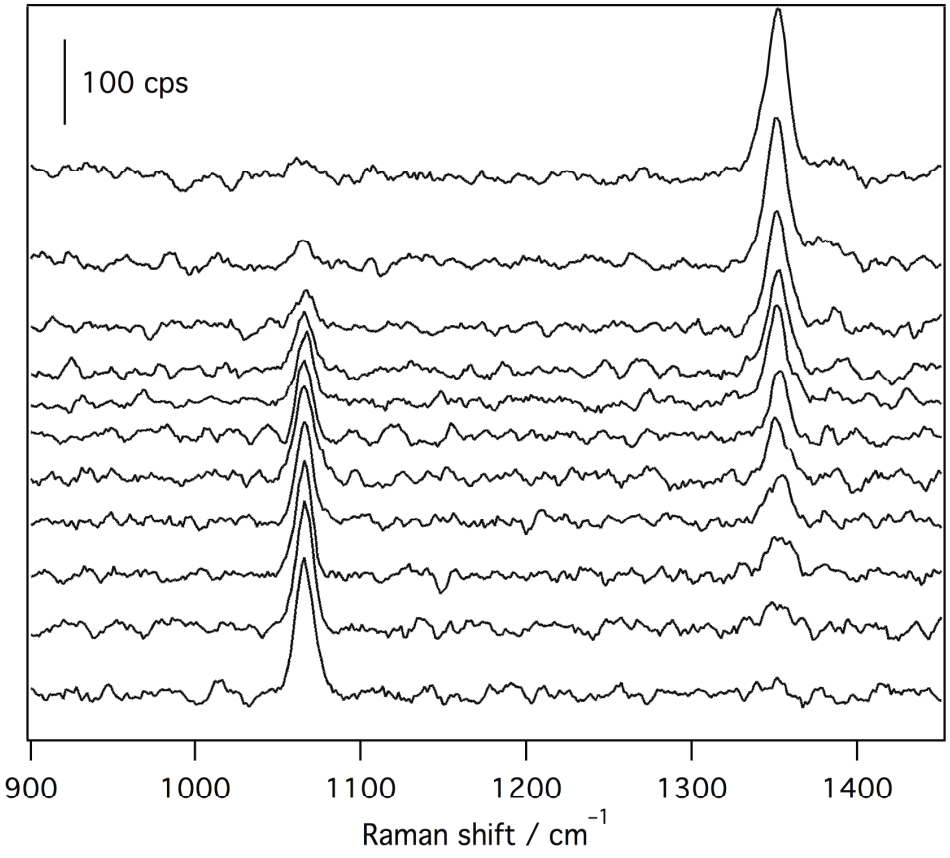

Fig. 4.3 Catalytic electro-oxidation of formate to carbonate at 66.2 atomic% Pd/ 33.8 atomict% Au alloy, followed using Raman spectroscopy. Time increases from top to bottom with an interval of 52 second.

We observed an apparent first order decay of the formate Raman peak intensity. Kinetic data were measured from twenty spots along the bipolar electrode-each corresponding to a unique Pd-Au alloy composition. Representative data are shown in Fig. 4.4. We fit all of the kinetic data using a simple first order decay model ($[A]/[A]_0 = e^{-kt}$, where [A] = concentration of reactant at time t, $[A]_0$ = initial concentration of reactant, k = apparent first order rate constant) and calculated the apparent first order rate constants. The apparent rate constant (k) for each alloy composition is plotted in Fig. 4.5. An optimum alloy composition was observed, corresponding to about 70% Pd- 30% Au.

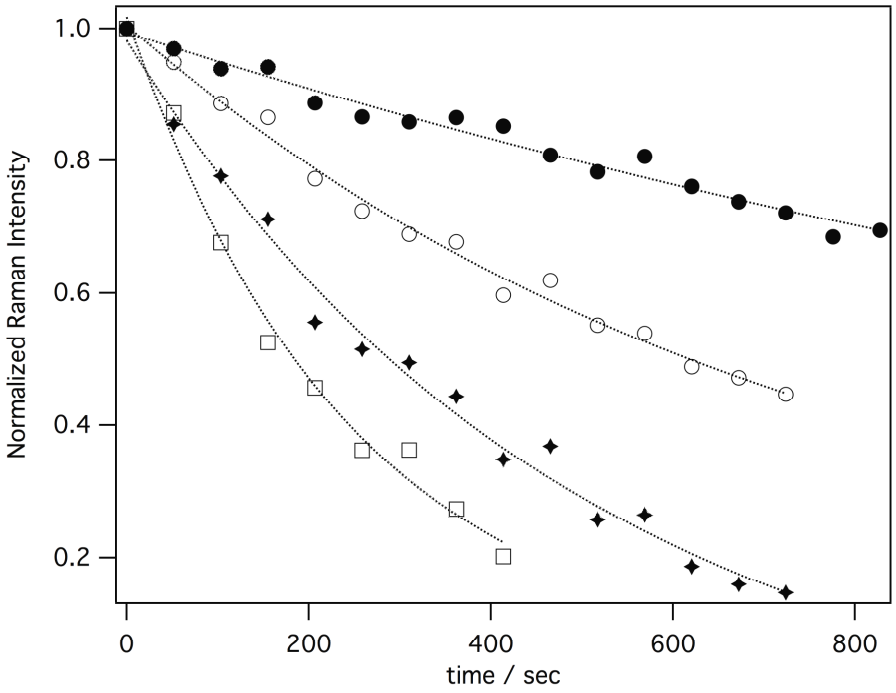

Fig. 4.4 Pseudo-first order decay of [formate] measured at different points along the BPE. Each point corresponds to a unique alloy composition. (Top to bottom: Pd atomic% is 18.1, 31.0, 59.8 and 74.8)

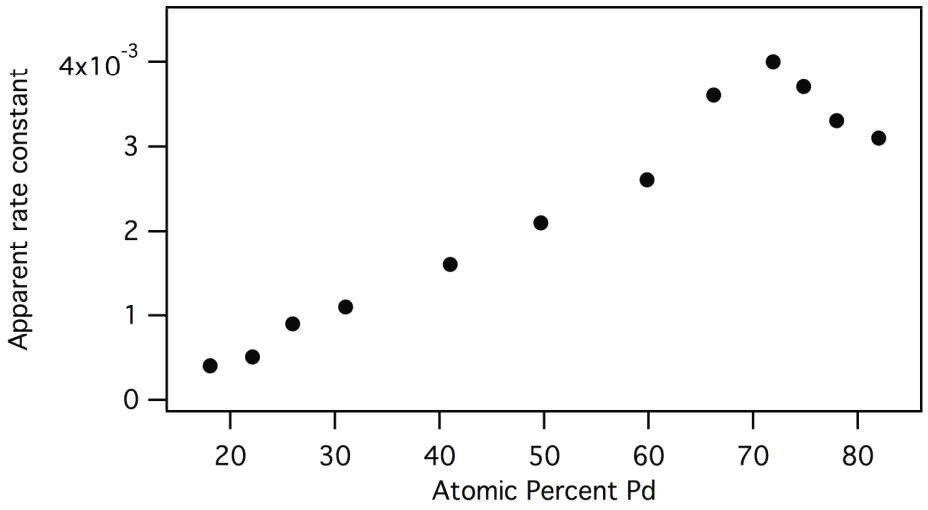

Fig. 4.5 Apparent rate constant for formate oxidation plotted as a function of Pd atomic percent.

Allison and Bond have compiled a few models in their review[2] which explain the variation in the catalytic activity of alloys between metals of Group VIII and IB with their alloy composition based on the variation in their electronic property. According to the band theory model, when Pd forms alloy with Au, the 6s electron of Au is donated to Pd to fill its d-band vacancy of 0.6. So, when the concentration of Au increases in the Pd-Au alloy, the d-band vacancy decreases and at a critical alloy composition of 60% Au, d-band vacancy is completely filled. Primitive models of band theory approach assume that the bulk and surface atoms of the alloy have similar properties. So, a broad metallic d-band is applied to the surface atoms and the filling of d-band vacancy with increasing Au concentration in the alloy will not make any remarkable change in the available electronic energy states until the d-band vacancy is completely filled. Based on these assumptions, only limited cases such as a constant catalytic activity (for reactions which require the d-band holes and not dependent on the d-band holes concentration) or a gradually increasing or decreasing catalytic activity (for reactions which are dependent on the d-band hole

concentration) over a composition range, where the d-band hole concentration is varying from a maximum of 0.6 to zero could be explained.

So, our optimum alloy composition of 70 atomic% Pd/ 30 atomic% Au which has shown the maximum catalytic activity cannot be explained by these simple primitive band theory models. Advanced models consider that surface atoms have different electronic properties than the bulk atoms in an alloy. According to a band theory approach applied to the alloy surface, within d-band t_{2g} electrons occupy a broad metallic band whereas the e_g electrons occupy a narrow localized band with high densities of states. If the s-electrons of Au occupy the e_g states preferentially than t_{2g} states, then there is a possibility for a remarkable change in the available electronic energy states at a Au concentration less than the d-band vacancy filling concentration of 60 atomic% Au. Based on this model, the optimum composition of 70 atomic% Pd/ 30 atomic% Au for formate oxidation could be justified and as predicted by the d-band model, above 60 atomic% Au the catalytic activity of Pd-Au alloy is very less compared to pure Pd or the optimum composition of Pd-Au alloy. It implies that the formate oxidation reaction requires d-band holes.

4.4 Conclusions:

We obtained Pd-Au alloy gradient by bipolar electrodeposition and screened its electrocatalytic activity for formate oxidation using Raman spectroelectrochemistry. The optimum composition of 70 atomic% Pd/ 30 atomic% Au is believed to be the result of electronic effect induced by the addition of Au with Pd. This example illustrates the power of using material gradients to screen a wide range of compositions for optimum catalytic properties. The deposition of the gradient is rapid, and conventional surface analytical probes can be employed to screen the materials. The precise optimization of Pd-Au alloy

compositional gradient for formate oxidation is noteworthy for the growth of alkaline fuel cell technology.

References:

(1) Ramaswamy, R.; Shannon, C. *Langmuir* **2011,** *27*, 878-881.

(2) Allison, E. G.; Bond, G. C. *Catalysis Reviews*, **1972**, *7*, 233-289.

(3) Sehayek, T.; Bendikov, T,; Vaskevich, A.; Rubinstein, I. *Adv. Funct. Mater.* **2006**, *16*, 693–698.

(4) Nishimwa, K.; Machida, K.; Enyo, M. *J. Electroanal. Chem.* **1988**, *251*, 103-116.

(5) Nishimwa, K.; Kunimatsu, K.; Machida, K.; Enyo, M. *J. Electroanal. Chem.* **1989**, *260*, 181-192.

(6) Baldauf, M.; Kolb, D. M. *J. Phys. Chem.* **1996,** *100,* 11375-11381.

(7) Zhu, Y.; Khan, Z.; Masel, R.I. *Journal of Power Sources* **2005**, *139,* 15–20.

(8) Larsen, R.; Ha, S.; Zakzeski, J.; Masel, R. I. *Journal of Power Sources* **2006**, *157*, 78–84.

(9) Kjeang,E.; Michel, R.; Harrington, D. A.; Sinton, D.; Djilali, N. *Electrochimica Acta* **2008**, *54*, 698–705.

(10) Ito, K.; Bernstein, H.J. *Canadian Journal of Chemistry* **1956**, *34*, 170-178.

(11) Frantz, J. D. *Chemical Geology* **1998**, *152*, 211–225.

(12) Christensen, P. A.; Hamnett, A. Linares-Moya, D. *Phys. Chem. Chem. Phys.*, **2011**, *13*, 11739–11747.

(13) Antolini, E.; Gonzalez, E. R. *Journal of Power Sources* **2010**, *195*, 3431–3450.

(14) Denton, A. R.; Ashcroft, N. W. *Physical review A* 1991, *43*, 3161-3164.

(15) Mitchell, B. S. *An introduction to materials engineering and science for chemical and materials engineers*, Wiley-interscience, New Jersey, 2004.

Chapter 5

Summary of dissertation

A bimetallic ORR catalyst system has been developed based on the layer-by-layer assembly of PDDA-stabilized PtNP and Co-substituted Dawson type polyoxometalate through electrostatic interaction. The week physisorption of PDDA on PtNP surface makes the PDDA-stabilized PtNP a suitable catalyst for ORR along with Co-Dawson in the LBL film. However the free PDDA polymer molecules incorporated in the LBL assembly seems to resist the electron transfer and O_2 diffusion with in the thin film of LBL assembly. Future studies could be directed to improve the electronic conductivity of the film and to facilitate O_2 mass transport in the LBL film by incorporating materials such as carbon nanotube (CNT) and some pore forming materials.

With the help of bipolar electrodeposition, a lateral potential gradient can be established on the bipolar electrode surface and as a result a continuous alloy composition spread such as Ag-Au and Pd-Au have been generated as thin films on the bipolar electrode surface. With the help of microprobe techniques such as SEM/EDX and micro Raman spectroscopy, it was made possible to characterize and screen these alloy gradients for various applications. We found the optimum Ag-Au alloy composition to be 70 atomic% Ag/30 atomic% Au for making a stable and sensitive SERS substrate and the optimum Pd-Au alloy composition to be 70 atomic% Pd/30 atomic% Au for the maximum electrocatalytic activity for the formate oxidation applied in formate ion fuel cell.

In the X-ray diffractogram of Pd-Au alloy deposit, the substrate (gold) X-ray diffraction peaks appear along with the alloy X-ray diffraction peaks. Since the Au-rich alloy X-ray diffraction peaks completely merge with the substrate (gold) X-ray diffraction peaks, we are unable to access the accurate information about the Au-rich alloy X-ray diffraction peaks below 14 atomic% Pd. Under this circumstance, thick deposit is required to avoid the interference of the substrate (gold) signal with the Pd-Au alloy signal. Increasing the thickness of the alloy deposit by extending the deposition time in bipolar electrochemical cell is not possible in the batch cell design that we used. The prolonged gas evolution reactions occurring at the driver electrodes change the pH of the electrolyte leading to the precipitation of metal hydroxides on the electrodeposit. The prolonged Faradaic reactions occurring at the bipolar electrode leads to the depletion of electroactive species in the bipolar electrode surface which can change the composition of the electrodeposit from the expected one.

A flow cell configuration of bipolar electrochemical cell can solve the above mentioned scientific issues associated with long time operation of the cell. A flow cell configuration can replenish the electrolyte in the bipolar electrochemical cell, which can avoid the pH change as well as the depletion of the electroactive species near the bipolar electrode surface. Since the outlet electrolyte will carry the driver electrode reaction products, recycling of the electrolyte is not advisable in the flow cell configuration. So the size of the cell and the bipolar electrode can be optimally designed in order to minimize the wastage of the electrolyte.